Combination of Metabolic Intervention and T Cell Therapy via Cell-Surface Anchor-Engineering Augments Solid Tumor Immunotherapy

Authors: Meixi Hao†, Siyuan Hou†, Weishuo Li, Kaiming Li, Lingjing Xue, Qifan Hu, Lulu Zhu, Yue Chen, Hongbin Sun, Caoyun Ju*, Can Zhang*

Affiliations:

State Key Laboratory of Natural Medicines, Jiangsu Key Laboratory of Drug Discovery for Metabolic Diseases, Center of Advanced Pharmaceuticals and Biomaterials, China Pharmaceutical University, Nanjing 210009, P.R. China.

* Corresponding author. Email: zhangcan@cpu.edu.cn (C.Z.); jucaoyun@cpu.edu.cn (J.C.Y.)

† These authors contributed equally to this work.

One Sentence Summary:

Combination of avasimibe and T cell via surface anchor-engineering yields sustained metabolic fitness and thus a synergistic efficacy in solid tumor.

Abstract: Treatment of solid tumors with T-cell therapy has yielded limited therapeutic benefits to date. Although T-cell therapy in combination with proinflammatory cytokines or immune checkpoints inhibitors has demonstrated preclinical and clinical successes in solid tumors, the unsatisfactory results along with the severe toxicities necessitate the development of novel combinatorial paradigm. Besides, a benign and general combinatorial technology to achieve maximum synergistic efficacy could be further optimized. Here, the liposomal avasimibe (an inhibitor of cholesterol-esterification enzyme, metabolism-modulating drug) containing bicyclo

[6.1.0] nonyne (BCN) groups was clicked onto the T-cell surface displaying functional tetrazine (Tre) groups-introduced by lipid insertion, without disturbing the physiological functions of T cell. The liposomal avasimibe (4 μg avasimibe per million T cells) could be restrained on the T cell surface during circulation and extravasation, and locally released to increase the level of cholesterol in T-cell membrane, consequently induce a rapid TCR clustering and sustained T-cell activation. Lastly, the surface anchor-engineered T cell, including mouse TCR transgenic $CD8^+$ T cell and human CAR-T cell, presented a superior anti-tumor and metastatic efficacy in mouse models of melanoma and glioblastoma. Notably, glioblastoma was completely eradicated in three of the five mice receiving surface anchor-engineered CAR-T cell, while mice in other treatment groups survived no more than 64 days. Moreover, the administration of engineered T cell showed no obvious systemic side effects. This cell-surface anchor-engineered T cell with sustained metabolic fitness is full of translational potential due to the facile and benign generation as well as the augmented action/safety profile.

Introduction

T-cell therapy has demonstrated great clinical and preclinical successes in haematological malignancies treatment (*1*, *2*). Despite these encouraging results, treatment of solid tumors with T cells yields limited therapeutic benefits (*3*). Most studies have focused on the co-administration of proinflammatory cytokines or immune checkpoint inhibitors with T cells, to boost the therapeutic index (*4-8*). However, the unsatisfactory results along with severe side effects necessitate the development of novel combination paradigm (*9*, *10*). It is increasingly recognized that the suppressive metabolic state of oxygen- and nutrient- deprived tumor microenvironment, largely impedes T-cell infiltration, survival, and effector function, which

likely comprised the therapeutic outcome of solid tumor T-cell therapy (*11*, *12*). Of note, the cellular metabolism involved diverse pathways, which offered a breadth of potential intervention targets (*12*). For example, T-cell function is positively dependent on the level of cholesterol on cell membrane to cluster T-cell receptor (TCR) and form immunological synapse (*13*-*15*). Therefore, intervention of cholesterol metabolism combined with T-cell therapy holds great promise for solid tumor immunotherapy.

Avasimibe (Ava), an inhibitor of the cholesterol-esterification enzyme acetyl-CoA acetyltransferase 1 (ACAT1), has the potential to elevate plasma membrane cholesterol levels, which in turn promotes TCR clustering and thus potentiating the effector function of T cells (*16*). We thereby reasonably envisioned that, combining Ava with T-cell therapy would boost solid tumor immunotherapy. However, the pharmacokinetics and biodistribution of Ava are completely different from that of T cells, which may impose difficulties on optimizing the synergistic effect (*17*-*20*). Thus, it is of great interest to develop novel and practical combinatorial technologies to maximize the synergistic effects.

Genetically-engineered T cell, serving as a living factory to produce the designed protein drugs, is generally utilized to realize the combined functions (*21*-*23*). Yet, the toxicity as well as the efficacy is heterogeneous, due to the uncertain expression of T-cell genes (*24*, *25*). Besides, small molecular drugs, cannot be manipulated in this genetic manner. Alternatively, backpacking nanoparticulated drugs onto T-cell surface via chemical conjugation or ligand-receptor biorecognition, has great potential in optimizing the synergistic effect, showing augmented T-cell function as well as improved therapeutic window of combined drugs (*26*-*28*). Of note, the above-mentioned technologies, either occupying the membrane biomolecules (*27*-*30*) (such as thiol groups and CD45 proteins) for a long time, or glycometabolism introducing exogenous

functional groups (*31*), e.g. azides, may impair the physiological functions of T cell. Thus, a benign and facile technology to backpack nanoparticulated drugs onto T-cell surface can be further optimized to reduce the influence of engineering process on T cell.

Here, inspired by glycosylphosphatidylinositol-anchored proteins on the plasma membrane and click chemistry, an alternative strategy to backpack drug on T cell surface by T-cell-surface anchor-engineering technology was developed. In specific, the functional tetrazine (Tre) groups were first introduced onto the T-cell surface via lipid insertion to cell membrane and then the liposomal Ava containing bicyclo [6.1.0] nonyne (BCN) groups was sufficiently clicked onto the cell surface with 4 μg Ava per million T cells, without disturbing the physiological functions of engineered T cell, e.g. transvascular migration and antigen-specific activation. Besides, the liposomal Ava could be restrained on the T cell surface during circulation as well as extravasation, and locally released to improve the level of cholesterol in T-cell membrane, consequently a rapid TCR clustering and sustained T-cell activation. Lastly, the engineered T cell, mouse TCR transgenic $CD8^+$ T cell and human CAR-T cell in this setting, showed a superior anti-tumor and metastatic efficacy in mouse models of melanoma and glioblastoma. Notably, glioblastoma was completely eradicated in three of the five mice receiving engineered CAR-T cell, while mice in other treatment groups survived no more than 64 days. Moreover, no obviously systemic side effects were detected in mice receiving engineered T cell.

Results

Design and generation of cell-surface anchor-engineered T cell (T-Tre/BCN-Lipo-Ava cell)

Cell-surface anchor-engineering of T cell involved two steps: i) the benign anchor of tetrazine-bearing, two-tailed lipids into the lipid bilayers of T-cell membrane via hydrophobic interactions,

endowing T-cell surface with tetrazines, and ii) the subsequent biorthogonal click reaction of cell-surface tetrazines with bicyclo [6.1.0] nonyne-containing liposomal Ava, as illustrated in Fig.1A. To this end, tetrazine-bearing, two-tailed lipid (1,2-distearoyl-sn-glycero-3-phosphoethanolamine-N-amino(polyethylene glycol)5000-tetrazine, DSPE-PEG_{5k}-Tre) and complementary bicyclo [6.1.0] nonyne-derived lipid (1,2-distearoyl-sn-glycero-3-phosphoethanolamine-bicyclo [6.1.0] nonyne, DSPE-BCN) were first designed and synthesized, of which structures were verified by proton nuclear magnetic resonance and mass spectrometry (fig. S1). The DSPE-PEG_{5k}-Tre was observed to rapidly react with DSPE-BCN at room temperature in PBS, as evidenced by ultraviolet spectroscopy (fig. S2A). Then we used DSPE-BCN as a functional component to prepare BCN-containing liposomal Ava (BCN-Lipo-Ava) based on our previous work (*32*). The obtained BCN-Lipo-Ava displayed an average particle size of 91.5 nm, with a uniform spheroid shape as suggested by transmission electron microscopy images (TEM) (fig. S2B). The loading capacity and entrapment efficiency of BCN-Lipo-Ava for Ava were measured at 2.3% and 89.1%, respectively. Moreover, BCN-Lipo-Ava remained stable under physiological conditions, without detectable accumulations for at least 24 h (fig. S2C). The resulting BCN-Lipo-Ava were rapidly and mildly reacted with DSPE-PEG_{5k}-Tre at room temperature in PBS within 0.5 h (fig. S2D), similar to the reaction of DSPE-PEG_{5k}-Tre and DSPE-BCN, as evidenced by ultraviolet spectroscopy (fig. S2A), which indicated the potential of this anchor-click technology for engineering of living cell.

To develop effective and biocompatible anchor-click conditions for living-cell engineering, we examined a number of cellular anchor-click parameters, including anchor/click feeding concentrations and time. As demonstrated by CCK-8 analysis, no significant reduction in T-cell viability was observed when incubated with DSPE-PEG_{5k}-Tre (100 μg) and BCN-Lipo-Ava

(Ava Conc: 100 μg/mL) up to 24 h, indicating the cytocompatibility of these two modules (fig. S3, A and B). Notably, when the feeding concentration of BCN-Lipo-Ava was fixed at 100 μg/mL, the amount of Ava in T-Tre/BCN-Lipo-Ava cells increased from 1 to 4 μg per million cells and then plateaued, as the feeding amount of anchor module-DSPE-PEG_{5k}-Tre increased. The feeding amount of DSPE-PEG_{5k}-Tre at plateau point was at 80 μg (fig. S3, C and D). Lastly, we found that, the time of anchor and click both positively contributed to the amount of Ava in T-Tre/BCN-Lipo-Ava cells within a certain time-less than 10 min for anchor and shorter than 30 min for click (fig. S3, E and F). Collectively, for all the following generations of T-Tre/BCN-Lipo-Ava cell, unless it was specifically stated, the feeding amounts of DSPE-PEG_{5k}-Tre and BCN-Lipo-Ava were set as 80 μg and 100 μg/mL, while the time of anchor/click was fixed at 10 min and 30 min, respectively. The total number of liposomes anchored on the surface of T cells was approximately 275 liposomes per T cell, as measured by nanoparticle tracking analysis, with nearly 4 μg Ava per million cells (table S1 and fig. S3C).

Having demonstrated the cytocompatibility and efficacy of this anchor-click based living-cell engineering, we next explored the generation and morphology of resulted T-Tre/BCN-Lipo cell. To this end, DSPE-PEG_{5k}-Tre and BCN-Lipo were tagged by fluorescein isothiocyanate and Rhodamine, respectively (FITC-DSPE-PEG_{5k}-Tre and BCN-Lipo-RhoB). Besides, fluorescence-tagged lipid and liposome without clickable groups (FITC-DSPE-PEG_{5k} and Lipo-RhoB) were also prepared as controls. As displayed in Fig. 1B, T-Tre/BCN-Lipo-RhoB cell showed the highest fluorescent intensity in comparison with those of T/BCN-Lipo-RhoB cell and T-Tre/Lipo-RhoB cell, which indicated the anchor of liposomes onto T-cell surface was largely owing to DSPE-PEG_{5k}-Tre anchor and the subsequent click reaction, rather than physical absorption. Further, as evidenced by fluorescent images of T-FITC-Tre/BCN-Lipo-RhoB cell

along with the corresponding correlation coefficients (Fig. 1, C and D), FITC-DSPE-PEG$_{5k}$-Tre, T-cell surface marker-CD8, and BCN-Lipo-RhoB, colocalized well, suggesting the successful anchor of DSPE-PEG$_{5k}$-Tre into cell surface, and the subsequent introduction of BCN-Lipo onto cell surface via click reaction of Tre and BCN. In contrast, no such colocalized signal was observed in T-FITC/BCN-Lipo-RhoB cell, due to lack of Tre groups inserted on cell surface. To better visualize the morphology of T-Tre/BCN-Lipo cell, the scanning electron microscopy images (SEM) were obtained. Of note, the BCN-modified gold nanoparticles instead of BCN-Lipo were used, owing to the structure of BCN-Lipo that was fragile to dehydration during the preparation of SEM sample. In Fig. 1E, a considerable amount of gold nanoparticles was tightly restricted on the T-cell surface, as pointed by red arrows.

Next, we investigated the stability of T-Tre/BCN-Lipo-Ava cell, especially the retention of BCN-Lipo-Ava on T-cell surface. RhoB-tagged BCN-Lipo-Ava stayed attached on the surface of T-Tre/BCN-Lipo-Ava cell up to 4 days as evidenced by confocal microscopy imaging (Fig. 1F), which likely resulted from the strong hydrophilicity and steric hindrance of PEG chain in the anchor module-DSPE-PEG$_{5k}$-Tre. Approximately 50% and 30% of initial anchoring liposomes is retained on T-Tre/BCN-Lipo-Ava cell at day 2 and day 4, respectively, according to the flow cytometry (Fig. 1G and fig. S4). In addition, approximately 50% of the backpacked Ava was stably restricted on the surface of T-Tre/BCN-Lipo-Ava cell after 48 h culture in fetal bovine serum (FBS)-free or 50% FBS-contained 1640 medium at 37°C (Fig. 1, H and I). Taken together, these data demonstrated a superior stability of T-Tre/BCN-Lipo-Ava cell with respect to not only the retention of liposomes on cell surface but also the entrapment of Ava in the retained liposomes.

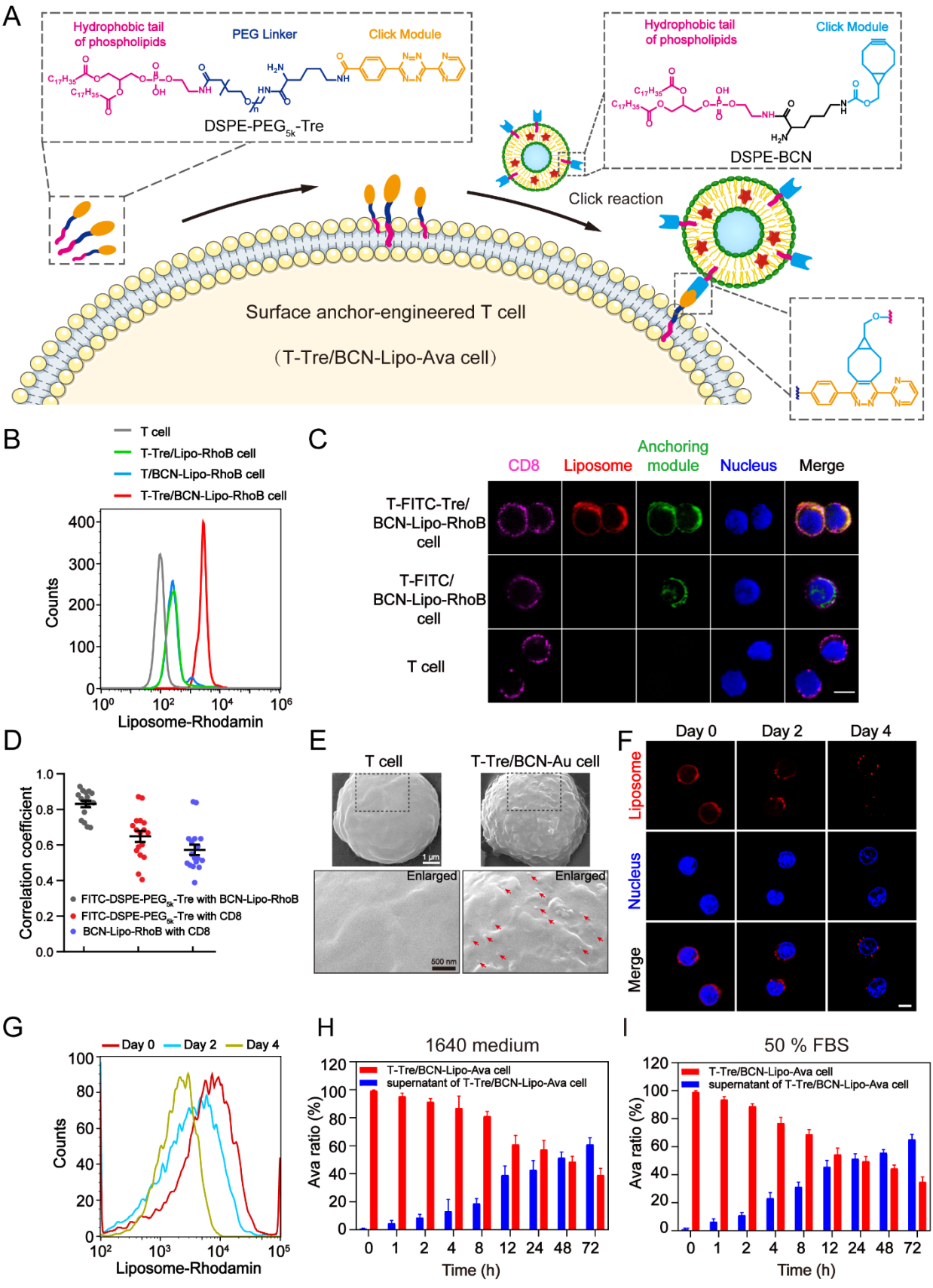
A
Hydrophobic tail of phospholipids
PEG Linker
Click Module
DSPE-PEG5k-Tre
Hydrophobic tail of phospholipids
Click Module
DSPE-BCN
Click reaction
Surface anchor-engineered T cell
(T-Tre/BCN-Lipo-Ava cell)
B
T cell
T-Tre/Lipo-RhoB cell
T/BCN-Lipo-RhoB cell
T-Tre/BCN-Lipo-RhoB cell
Counts
Liposome-Rhodamin
C
CD8
Liposome
Anchoring module
Nucleus
Merge
T-FITC-Tre/ BCN-Lipo-RhoB cell
T-FITC/ BCN-Lipo-RhoB cell
T cell
D
Correlation coefficient
FITC-DSPE-PEG5k-Tre with BCN-Lipo-RhoB
FITC-DSPE-PEG5k-Tre with CD8
BCN-Lipo-RhoB with CD8
E
T cell
T-Tre/BCN-Au cell
Enlarged
Enlarged
F
Day 0
Day 2
Day 4
Liposome
Nucleus
Merge
G
Day 0
Day 2
Day 4
Counts
Liposome-Rhodamin
H
1640 medium
T-Tre/BCN-Lipo-Ava cell
supernatant of T-Tre/BCN-Lipo-Ava cell
Ava ratio (%)
Time (h)
I
50 % FBS
T-Tre/BCN-Lipo-Ava cell
supernatant of T-Tre/BCN-Lipo-Ava cell
Ava ratio (%)
Time (h)

Fig. 1. Generation and characterizations of T-Tre/BCN-Lipo-Ava cell. (A) Schematic diagram of generation of cell-surface anchor-engineered T cell (referred as T-Tre/BCN-Lipo cell). **(B)** Flow cytometry analysis of T-Tre/Lipo-RhoB cell, T/BCN-Lipo-RhoB cell, and T-Tre/BCN-Lipo-RhoB cell, using T cell as the control (n = 3 independent samples per group). **(C)** Fluorescence images of T-FITC-Tre/BCN-Lipo-RhoB cell, T-FITC/BCN-Lipo-RhoB cell and T cell. All cells were co-stained with APC-Cy7-conjugated anti-CD8α Ab and Hoechst 33342. Scale bar, 5 μm (n = 2 independent experiments). **(D)** Pearson's correlation coefficients for FITC-DSPE-PEG_{5k}-Tre *v.s.* BCN-Lipo-RhoB, FITC-DSPE-PEG_{5k}-Tre *v.s.* APC-Cy7-anti-CD8α, and BCN-Lipo-RhoB *v.s.* APC-Cy7-anti-CD8α, as shown in **(C)**. n = 17 cells. Values >0.5 indicate colocalization of two fluorescent signals. **(E)** SEM of T-Tre/BCN-Au cell and T cell. Red arrows indicate BCN-Au nanoparticles. **(F)** Confocal microscopy images of T-Tre/BCN-Lipo-Ava cell after *in vitro* expansion for 2 days and 4 days. Scale bar, 5 μm (n = 2 independent experiments). **(G)** Flow cytometry analysis of T-Tre/BCN-Lipo-RhoB cell expansion at 37°C for 2 days and 4 days, using freshly prepared T-Tre/BCN-Lipo-RhoB cell as control (n = 3 independent samples per group). **(H-I)** The percentages of Ava in T-Tre/BCN-Lipo-Ava cell, which were cultured in 1640 medium containing no **(H)** or 50% FBS **(I)** for different incubation time, n = 3 independent samples per group. Error bars denote SEM.

Key physiological functions of T-Tre/BCN-Lipo-Ava cell *in vitro*

The viability of T-Tre/BCN-Lipo-Ava cells was monitored over 10 days via trypan blue staining. As shown in Fig. 2A, the viability of T-Tre/BCN-Lipo-Ava cells was all higher than 80% during 10 days and the apoptosis rate of T-Tre/BCN-Lipo-Ava cell was measured at 2.81% on day 10 (fig. S5), which demonstrated an unimpaired viability of T-Tre/BCN-Lipo-Ava cell. The in *vitro*

expansion of T-Tre/BCN-Lipo-Ava cells after stimulated by anti-CD3/CD28 antibodies, presented a comparable level as that of T cells, nearly 20 folds on day 10, and this robust and unimpaired proliferative capacity of T-Tre/BCN-Lipo-Ava cell was further verified by the gradually decreased fluorescence intensity of carboxyfluorescein succinimidyl ester (CFSE)-labelled T-Tre/BCN-Lipo-Ava cell, as analyzed by fluorescence activating cell sorter (FACS) (Fig. 2, B and C).

Next, we observed no reduction in trans-endothelia migration capacity of T-Tre/BCN-Lipo-Ava cell compared with T cell (38% *v.s.* 40%, Fig. 2D). Additionally, the chemotaxis behavior of T-Tre/BCN-Lipo-Ava cell was studied, using monocyte chemoattractant protein-1 (MCP-1) as the chemoattractant agent (*27*). As presented in Fig. 2E, the chemotaxis migrations of T-Tre/BCN-Lipo-Ava cell and T cell were both positively related to MCP-1 concentration and the percentages of migrated T-Tre/BCN-Lipo-Ava cell and T cell were calculated at 17% and 19%, respectively, when the concentration of MCP-1 was at 100 ng/mL, indicating an intact chemotaxis capacity of T-Tre/BCN-Lipo-Ava cell. Given T-Tre/BCN-Lipo-Ava cell could reshape their cytoskeletons and consequently the cell membrane during migration (*33*), which may lead to a loss of backpacked Ava, we next sought to figure out the amount of Ava in the migrated T-Tre/BCN-Lipo-Ava cells. Compared to 4 μg per million cells of freshly-prepared T-Tre/BCN-Lipo-Ava cells, we observed a small reduction in the amount of Ava-maintained in the migrated T-Tre/BCN-Lipo-Ava cells, with 3.37 μg per million cells (fig. S6, A and B), which fulfilled the dosage requirement for *in vivo* application (*16*).

Moreover, we found that, the surface expressions of CD69 (an activation marker of T cell) (*34-36*) on T-Tre/BCN-Lipo-Ava cell and T cell were both low under quiescent condition (without stimulation), and increased by the same extent in response to anti-CD3/CD28 antibodies

stimulation, which suggested the condition of T-Tre/BCN-Lipo-Ava cell, just as T cell, was solely dependent the exogenous immune stimuli rather than the engineering process/agents (Fig. 2F). Additionally, the secretion of cytokines (IL-2, IFNγ, and TNFα) by concanavalin A (ConA)-stimulated T-Tre/BCN-Lipo cell was comparable to that of T cell, but far less than that of T-Tre/BCN-Lipo-Ava cell and T cell plus free Ava (Fig. 2, G, H and I, and fig. S7), indicating that the backpacked Ava could improve the T cell function while the insert process of BCN-Lipo had no effect on cytokine secretion.

We further examined the basal energy metabolism of T-Tre/BCN-Lipo-Ava cell. Mitochondrial oxygen consumption rate (OCR) and extracellular acidification rate (ECAR) of T-Tre/BCN-Lipo-Ava cell and unconjugated T cell were comparable (fig. S8), further confirming that the engineering technology was benign without affecting the basal oxidative phosphorylation and glycolysis.

Despite the survival, chemotaxis/migration ability, activation, cytokine secretion and basal energy metabolism of T-Tre/BCN-Lipo-Ava cell was remained unaffected, the influences on other proteins related to key physiological functions of T cell after engineering were unclear. To clarify this, mass spectrometry was performed to examine T cell proteome alterations. We studied the overall proteome changes between T-Tre/BCN-Lipo cell (without drug loading) and unconjugated T cell by Tandem Mass Tag (TMT)-based quantitative proteomics. The result exhibited that only a total of 7 proteins within 7226 all proteins showed more than 1.5-fold change in abundance, suggesting very few proteins were affected by the cell surface anchoring engineering. Of note, the expression of most proteins enriched in the biological process of TCR signaling, T cell activation, T cell proliferation, and immune effector process remain unchanged

(fig. S9), suggesting that central molecular signatures related to T cell function remain unaffected.

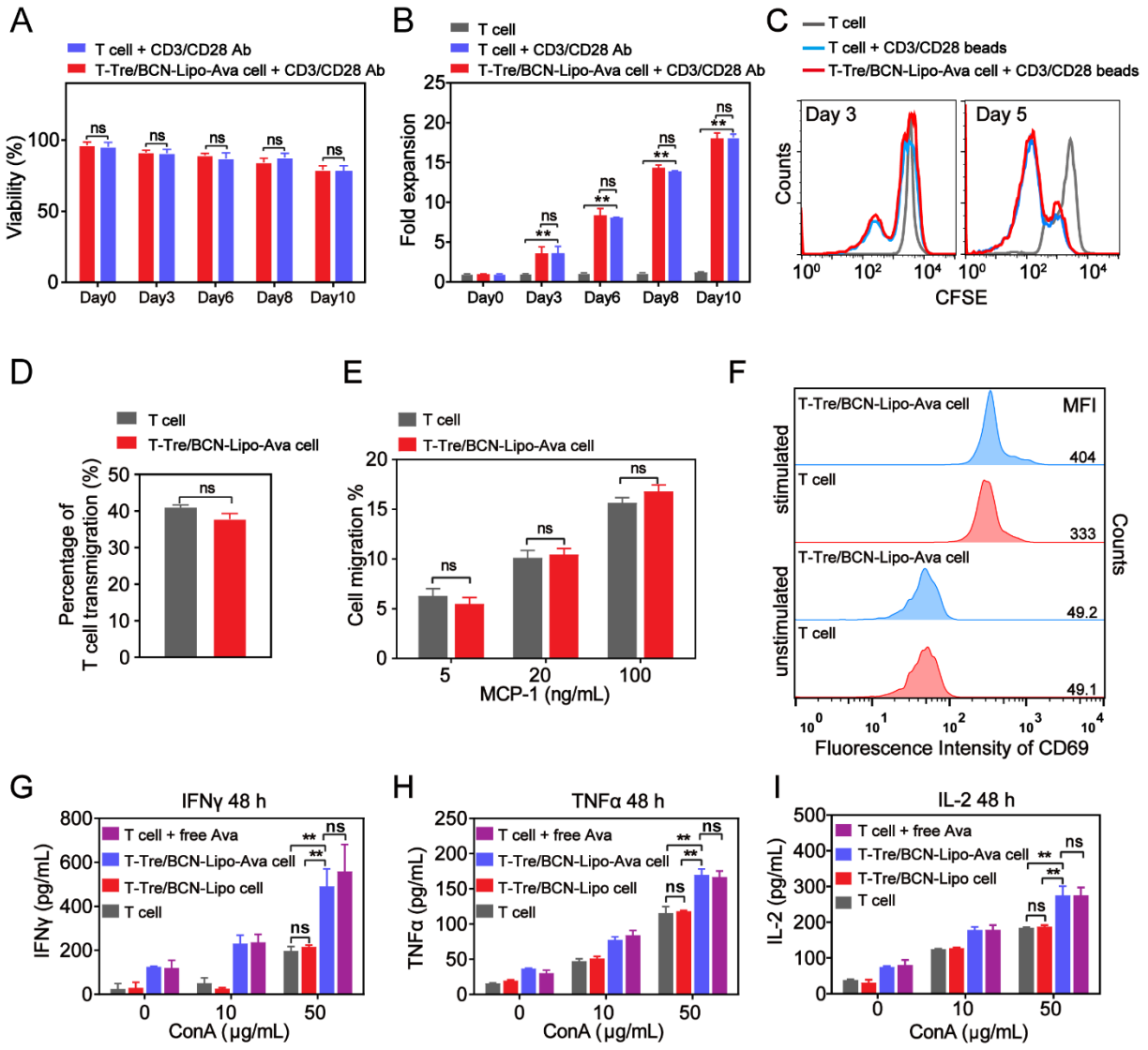

Fig. 2. T-Tre/BCN-Lipo-Ava cell maintained key physiological functions of T cell. (A) Viability of T-Tre/BCN-Lipo-Ava cells for 10 days after stimulated with anti-CD3 and anti-CD28 antibodies (CD3/CD28 Abs) (n = 3 independent samples per group). **(B)** *In vitro* expansion of T-Tre/BCN-Lipo-Ava cells after stimulation. Naive and stimulated T cells were used as controls (n = 3 independent samples per group). **(C)** The proliferative profile of T-

Tre/BCN-Lipo-Ava cells after stimulation, using T cells with and without stimulation as controls (n = 3 independent samples per group). **(D-E)** Transwell-assay of trans-endothelia **(D)** and chemotaxis migration **(E)** behaviors of T-Tre/BCN-Lipo-Ava cell using MCP-1 as the chemoattractant agent (n = 3 independent samples per group). **(F)** Flow cytometry analysis of CD69 expression on cell surface with and without stimulation (n = 3 independent samples per group). **(G-I)** The improved secretion of inflammatory cytokines including IFNγ **(G)**, TNFα **(H)** and IL-2 **(I)** after stimulation for 48 h with concanavalin A (Con A) (n = 3 independent samples per group). Data were analyzed by unpaired t-test. Error bars denote SEM, $^{**}P < 0.01$ and ns means no significant difference.

The antitumor responses of T-Tre/BCN-Lipo-Ava cell *in vitro*

The cytotoxicity of T-Tre/BCN-Lipo-Ava cell towards tumor cells was evaluated via the co-culture of pmel-1 $CD8^+$ T cells derived from pmel-1 TCR transgenic mice with melanoma cells (B16F10 cells) at an effector: target ratio of 10:1 for different co-culture time. As shown in Fig. 3A, T-Tre/BCN-Lipo-Ava cell killed nearly 80% of co-cultured B16F10 cells compared to 50% of T cell, when the co-incubation time was at 48 h. In contrast, pre-treatment of $CD8^+$ T cells with Ava (pre-Ava T cell) only yielded modest toxicity against B16F10 cells, whereas T cell plus free Ava demonstrated the comparable toxicity as that of T-Tre/BCN-Lipo-Ava cell. We believed that the duration of Ava action led to improved cytotoxicity of T cell through inhibiting their ACAT1 expression. However, it was reported that Ava could directly inhibit the growth of tumor cells by targeting tumor cell-derived ACAT1 (*37*). To clarify this issue, we first determined the ACAT1 expression of B16F10 melanoma and glioblastoma LN-229 cells as well as their established tumors (fig. S10 A and B). These two types of cancer cells chosen in our

study expressed relatively low levels of ACAT1 protein compared with PC-3 prostate cancer cells which express high level of ACAT1 protein as previously reported (*37*). Treatment with the concentration of Ava under 10 μM remains normal viability of B16F10 and LN-229 cells (fig. S10 C and D), confirming that the inhibition of cancer cell growth is not driven by the cytotoxicity of Ava to cancer cells, but rather by potentiated T cell antitumor response.

Moreover, we believed the augmented antitumor responses of T-Tre/BCN-Lipo-Ava cell were owing to enhanced TCR clustering and immunological synapse formation mediated by increased membrane cholesterol content-as a result of combinatorial Ava suppressing ACAT1 activities (Fig. 3B). To verify our assumptions, we first measured the cholesterol content and found backpacked Ava on T-Tre/BCN-Lipo-Ava cell significantly increased cholesterol levels (fig. S11). Consistent with previous report (*16*), the increased cholesterol content was ascribed to the inhibited conversion of cholesterol to cholesteryl esters and the modestly enhanced cholesterol biosynthesis (fig. S12). Then, we checked whether increased cholesterol is causative for the augmented antitumor responses by adding or depleting cholesterol to the plasma membrane. The results showed that addition of plasma membrane cholesterol led to potentiated effector function, which was consistent with enhanced effector function induced by free Ava or backpacked Ava (fig. S13, A-C), while depletion of plasma membrane cholesterol led to impaired effector function of T-Tre/BCN-Lipo-Ava cell (fig. S13, D-F). These data further indicated the critical role of increased cholesterol in antitumor responses. Next, TCR and the consequent downstream signal, phosphorylated ζ-chain-associated protein kinase 70 (pZAP-70) after stimulation in T-Tre/BCN-Lipo-Ava cell, T cell and T cell plus free Ava, were examined at cellular level via Alexa Fluor 647-anti-TCRβ and Alexa Fluor 488-anti-pZAP70 double-staining. As presented in Fig. 3C, a stronger as well as highly-colocalized fluorescent signals were

observed on the surface of T-Tre/BCN-Lipo-Ava cell, compared to that of T cell. This improved TCR signals of T-Tre/BCN-Lipo-Ava cell with stimulation including p-CD3, p-ZAP70 as well as p-Erk1/2 was also verified at molecular level as evidenced by the western blot (Fig. 3D and fig. S14). To further study the distribution and structure of TCRs on T-cell membrane, the super-resolution imaging was utilized. Fig. 3E and the corresponding qualitative results (Fig. 3F) showed that, T-Tre/BCN-Lipo-Ava cell had a significantly larger TCR microcluster compared to that of T cell, which can improve the interactions between T-Tre/BCN-Lipo-Ava cell and tumor antigen via the augmented avidity and result in a bigger TCR signalosome. Moreover, the formation of immunological synapse in T-Tre/BCN-Lipo-Ava cell was investigated, since the cholesterol was the key component of immunological synapse (*13*). Using total internal reflection fluorescence imaging, we found that within the same experimental time, the TCRs of T-Tre/BCN-Lipo-Ava cell were more compact in the center of immunological synapse with a smaller area, indicating a faster maturation of immunological synapse compared with T cell (Fig. 3, G and H).

Having demonstrated the backpacked Ava could potentiate the anti-tumor responses of T-Tre/BCN-Lipo-Ava cell via the improved TCR clustering and immunological synapse formation, likely in a psueo-autocrine manner, we next sought to figure out whether the backpacked Ava by T-Tre/BCN-Lipo-Ava cell would potentiate the anti-tumor responses of endogenous microenvironmental T cell in a pseudo-paracrine manner, which may offer an additional benefit to treat solid tumor, in which most of the infiltrating T cells were metabolic insufficiency (*38*). In pursuit of this, we cultured T cells in T-Tre/BCN-Lipo-Ava cell- or T cell- conditioned medium (CM) and subsequently stained the cell membrane cholesterol by Filipin III (*16*). Fig. 3I suggested a higher content of T-cell-membrane-cholesterol content cultured in T-Tre/BCN-Lipo-

Ava cell- CM with a strong Filipin III fluorescence. To confirm this finding, we quantified the plasma-membrane-cholesterol content using an oxidation-based assay, which showed that the cholesterol content in T-cell membrane doubled when cultured in T-Tre/BCN-Lipo-Ava cell-CM, compared with T cells in T-cell CM (Fig. 3J). Collectively, we believed that the backpacked Ava could inhibit the esterification of cholesterol inside adoptive T-Tre/BCN-Lipo-Ava cells and endogenous T cells in a pseudo-paracrine/autocrine manner, thereby a maximum synergistic anti-tumor response between Ava and T cell as well as a reinvigorated exogenous T-cell effector functions was achieved.

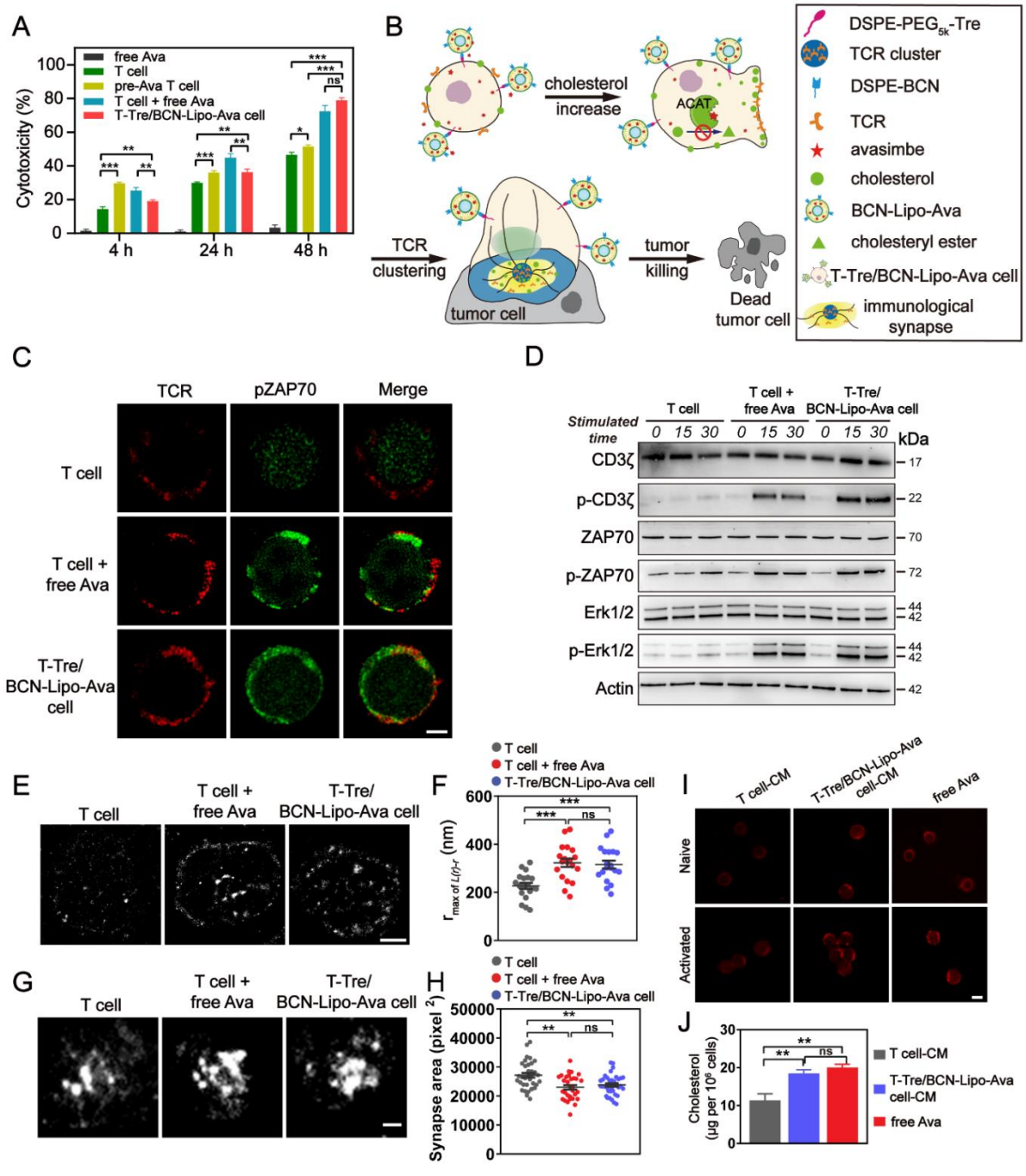

Fig. 3. T-Tre/BCN-Lipo-Ava cell displayed enhanced TCR clustering and immunological synapse formation, and consequently improved antitumor responses. (A) The cytotoxicity against B16F10 tumor cells, n = 4 independent samples per group. **(B)** The proposed mechanism of enhanced anti-tumor responses of T-Tre/BCN-Lipo-Ava cell. **(C)** Representative fluorescence

images of TCR and its downstream signal pZAP-70 after stimulation with anti-CD3/CD28 Abs using stimulated emission depletion microscopy. All the cells were stained with anti-TCRβ-Alexa Fluor 647 and anti-pZAP-70-Alexa Fluor 488. Scale bar, 2 μm. **(D)** Immunoblotting of proximal and downstream TCR signaling molecules after stimulation with anti-CD3/CD28 Abs (n = 3 independent experiments). Super-resolution STORM images **(E)** and quantification **(F)** of TCR clustering. Scale bar, 2 μm. Graph shows *r* value at the maximal *L(r)-r* value of Ripley's *K*-function curves (n = 20), representing the cluster size with the highest probability, where *L(r)-r* represents the efficiency of molecule clustering, and *r* represents cluster radius (n = 2 independent experiments). Total internal reflection fluorescence microscopy images **(G)** and quantification **(H)** of the immunological synapse size. Total synapse areas were quantified using the entire signal from each field. Scale bar, 2 μm. **(I)** Fluorescence microscopy images of Filipin III-stained naive or activated $CD8^+$ T cells incubated with T-Tre/BCN-Lipo-Ava cell-CM or T cell-CM for 12 h. Scale bar, 5 μm (n = 2 independent experiments). **(J)** Quantification of plasma membrane cholesterol content in $CD8^+$ T cells using an oxidation-based method, n = 3 independent samples per group. Data were analyzed by unpaired t-test. Error bars denote SEM, $*P < 0.05$, $**P < 0.01$, $***P < 0.001$ and ns means no significant difference.

Combination treatment *via* T-Tre/BCN-Lipo-Ava cell against primary solid tumor

We first analyzed the homing of T-Tre/BCN-Lipo-Ava cell and accumulation of Ava in primary melanoma, via adoptive transferring melanoma-specific pmel-1 $CD8^+$ T cells, which carry T cell receptor transgenes specific for the mouse homologue (pmel) of human premelanosome protein (gp100) (*39*). The population of transferred T cells and Ava concentrations in tumor were measured by flow cytometry and high-performance liquid chromatography (HPLC) over time, respectively. We found that substantial T-Tre/BCN-Lipo-Ava cells accumulated in tumor by 4 h,

reaching peak levels by 48 h with similar kinetics to unconjugated T cells, indicating that surface-anchoring did not affect the survival or trafficking of transferred T cells (fig. S15, A and B). The drug concentration of backpacked Ava peaked at 48 h after adoptive transfer with a similar pattern of T-Tre/BCN-Lipo-Ava cell (fig. S15C), and exhibited 200-fold greater than free Ava and 8-fold greater than BCN-Lipo-Ava at 48 h, remaining at high levels for at least 3 days. It implied that BCN-Lipo-Ava remained stable and retained on T cell surface during the trafficking to tumor and might strengthen the T cell effect due to the extended and sufficient Ava action.

We next evaluated the antitumor efficacy of proposed combination treatment mediated by pmel-1 $CD8^+$ T-Tre/BCN-Lipo-Ava cell (T-Tre/BCN-Lipo-Ava cell) *in vivo*. The orthotopic melanoma mouse model was first established via intradermal injection of B16F10 cells into wild-type C57BL/6 mice. The mice were randomly divided into nine groups, lymphodepleted on day 6 and received two intravenous injections on post-tumor-implantation day 8 and 14, with one of the following formulations: (i) saline; (ii) free Ava; (iii) BCN-Lipo-Ava, (iv) T cell, (v) T-Tre/BCN-Lipo cell, (vi) pre-Ava T cell, (vii) T cell plus free Ava, , (viii) T cell plus BCN-Lipo-Ava, and (ix) T-Tre/BCN-Lipo-Ava cell (Fig. 4A). Then the tumor growth was monitored by tumor volume. T-Tre/BCN-Lipo-Ava cell treated mice showed the slowest rate of tumor growth (Fig. 4B), compared with monotherapies. Moreover, tumors harvested from mice on day 20 were immunohistochemically stained to analysis the expression of Ki-67 (a proliferation marker). As presented in Fig. 4, C and D, the minimum Ki-67 positive tumor cells were observed in T-Tre/BCN-Lipo-Ava cell treated group, around half of those for T cell treated mice and one third of those in mice receiving free Ava. In consistence with growth and proliferation profiles of tumor, fifty percent of mice receiving T-Tre/BCN-Lipo-Ava cell survived for at least 63 days,

compared to 28 days of saline-treated mice (Fig. 4E). Notably, the combinatory administration of the blend of T cell and BCN-Lipo-Ava, namely T cell plus BCN-Lipo-Ava, inhibited the tumor growth moderately compared with T-Tre/BCN-Lipo-Ava cell, with no mice surviving after 53 days (Fig. 4E). Even Ava-pretreated T cell (pre-Ava T cell) exhibited moderate anti-tumor effect due to the lack of sustained Ava action (Fig. 4E). Additionally, none of the treatments caused significant loss of body weights (Fig. 4F) and tissue damage (fig. S16-S20), and adoptively transfer of T-Tre/BCN-Lipo-Ava cell induced neither systemic cytokine release (IL-10, IL-6, TNFα), nor the expressions of markers of liver/kidney injury (aminotransferases, alkaline phosphatase, blood urea nitrogen; fig. S21).

The superior antitumor efficacy of combination therapy mediated by OT-I $CD8^+$ T-Tre/BCN-Lipo-Ava cell (T-Tre/BCN-Lipo-Ava cell) was further confirmed in a second tumor model via intradermal injection of ovalbumin (OVA)-expressing B16F10 melanoma cells (B16F10-OVA) into wild-type C57BL/6 mice (fig. S22A). The measurement of tumor growth curves, survival curves and body weights of tumor-bearing mice as well as the immunohistochemistry of Ki-67 staining in tumor sections were also performed. Combination treatment via OT-I $CD8^+$ T-Tre/BCN-Lipo-Ava cells (also refers as T-Tre/BCN-Lipo-Ava cell) exhibited the best antitumor efficacy, markedly delayed tumor growth and significantly improved survival (fig. S22, B-E), while the body weight, systemic cytokine release and liver/kidney injury markers were comparable with other groups (fig. S22F and fig. S23). These results therefore indicated that T-Tre/BCN-Lipo-Ava cell afforded markedly improved treatment benefits against primary solid tumor *in vivo*, compared with monotherapies and even the combination treatment-mediated by the blend of T cell and Ava.

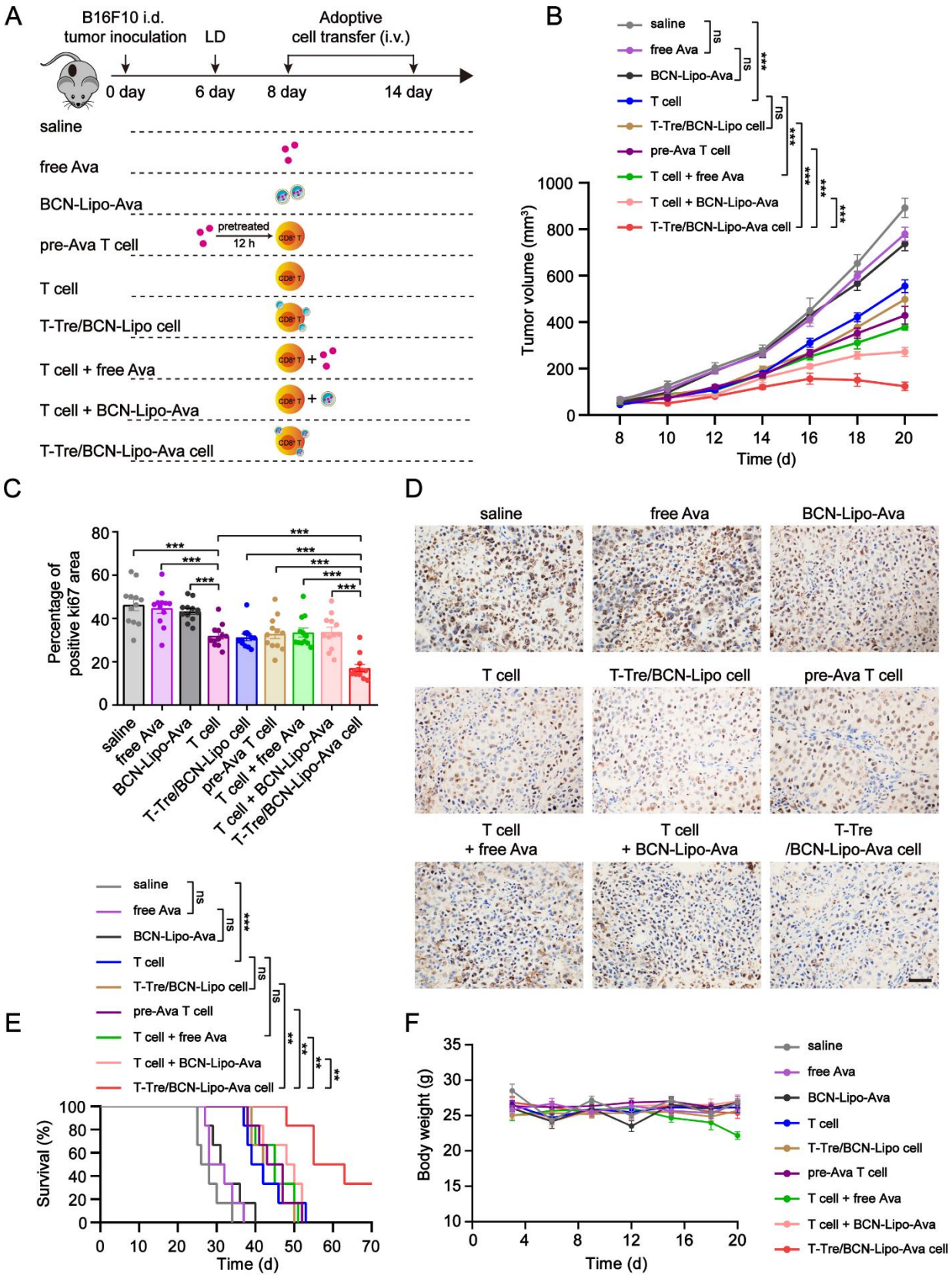
A
B16F10 i.d. tumor inoculation
LD
Adoptive cell transfer (i.v.)
0 day
6 day
8 day
14 day
saline
free Ava
BCN-Lipo-Ava
pre-Ava T cell
pretreated 12 h
T cell
T-Tre/BCN-Lipo cell
T cell + free Ava
T cell + BCN-Lipo-Ava
T-Tre/BCN-Lipo-Ava cell
B
Tumor volume (mm³)
Time (d)
C
Percentage of positive ki67 area
D
E
Survival (%)
Time (d)
F
Body weight (g)
Time (d)

Fig. 4. Optimized synergistic antitumor efficacy of pmel-1 CD8$^+$ T-Tre/BCN-Lipo-Ava cell in an orthotopic melanoma mouse model. (A) Schematic illustration of the experimental setting. **(B)** The tumor growth curves of mice receiving tested formulations, n = 6 mice/group. Representative quantification **(C)** and microscopic images **(D)** of tumor sections immunostained by Ki-67 and the Ki-67 positive areas were quantified from each field (n = 12). Scale bar, 50 μm. **(E)** The survival profiles of mice receiving tested formulations, n = 6 mice/group. **(F)** Body weights of all mice, n = 6 mice/group. Data were analyzed by one-way ANOVA **(B)**, unpaired t-test **(C)** or a log-rank (Mantel-Cox) test **(E)**. Error bars denote SEM, *$P < 0.05$, **$P < 0.01$, ***$P < 0.001$ and ns: no significant difference.

Anti-tumor responses of adoptive transferred and tumor-infiltrating CD8$^+$ T cell

The superior anti-tumor capacities of T-Tre/BCN-Lipo-Ava cell mediated combination therapy *in vivo* were believed to stem from the enhanced T cell effector functions mediated by intervention of cholesterol metabolism. To verify this hypothesis, we first isolated adoptively transferred pmel-1 CD8$^+$ T cells from primary melanoma tumors on day 12 post-inoculation (4 days after first treatment) and investigated their capacity to secrete inflammatory cytokines, including IFNγ, TNFα, and lytic enzyme granzyme B (GzmB). As displayed in Fig. 5, A and B, the intravenous injection of pre-Ava T cell slightly increased the percentage of IFNγ$^+$, TNFα$^+$ as well as GzmB$^+$ pmel-1 T cells in tumors, compared to that of T cell-treated mice, which was in agreement with its modest *in vitro* cytotoxicity and *in vivo* antitumor efficacy (Fig. 3A and Fig. 4B). Mice receiving the combination of pmel-1 T cell and BCN-Lipo-Ava (mediated by a simple blend, T cell plus BCN-Lipo-Ava) showed an improved percentage of IFNγ$^+$, TNFα$^+$ as well as GzmB$^+$ pmel-1 T cells, due to the moderate synergistic effect between T cell and Ava. In

contrast, the transferred T-Tre/BCN-Lipo-Ava cell displayed the maximum synergistic efficacy and the largest population of cytokine and cytolytic granule, likely due to the optimized action profile of Ava (fig. S15). The cholesterol content in the transferred T-Tre/BCN-Lipo-Ava cell was significantly greater compared to the T cell or the blend of T cell with BCN-Lipo-Ava (Fig. 5, C and D), which helps to explain backpacked Ava is required to maintain a high and sustained cholesterol levels for potent antitumor efficacy.

Importantly, when mice received combination therapy via pmel-1 T-Tre/BCN-Lipo-Ava cell, total tumor-infiltrating $CD8^+$ T cells exhibited the highest percentage of effector $CD8^+$ T cells (fig. S24, A and B) , Ki-67 and cholesterol level (fig. S24, C and D), indicating that backpacked Ava afforded a pseudo-paracrine action profile for Ava to increase the anti-tumor effect of tumor-infiltrating $CD8^+$ T cell. Similarly, the largest percentage of cytotoxic $CD8^+$ T cells in primary melanoma was witnessed by mice receiving OT-I $CD8^+$ T-Tre/BCN-Lipo-Ava cell (fig. S25).

Lastly, we assessed the exhaustion and immunosuppressive status of adoptive transferred pmel-1 T cells according to the expression of different markers for proliferation (Ki-67), T cell exhaustion (TIM-3, LAG-3 and TIGIT) and immunosuppressive (PD-1 and CTLA-4) in primary melanoma tumors. The results showed that the exhaustion and immunosuppressive markers presented comparable levels between pmel-1T-Tre/BCN-Lipo-Ava cell and the blend of pmel-1T cell and BCN- Lipo-Ava (fig. S26, A and B), while the Ki-67 level was increased (Fig. 5, C and D). Similar results including comparable population of $TIM\text{-}3^+$, $LAG\text{-}3^+$, $TIGIT^+$, $PD\text{-}1^+$, $CTLA\text{-}4^+$ $CD8^+$ T cell and highest level of Ki-67 and cholesterol in treatment of T-Tre/BCN- Lipo-Ava cell was observed, when compared with other treatment groups (fig. S24, C and D; fig. S26, C and D). Of note, in the group of combination treatment via T-Tre/BCN-Lipo-Ava cell, the

backpacked Ava markedly increased the cytokine and cytolytic granule production (IFNγ, TNFα and GzmB) of PD-1^{+}, TIM-3^{+} or TIGIT^{+} pmel-1 T cells (Fig. 5, E-G). Taken together, the results suggested that T-Tre/BCN-Lipo-Ava cell are not in an exhausted state and the backpacked Ava could potentiate their effector function of adoptively transferred T-Tre/BCN-Ava-Lipo cell in the tumor microenvironment by increasing the proliferative capacity and the cytokine and cytolytic granule production due to the metabolic intervention.

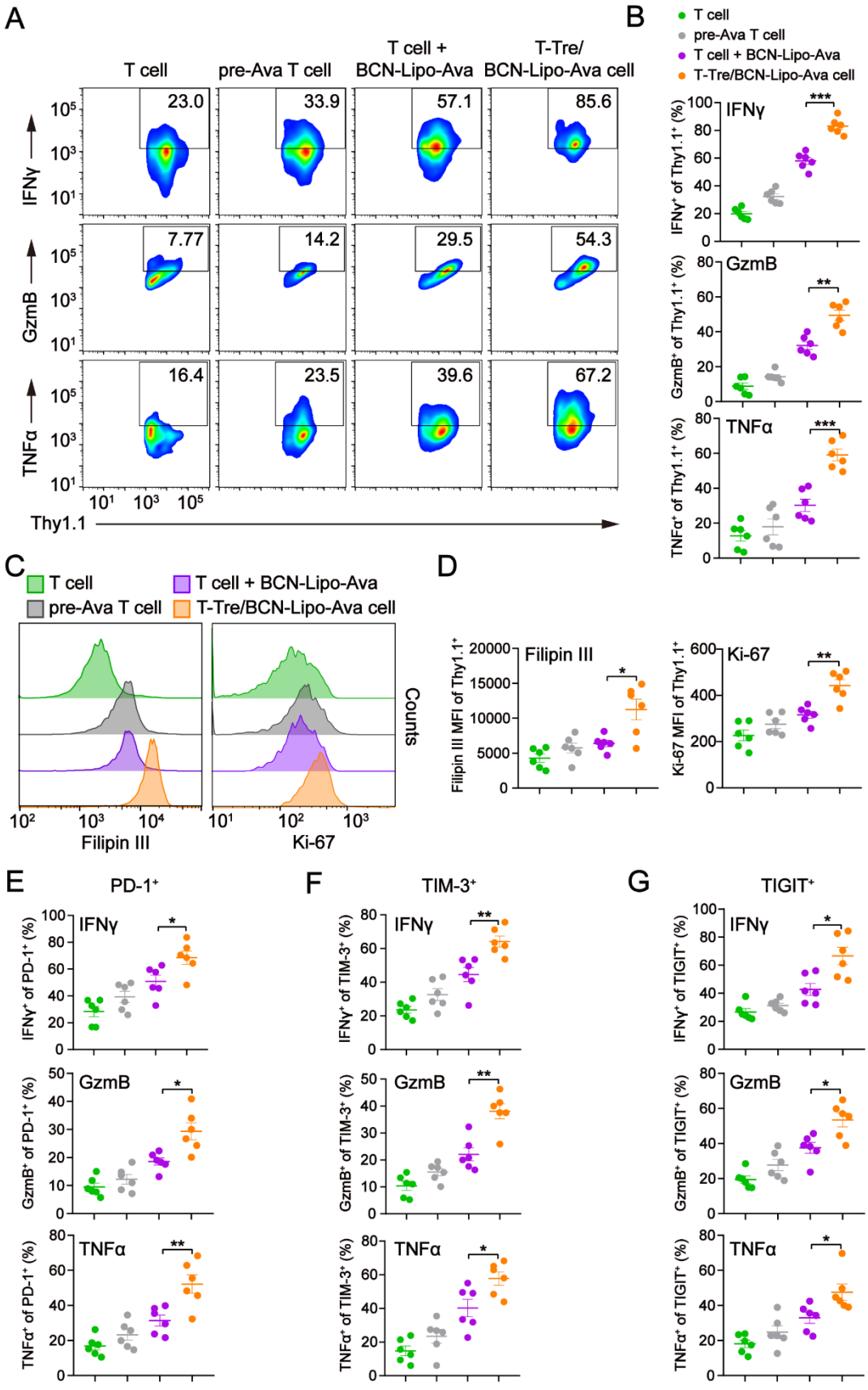
A
T cell
pre-Ava T cell
T cell + BCN-Lipo-Ava
T-Tre/ BCN-Lipo-Ava cell
IFNγ
GzmB
TNFα
Thy1.1
23.0
33.9
57.1
85.6
7.77
14.2
29.5
54.3
16.4
23.5
39.6
67.2
B
T cell
pre-Ava T cell
T cell + BCN-Lipo-Ava
T-Tre/BCN-Lipo-Ava cell
IFNγ
GzmB
TNFα
IFNγ+ of Thy1.1+ (%)
GzmB+ of Thy1.1+ (%)
TNFα+ of Thy1.1+ (%)
C
T cell
pre-Ava T cell
T cell + BCN-Lipo-Ava
T-Tre/BCN-Lipo-Ava cell
Filipin III
Ki-67
Counts
D
Filipin III
Filipin III MFI of Thy1.1+
Ki-67
Ki-67 MFI of Thy1.1+
E
PD-1+
IFNγ
GzmB
TNFα
IFNγ+ of PD-1+ (%)
GzmB+ of PD-1+ (%)
TNFα+ of PD-1+ (%)
F
TIM-3+
IFNγ
GzmB
TNFα
IFNγ+ of TIM-3+ (%)
GzmB+ of TIM-3+ (%)
TNFα+ of TIM-3+ (%)
G
TIGIT+
IFNγ
GzmB
TNFα
IFNγ+ of TIGIT+ (%)
GzmB+ of TIGIT+ (%)
TNFα+ of TIGIT+ (%)

Fig. 5. Tumor-infiltrating pmel-1 T cell displayed a more lethal phenotype in tumor after a single adoptive pmel-1 CD8$^+$ T-Tre/BCN-Lipo-Ava cell transfer. (A-B) Flow cytometry analysis and quantification the produced TNFα, IFNγ and GzmB of pmel-1 T cells in orthotopic melanoma tumors after injection the Thy1.1$^+$ pmel-1 T cell for 4 days, n = 6 mice/group. **(C-D)** Filipin III and Ki-67 level of tumor-infiltrating Thy1.1$^+$ pmel-1 T cells were assessed using flow cytometry, n = 6 mice/group. **(E-G)** Flow cytometry analysis the produced TNFα, IFNγ and GzmB of PD-1$^+$, TIM-3$^+$ and TIGIT$^+$ Thy1.1$^+$ pmel-1 T cells in orthotopic melanoma tumors, n = 6 mice/group. Data were analyzed by unpaired t-test. Error bars denote SEM, *P < 0.05, **P < 0.01, ***P < 0.001 and ns means no significant difference.

***In vivo* T-Tre/BCN-Lipo-Ava cell therapy against solid tumor metastasis**

To demonstrate the potential of combination therapy-mediated by T-Tre/BCN-Lipo-Ava cell to treat solid tumor metastasis, an experimental metastasis model by intravenously injecting mice with Luciferase-expressing B16F10-OVA cells was utilized. The treatment regimen was identical to that for primary solid tumor, except that the development of metastasis was monitored via the bioluminescence of B16F10-OVA cells. We found that, mice receiving combination therapy-mediated by OT-I CD8$^+$ T-Tre/BCN-Lipo-Ava cell (T-Tre/BCN-Lipo-Ava cell) displayed the fewest lung and bone metastasis compared with mice receiving monotherapies and even the combination therapy-mediated by a simple blend (Fig. 6A). Moreover, the H&E staining of lungs harvested from mice receiving tested formulations confirmed the superior anti-metastasis capacity of T-Tre/BCN-Lipo-Ava cell with the smallest amount and size of lung-metastatic tumor (Fig. 6, B and C, and fig. S27). Consistently, 60% of mice receiving T-Tre/BCN-Lipo-Ava cell survived at least 60 days. In contrast, no other mice survived after 60

days except for the T cell plus BCN-Lipo-Ava treated mice, of whom only 20% survived after 60 days (Fig. 6D). Moreover, the adoptive transfer of T-Tre/BCN-Lipo-Ava cell did not provoke significant systemic inflammation and cause detectable damages to major organs, including liver, kidney and spleen, as evidenced by ELISA analysis, the blood biochemical analysis along with the examinations of liver and kidney functions (fig. S28). Lastly, the production of cytokine and cytolytic granule release of $CD8^+$ T cell were determined. Consistent with the results observed in primary melanoma (fig. S24 and fig. S25), the largest percentage of $IFN\gamma^+$, $TNF\alpha^+$ and $GzmB^+$ producing $CD8^+$ T cells in pulmonary metastatic melanoma was witnessed by mice receiving OT-I $CD8^+$ T-Tre/BCN-Lipo-Ava cell (fig. S29).

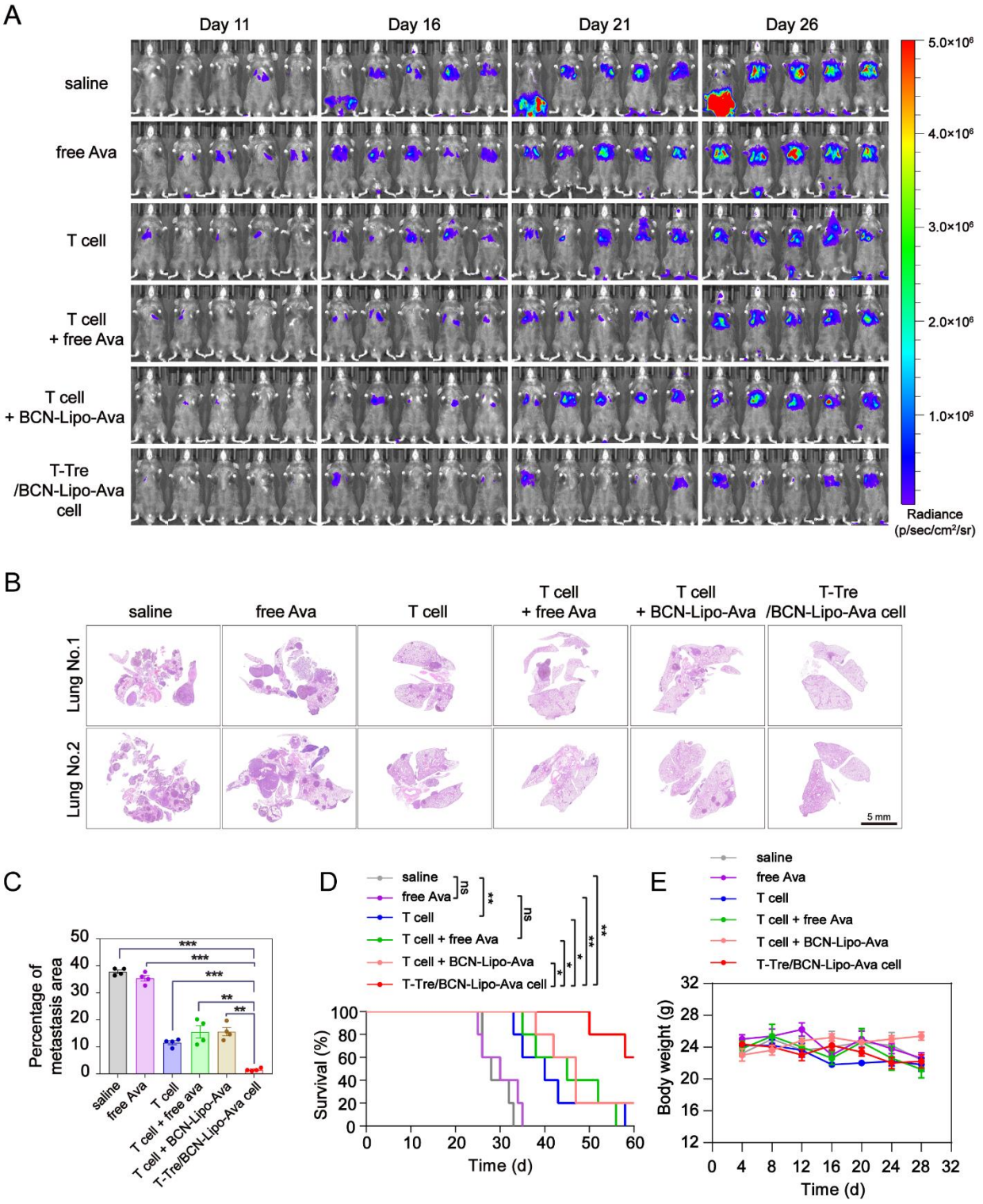

Fig. 6. Enhanced anti-metastasis efficacy of OT-I CD8⁺ T-Tre/BCN-Lipo-Ava cell in an experimental metastasis mouse model. (A) *In vivo* bioluminescence images of mice bearing

melanoma tumors, n = 5 mice/group. **(B-C)** The representative microscopic H&E stained images and quantification of lung sections harvested from mice receiving tested formulations. Whole lung sections were photographed and were further evaluated for tumoral area, n = 4. **(D)** The survival profiles of mice receiving tested formulations, n = 5 mice/group. **(E)** Body weights of all mice, n = 5 mice/group. Data were analyzed by unpaired t-test **(C)** or a log-rank (Mantel-Cox) test **(D)**. Error bars denote SEM, $*P < 0.05$, $**P < 0.01$, $***P < 0.001$ and ns means no significant difference.

***In vivo* T-Tre/BCN-Lipo-Ava cell therapy of highly-aggressive brain solid tumor**

Encouraged by the promising anti-tumor and metastasis capacities of T-Tre/BCN-Lipo-Ava cell-mediated combination therapy, we extended its application into the treatment of highly-aggressive brain solid tumor-orthotopic mouse model of human glioblastoma LN-229 (which expressed GD-2, fig. S30) in our setting (Fig. 7A). To this end, we first generated a disialoganglioside GD2 targeted CAR-T cells, of which detailed fabrication and characterizations were displayed in fig. S31 according to previous reports (*40*). And the fabrication of CAR T-Tre/BCN-Lipo-Ava cell followed the identical procedures as shown in Fig. 1, except for the CAR-T cells used (fig. S32, also referred as T-Tre/BCN-Lipo-Ava cell). Based on the bioluminescence of LN-229 cells, we found mice receiving T-Tre/BCN-Lipo-Ava cell displayed the most controlled tumor growth with 3 out of 5 showing no detectable tumor. And mice treated by the combination of CAR-T cell and BCN-Lipo-Ava (mediated by a simple blend, T cell plus BCN-Lipo-Ava) displayed a delayed tumor growth, but the growth could not be prevented. The anti-tumor capacities of monotherapies, including free Ava and CAR-T cell were limited, almost comparable to that of saline (Fig. 7B). The mice receiving T-Tre/BCN-Lipo-Ava

cell experienced a 60% survival rate after 100 days, but mice from other groups survived no more than 70 days, as presented in Fig. 7C. Further, we observed no significant loss of body weights (Fig. 7D), nor significantly evaluated systemic cytokine levels (Fig. 7, E-G) in mice receiving T-Tre/BCN-Lipo-Ava cell, indicating a considerable safety profile of T-Tre/BCN-Lipo-Ava cell *in vivo*.

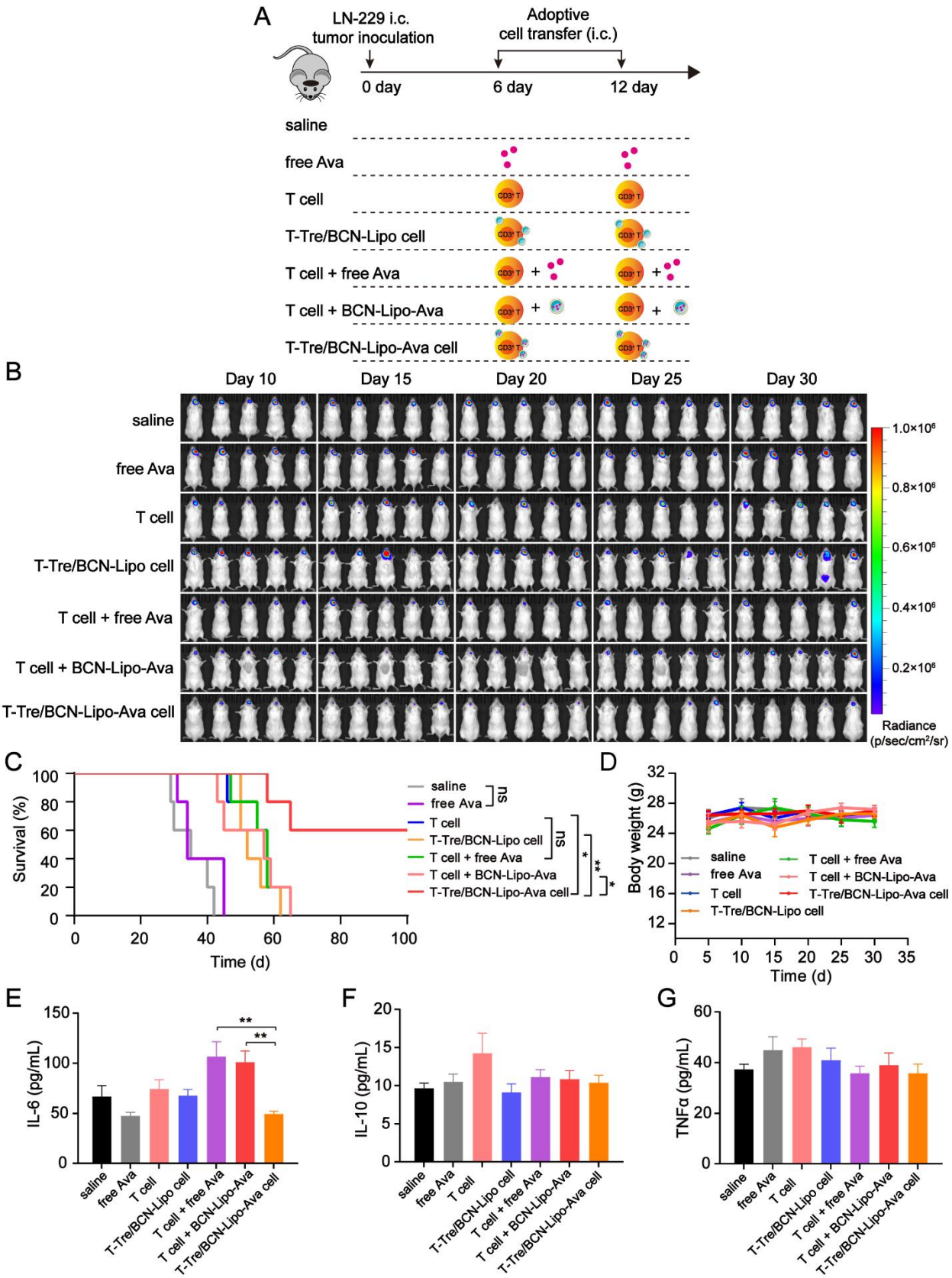
A
LN-229 i.c.
tumor inoculation
Adoptive
cell transfer (i.c.)
0 day
6 day
12 day
saline
free Ava
T cell
T-Tre/BCN-Lipo cell
T cell + free Ava
T cell + BCN-Lipo-Ava
T-Tre/BCN-Lipo-Ava cell
B
Day 10
Day 15
Day 20
Day 25
Day 30
saline
free Ava
T cell
T-Tre/BCN-Lipo cell
T cell + free Ava
T cell + BCN-Lipo-Ava
T-Tre/BCN-Lipo-Ava cell
1.0×10⁶
0.8×10⁶
0.6×10⁶
0.4×10⁶
0.2×10⁶
Radiance
(p/sec/cm²/sr)
C
Survival (%)
Time (d)
saline
free Ava
T cell
T-Tre/BCN-Lipo cell
T cell + free Ava
T cell + BCN-Lipo-Ava
T-Tre/BCN-Lipo-Ava cell
ns
ns
*
**
*
D
Body weight (g)
Time (d)
saline
free Ava
T cell
T-Tre/BCN-Lipo cell
T cell + free Ava
T cell + BCN-Lipo-Ava
T-Tre/BCN-Lipo-Ava cell
E
IL-6 (pg/mL)
**
**
F
IL-10 (pg/mL)
G
TNFα (pg/mL)

Fig. 7. Adoptive CAR T-Tre/BCN-Lipo-Ava cell transfer significantly inhibited the progression of glioblastoma in an orthotopic mouse model. (A) Schematic illustration of the experimental setting. i.c.: Intracranial injection. **(B)** *In vivo* bioluminescence images of mice bearing glioblastoma, n = 5 mice/group. **(C)** The survival profiles of mice receiving tested formulations, n = 5 mice/group. **(D)** Body weights of all mice, n = 5 mice/group. Serum IL-6 **(E)**, IL-10 **(F)**, and TNFα **(G)** levels measured by ELISA, n = 5 mice/group. Data were analyzed by unpaired t-test **(E)** or a log-rank (Mantel-Cox) test **(C)**. Error bars denote SEM, $*P < 0.05$, $**P < 0.01$, $***P < 0.001$ and ns means no significant difference.

Discussion

It is increasingly recognized that T cells undergo metabolic exhaustion in oxygen- and nutrient-limited tumor microenvironment, which may largely contribute to the failure of solid tumor by T-cell therapy (*11*). In an effort to boost solid tumor immunotherapy via metabolic interventions, according to the comprehensive review of Prof. Romero (*41*), there are three main prospects: i) pre-conditioning T cells with metabolic modulators during *in vitro* expansion for adoptive T cell therapy (*42-44*). However, the *in vitro* reprogrammed T-cell metabolism may be reversed within metabolic suppressive tumor microenvironment (*45*). ii) Systemic administration of free metabolic modulators. Nevertheless, this approach is limited due to the non-specific distribution as well as the poor pharmacokinetic profile of these compounds (*46, 47*). iii) Targeted delivery of metabolic modulators into tumor microenvironment using nanoparticles or oncolytic viruses. Yet delivering the compounds into cells of interest, such as T cells, is challenging (*48*). Drawing the strong points of each prospect and to offset one's own weakness, we provided a combination of metabolic interventions and T-cell therapy via cell-surface anchor-engineering (T-Tre/BCN-

Lipo-Ava cell) to boost solid tumor immunotherapy. T-Tre/BCN-Lipo-Ava cell yielded a sustained T-cell metabolic fitness within tumor microenvironment by a sustained and prolonged release of Ava. In addition, retaining Ava on T-cell surface afforded a pseudo-autocrine/paracrine action profile for Ava, which was critical for an optimized synergistic efficacy (*49*).

With respect to clinical translation, although T-Tre/BCN-Lipo-Ava cell demonstrated great potentials, the long-term toxicity should be thoroughly investigated and the metabolic-modulating drugs can be tailored to clinically approved ones. Besides, further investigation, including the improvement of the physical stability of liposomes by optimizing lipid compositions, will be necessary to increase the therapeutic window of combined drugs.

In conclusion, this rational and novel combination of metabolic intervention yielded optimized synergistic efficacy in mouse models of several solid tumors and provided an alternative combination strategy for boosting solid tumor immunotherapy. Additionally, general combinatorial technology based on cell-surface anchor-engineering, served as a proof-of-concept, which can be easily tailored to other combinations based on clinically approved metabolic drugs and/or antibodies. Lastly, this cell-surface anchor-engineering expanded the repertoire of non-genetic T-cell engineering and can be deployed to various cell types.

Materials and Methods

Cell lines and mice

The human glioblastoma cell line LN-229, the human prostatic carcinoma cell line PC-3 and the mouse melanoma cell line B16F10 were all purchased from the American Type Culture Collection. LN-229 cells were cultured in Dulbecco's modified Eagle's medium (DMEM) with 5%

FBS and 1% Penicillin-Streptomycin. PC-3 cells were cultured in Dulbecco's modified Eagle's medium-F12 (DMEM-F12) with 10% FBS and 1% Penicillin-Streptomycin. B16F10 cells were cultured in DMEM with 10% FBS and 1% Penicillin-Streptomycin. The B16F10 cells were stably transfected with the plasmid pAc-neo-OVA (B16F10-OVA) which carried chicken ovalbumin (OVA) mRNA. For bioluminescent *in vivo* tumor imaging, we transduced the B16F10-OVA and LN-229 cells with the firefly luciferase expressing lentivirus (Genechem, Shanghai, China). Human $CD3^+$ pan T cells were purchased from Miao Tong Biological Technology Co.Ltd (Shanghai, China). NOD/SCID/IL2R$\gamma^{-/-}$ (NSG, 18-20 g, male) mice and TCR transgenic OT-I mice (18-20 g, male) were purchased from GemPharmatech Co. Ltd (Nanjing, China). TCR transgenic Thy1.1$^+$ pmel-1 mice were purchased from Jackson Laboratory. C57BL/6J mice (18-20 g, male) were obtained from Beijing Vital River Laboratory Animal Technology Co. Ltd (Beijing, China). All the animals were pathogen free and allowed access to food and water freely. The Animal Care and Use Committee of the China Pharmaceutical University approved all of the animal studies and animal protocols.

Chemistry

In order to successfully modify cell surface by click reaction, a cyclononynyl-derivatized phospholipid analogue (DSPE-BCN) which based on a copper-catalyzed click reaction of tetrazinazine-alkyne ring addition was to design and synthesize in this chapter. As a lipid click module, the DSPE-BCN can be incorporated into the liposome surface and the structure was confirmed by ^{1}H-NMR and MS. On the other hand, a tetrazinyl-derivatized PEG phospholipid analogue (DSPE-PEG_{5k}-Tre) which have a click reactive group and can be inserted into the surface of the cell membrane was designed and synthesized. And two fluorescently labeled tetrazine derivatives (FITC-DSPE-PEG_{5k}-Tre and DSPE-PEG_{5k}-FITC) were designed and

synthesized. All above structures were confirmed by ^{1}H-NMR. Detailed synthesis method of each compound was listed in the supporting information. At the same time, UV spectroscopy was performed to detect the reaction between the two modules at 540 nm.

Isolation of mouse CD8^{+} T cells

Spleens from C57BL/6J Thy1.1^{+} pmel-1 mice or C57BL/6J OT-I mice were ground through a 70-μm filter, and red blood cells were removed by incubation with ACK lysis buffer for 5 min at 4°C. Then, the splenic cells were centrifuged, washed with D-PBS (without Ca^{2+} and Mg^{2+}), and isolated by EasySep^{TM} Mouse CD8^{+} T cell Isolation Kit (StemCell) to obtained naive pmel-1 Thy1.1^{+} CD8^{+} T cells (pmel-1 CD8^{+} T cells) or OT-I CD8^{+} T cells. For activated CD8^{+} T cells, naive CD8^{+} T cells were resuspended at 1.5 × 10^{6} cells per milliliter in RPMI medium containing 10 ng/mL recombinant mouse IL-2, plate-bound 5 μg/mL anti-CD3 and 2 μg/mL anti-CD28 agonist antibodies and incubated at 37°C. After an incubation period for 2 days, dead cells were removed by centrifugation, and living cells were collected. Activated CD8^{+} T cells were cultured in medium containing IL-2 and anti-CD3 and anti-CD28 agonist antibodies for *in vitro* and *in vivo* studies.

Preparation and characterization of T-Tre/BCN-Lipo-Ava Cell

T-Tre/BCN-Lipo-Ava cell was obtained by incubating CD8^{+} T cells sequentially with DSPE-PEG$_{5K}$-Tre and BCN-Lipo-Ava. Briefly, CD8^{+} T cells (1 × 10^{6} cells/mL) were resuspended in serum-free medium. Then, CD8^{+} T cells were incubated with 80 μg DSPE-PEG$_{5K}$-Tre at 37°C for 10 min. After two times of ice-cold PBS wash, cells were incubated with BCN-Lipo-Ava with the concentration of Ava at 100 μg/mL at 37°C for 30 min. The CD8^{+} T cells with surface-anchored BCN-Lipo-Ava were collected by centrifugation at 800 g for 5 min, washed with PBS and resuspended in medium for *in vitro* or *in vivo* studies. The concentration of Ava in T-

Tre/BCN-Lipo-Ava cell was determined using high performance liquid chromatography (HPLC-LC-2010A HT, SHIMADZU, Japan).

For the preparation of T cells anchored with fluorescent liposomes, $CD8^+$ T cells (1×10^6 cells/mL) were incubated with 80 μg FITC-DSPE-PEG_{5K}-Tre or FITC-DSPE-PEG_{5K} or DSPE-PEG_{5K}-Tre at 37°C for 10 min. After washing with PBS, BCN-Lipo-RhoB or RhoB-Lipo were incubated with cells at 37°C for 30 min. After washing with PBS, the $CD8^+$ T cells anchored with fluorescent anchoring module or fluorescent liposomes were stained with Hoechst 33342, fixed with 4% PFA and used immediately for the confocal imaging and flow cytometry analysis.

To further confirm our surface anchor-engineering strategy enabled the anchoring of nanoparticles on T-cell surface, the BCN-modified Au nanoparticles (BCN-Au) were obtained through BCN-PEG-SH reaction with Au nanoparticles. Then, the $CD8^+$ T cells were incubated with DSPE-PEG_{5K}-Tre for 10 min. After washing with PBS, BCN-Au were further incubated with cells at 37°C for 30 min. $CD8^+$ T cells with surface-anchored Au nanoparticles were collected by centrifugation at 800 g for 5 min. The cells were fixed with 2.5% glutaraldehyde aqueous solution overnight. After washing by PBS for three times, samples were dehydrated with gradient ethanol and imaged by scanning electron microscopy (Quanta 250, FEI).

To investigate the stability of liposomes on the surface of T cell, RhoB-labelled T-Tre/BCN-Lipo-Ava cells were cultured and expanded for another 2 days and 4 days. Then, the cells were collected, stained with Hoechst 33342 and fixed with 4% PFA for confocal imaging and flow cytometry analysis. Moreover, for further assay the drug stability of T-Tre/BCN-Lipo-Ava cell, the amount of Ava in the supernatant, intracellular and filtered compartments were determined using HPLC. The *in vitro* stability of T-Tre/BCN-Lipo-Ava cell was evaluated under different conditions, including the normal physiological condition (PBS, pH 7.4) and FBS.

Briefly, T-Tre/BCN-Lipo-Ava cells (1×10^6 cells per well) were seeded in 24-well plates, and then incubated with 1640 medium or 50% FBS in 1640 medium for different periods (0, 2, 4, 6, 8, 10, 12, 24, 48, 72 h). The amounts of Ava anchored on T-Tre/BCN-Lipo-Ava cell and released in the supernatant medium were determined using HPLC.

To calculate the number of liposomes anchored on the surface of T cells, 1×10^6 $CD8^+$ T cells were first incubated with 80 μg DSPE-PEG_{5k}-Tre or DSPE-PEG_{5k} at 37°C for 10 min. After washing with PBS twice, T cells were then incubated with the BCN-Lipo-Ava solution in 1 mL for 30 min. The concentration of BCN-Lipo-Ava in the solution was assessed by Nanoparticle Tracking Analyzer (Malvern NanoSight NS300). The liposome number anchored on the surface of $CD8^+$ T cells per million was calculated as follows: $(N_{\text{before DSPE-PEG-Tre}} - N_{\text{after DSPE-PEG-Tre}}) - (N_{\text{before DSPE-PEG}} - N_{\text{after DSPE-PEG}})/10^6$, where $N_{\text{before DSPE-PEG-Tre}}$ and $N_{\text{before DSPE-PEG}}$ are the counted numbers of liposomes in the solution before the incubation of BCN-Lipo-Ava with T cells, and $N_{\text{after DSPE-PEG-Tre}}$ and $N_{\text{after DSPE-PEG}}$ were the counted numbers of liposomes in the supernatant after the incubation of BCN-Lipo-Ava with T cells. The counts of $N_{\text{before DSPE-PEG}}$ minus $N_{\text{after DSPE-PEG}}$ were used to calculate nonspecific adsorption of liposomes on the surface of T cells.

Evaluation of physiological functions of T-Tre/BCN-Lipo-Ava cell

The physiological activities of T-Tre/BCN-Lipo-Ava cell were evaluated, including viability, apoptosis, proliferation, chemotaxis and activation. For the viability analysis, 1×10^6 T cells and T-Tre/BCN-Lipo-Ava cells were cultured in RPMI medium containing 10 ng/mL recombinant mouse IL-2, plate-bound 5 μg/mL anti-CD3 and 2 μg/mL anti-CD28 agonist antibodies. At day 0, 3, 6, 8, 10, the cells were collected for trypan blue staining, counting the numbers of cell under the microscope to calculate the survival rate of the cells. Meanwhile, 1×10^6 T cells were

incubated with RPMI medium without anti-CD3 and anti-CD28 antibodies as control. Survival rate (%) = number of unstained cells/total number of cells × 100%.

For the apoptosis analysis, 1×10^6 T cells and T-Tre/BCN-Lipo-Ava cells after 10-day stimulation were collected and suspended in 0.5 mL of 1× binding buffer and washed twice with ice-cold PBS. The Annexin V-FITC Apoptosis Detection Kit (Vazyme, China) was used according to the manufacturer's instructions for the apoptosis assay. The stained cells were analyzed by the Attune NxT flow cytometer (Thermo).

For the proliferation assay, T cells and T-Tre/BCN-Lipo-Ava cells were resuspended at 1×10^7/mL in pre-warmed serum-free RPMI. CFSE was added to the cells at a final concentration of 2 μM, which were incubated at 37°C for 15 min. CFSE staining was quenched by adding a 1:1 volume ratio of cold RPMI with 10% FBS and cells were spun down followed by two more washes in cold RPMI with FBS. Then the cells resuspended in RPMI medium containing IL-2, and anti-CD3/CD28 beads (Dynabeads™ Mouse T-Activator CD3/CD28) were added to the medium at a bead-to-cell ratio of 1:1. Two days after activation, T cells were mixed with counting beads, washed once with FACS buffer, then the cells were continued culturing in incubator. At day 3 and day 5 the cells were collected and washed with PBS before analysis by flow cytometry. Meanwhile, T cells and T-Tre/BCN-Lipo-Ava cells were cultured in RPMI medium containing 10 ng/mL recombinant mouse IL-2 in the culture plate pre-coated with 5 μg/mL anti-CD3 and 2 μg/mL anti-CD28 agonist antibodies. At day 0, 3, 6, 8, 10, the cells were collected and counted through the cell counter. Fold expansions rate (%) = number of cells / number of cells (day 0) × 100%.

Chemotactic migration across vascular endothelial cells. A transwell model with confluent endothelial (HUVEC) monolayer was established to investigate the transvascular capacity of

surface anchor-engineered T cells. Briefly, HUVECs (2×10^5 cells/well) were seeded onto the upper chamber of the transwell (3 μm, 24 mm) and cultured with the medium containing FBS (10% *v:v*). The integrity of the cell monolayer was evaluated by measuring the transepithelial electrical resistance (TEER) values using a Millicell-ERS voltohmmeter (Millipore). The cell monolayers with TEER value higher than 300 Ω cm^2 were used for the transmigration studies. T-Tre/BCN-Lipo-Ava cells were added to the upper chamber with incubation of 25 ng/mL TNFα for 4 h, and 20 ng/mL MCP-1 was added into the lower chamber to induce the migration. After 12 h of incubation, the supernatant in the upper chamber and the medium in the lower chamber were sampled, and the HUVEC cell layers on the membrane of the transwell were harvested. The amount of Ava in the supernatant, intracellular and filtered compartments were determined using HPLC. The Ava ratio in each compartment was calculated compared with the feeding amount of Ava. The number of T cells in the lower chamber was also counted.

The chemotaxis of T-Tre/BCN-Lipo-Ava cell was investigated using a transwell migration assay (Corning). Briefly, 1×10^6 T-Tre/BCN-Lipo-Ava cells or unmodified $CD8^+$ T cells were added to the upper chamber of the transwell, and different concentration of MCP-1 (5 ng/mL, 20 ng/mL, 100 ng/mL) was added into the lower chamber to induce the migration. After 12 h of incubation, the cells in the lower chamber were harvested and the numbers were counted using a haemacytometer. The chemotaxis index ($(N_{T\text{-}Tre/BCN\text{-}Lipo\text{-}Ava} - N_{control})/N_{control}$) was calculated, where $N_{T\text{-}Tre/BCN\text{-}Lipo\text{-}Ava}$ and $N_{control}$ are the counted numbers of $CD8^+$ T cells in the lower chamber after incubating with T-Tre/BCN-Lipo-Ava cell in the presence of MCP-1 and the unmodified $CD8^+$ T in the absence of MCP-1, respectively.

For verity the activated of T cell, naive unmodified or T-Tre/BCN-Lipo-Ava cells were plated on 96 well microtiter plates and stimulated with or without anti-CD3/CD28 agonist

antibody beads (Dynabeads™ Mouse T-Activator CD3/CD28). After 24 h incubation, the cells were collected and stained with FITC anti-mouse CD69 antibody (Biolegend), and the expression levels of the early T cell activation markers CD69 were quantified by flow cytometry.

The $CD8^+$ T cells were stimulated with concanavalin A (ConA, Sigma) in different concentrations for 2 days and rested for another 1 day. Then cells were anchored with BCN-Lipo-Ava or incubated with 1 μM free Ava for 24 h or 48 h. The cell supernatant was used to measure IL-2, TNFα and IFNγ productions of $CD8^+$ T cells through ELISA kit (Elabscience, China).

Measurement of $CD8^+$ T cells cytotoxicity.

To measure $CD8^+$ T-cell cytotoxicity, activated pmel-1 $CD8^+$ T cells, Ava pretreated pmel-1 $CD8^+$ T cells and pmel-1 $CD8^+$ T-Tre/BCN-Lipo-Ava cells were washed three times with PBS, then the three group of cells were mixed with B16F10 (1×10^5) in the medium (phenol-free RPMI 1640, 2% FBS) at the ratios of 10:1, respectively. After 4 h, 12 h and 24 h, the cytotoxic efficiency was measured by quantifying the release of endogenous lactate dehydrogenase (LDH) from B16F10 cells using LDH Cytotoxicity Assay Kit.

The effector function analysis of T-Tre/BCN-Lipo-Ava cell *in vitro*

Super-resolution stimulated emission depletion (STED) image. The bottom of the confocal chamber was treated with 0.01% *w/v* poly-L-lysine solution for 2 h, which was then discarded and placed at room temperature for 15 min to dry the solution. Next, 20 μg/mL anti-mouse CD3 antibody was added into the chamber and incubated overnight at 4°C. After the incubation, the bottom of the chamber was washed once with PBS. Meanwhile, 1×10^6 T-Tre/BCN-Lipo-Ava cells or 1×10^6 $CD8^+$ T cells were cultured for 12 h, and another group of 1×10^6 $CD8^+$ T cells were added to 1 μM free Ava for 12 h. The above three groups of cells were plated in the pre-

treated confocal chambers, incubated at 37°C for 10 min, and fixed with 4% PFA for 15 min at room temperature. After washing twice with PBS, $CD8^+$ T cells were incubated with Alexa Fluor® 647 anti-mouse TCR β chain antibody (Biolegend) for 20 min at room temperature and washed twice with PBS. Afterwards, the cells were incubated with 0.2% Triton X-100 for 10 min, washed with PBS, and blocked with non-specific binding protein for 30 min at room temperature with 2% BSA. Alexa Fluor® 488 anti-ZAP-70 Phospho (Tyr319)/Syk Phospho (Tyr352) antibody (Biolegend) were incubated for 1 h at room temperature. The expression of TCR and phosphorylated ZAP-70 on the membrane of $CD8^+$ T cells was imaged by STED microscopy (Leica TCS SP8). Super-resolution STED images were analyzed using Leica LAS X.

Western Blot. To detect that the effect of Ava on TCR signaling of $CD8^+$ T cells, $CD8^+$ T cells plus 1 μM free Ava (T cell + free Ava) and $CD8^+$ T cells engineered with Ava-loaded liposomes (T-Tre/BCN-Lipo-Ava cell) were incubated for 12 h, after stimulated with CD3/CD28 antibodies for different times (0, 15, 30 min), the cells were collected. The whole cell protein extracts were isolated using RIPA lysis buffer. Protein concentration was determined by BCA Protein Assay Kit (Keygen Biotech, China). Approximately 30 μg total protein was loaded, fractionated by SDS-PAGE, transferred to PVDF membrane, and probed with anti-β actin (Absin, Shanghai, China), anti-pCD3ζ (Tyr142) (Thermo), anti-CD3ζ (Bioworld, Nanjing, China), anti-pZAP70 (Tyr319) (Cell Signaling Technology), anti-ZAP70 (Bioworld, Nanjing, China), anti-pERK1/2 (Cell Signaling Technology) or anti-ERK1/2 (Cell Signaling Technology), respectively. Signal was detected using Chemiluminescence imaging system (Tanon, Shanghai, China). Band intensities on the western blots were quantified by densitometric analysis using ImageJ software (Fiji, 1.51n). The grey value of each protein band was calculated using the integrated density value (mean grey value × area).

Super-resolution imaging was performed on N-STORM microscope (Nikon). Three groups were set up for the imaging TCR distribution in the plasma membrane using STORM ($CD8^+$ T cells without Ava for 12 h, $CD8^+$ T cells incubated with 1 μM free Ava for 12 h and T-Tre/BCN-Lipo-Ava cells cultured for 12 h). T cells were placed in 35 mm confocal chamber and fixed with 4% PFA, followed by surface staining with 5 μg/mL anti-TCRα/β (Abcam) for 4 h at 4°C, then the cells were stained with 2 μg/mL Alexa 647-conjugated goat anti-hamster IgG (the secondary antibody) for 2 h at 4°C after washing with PBS ten times. Before imaging, the buffer in the dish was replaced with the imaging buffer contained 100 mM β-mercaptoethanolamin (MEA) for a sufficient blinking of fluorophores. We analysis molecule distribution of super-resolution STORM images with N-STORM analysis module of NIS Elements 5.0 (Nikon) based on Ripley's K-function. Ripley's K-function is used to compare a given distribution with a random distribution (*50, 51*). The equation is as follow: $K(r) = \frac{1}{n}\sum_{i=1}^{n} N_{p_i}(r)/\lambda$. Here, r represents cluster radius, λ means the number of points per area (region of interest), p_i is the *i*th point and the sum is taken over n points. The expected value of $K(r)$ for a random Poisson distribution is πr^2 and deviations from the expectation indicate scales of clustering. Then the K-function is linearly normalized to L-function so that the expected value is r: $L(r) = \sqrt{K(r)/\pi}$. The K-function can be normalized so that the expected value is 0, yielding the so-called H-function: $H(r)=L(r)-r$. $L(r)$ $-r$ represents the efficiency of molecule clustering while the r value at the maximum $L(r)$ $-r$ value represents the cluster size with the highest probability.

Imaging of TCR clustering by TIRFM. Planar lipid bilayers (PLBs) containing biotinylated lipids were prepared for imaging TCR clustering. Biotinylated liposomes were prepared by ultrasound treatment of 1,2-dioleoyl-sn-glycero-3-phosphocholine (DOPC) (A.V.T. Shanghai Pharmaceuticals Co, Ltd) and 1,2-dioleoyl-sn-glycero-3-phosphoethanolamine-cap-biotin

(biotin-DOPC) (Sigma) at a molar ratio of 25:1 in PBS at a total lipid concentration of 5 mM. PLBs were formed in confocal chambers and 0.1 mM biotinylated-containing PLB were washed with PBS for 20 min. After washing with PBS, PLBs were incubated with 20 nM streptavidin for 20 min, and residual streptavidin was removed by washing with PBS. Streptavidin-containing PLBs were incubated with 20 nM bionylated anti-mouse CD3 antibody (17A2) (Biolegend), and unconjugated antibody was removed by washing with PBS. Finally, PLBs were treated with PBS containing 5% FBS for 30 min at 37°C and washed thoroughly for TIRFM of T cells. Three groups were set up for the imaging of TCR clustering by TIRFM ($CD8^+$ T cells without Ava for 12 h, $CD8^+$ T cells incubated with 1 μM free Ava for 12 h and T-Tre/BCN-Lipo-Ava cells cultured for 12 h). Then the T cells were stained with anti-mTCRα/β (Abcam) and Alexa 647-conjugated goat anti-hamster IgG (the secondary antibody). TIRFM imaging was performed on Leica DMI8 microscope. Images were analyzed with ImageJ (Fiji, 1.51n).

Measurement of the cholesterol level of T cells. Two methods were used to measure the cholesterol level of T cells. For Filipin III staining, T-Tre/BCN-Lipo-Ava cells were cultured for 12 h and the supernatant was collected for further studies. Six groups were set up for the experiment: (1) naive $CD8^+$ T cells incubated with the CM from T-Tre/BCN-Lipo-Ava cells for 12 h; (2) activated $CD8^+$ T cells incubated with the CM from T-Tre/BCN-Lipo-Ava cells for 12 h; (3) naive $CD8^+$ T cells incubated with equivalent free Ava for 12 h; (4) activated $CD8^+$ T cells incubated with an equivalent dose of free Ava for 12 h; (5) naive $CD8^+$ T cells cultured with the CM from unanchored $CD8^+$ T cells for 12 h; (6) activated $CD8^+$ T cells cultured with the CM from unanchored $CD8^+$ T cells for 12 h. Cells of each group were collected, plated in confocal chamber after centrifugation, and fixed with a 4% paraformaldehyde (PFA) for 15 min at room temperature. Then cells were washed twice with PBS, and stained with 50 μg/mL Filipin III

(Sigma) for 30 min at 4°C. Images were collected using a Zeiss LSM880 confocal microscope and analyzed using a Zeiss ZEN software. For oxidation-based cholesterol quantification, the activated $CD8^+$ T cells were incubated with the CM of T-Tre/BCN-Lipo-Ava cells for 12 h. Meanwhile, activated $CD8^+$ T cells were incubated with an equivalent dose of free Ava for 12 h as positive control. The plasma membrane was collected through the methods as previously reported (*52*, *53*) and the cholesterol level was quantified using the Amplex Red cholesterol assay kit (Invitrogen) according to manufacturer's instructions.

***In vivo* therapy study by adoptive surface anchor-engineered T cells**

For pharmacodynamic evaluation of adoptive surface anchor-engineered pmel-1 $CD8^+$ T cell and OT-I $CD8^+$ T cell in orthotopic melanoma model, B16F10 cells (1.0×10^6) and B16F10-OVA cells (1.0×10^6) were injected intradermally in the flank of C57BL/6J mice on day 0.

The B16F10 bearing mice were lymphodepleted by 2 mg/kg cyclophosphamide and 2 mg/kg fludarabine on day 6. Then, the mice were randomly divided into nine groups (n = 6) and were respectively received saline, free Ava (2 mg/kg), BCN-Lipo-Ava (2 mg/kg for Ava), pmel-1 $CD8^+$ T cell (1.0×10^7), pmel-1 $CD8^+$ T cell plus free Ava (1.0×10^7, 2 mg/kg for Ava), pmel-1 $CD8^+$ T-Tre/BCN-Lipo cell (1.0×10^7), Ava pretreated pmel-1 $CD8^+$ T cell (1.0×10^7), pmel-1 $CD8^+$ T cell (1.0×10^7) plus unconjugated BCN-Lipo-Ava (2 mg/kg for Ava) or pmel-1 $CD8^+$ T-Tre/BCN-Lipo-Ava cell (1.0×10^7, 2 mg/kg for Ava) by intravenous injection at day 8 and day 14 after tumor inoculation. The tumor size was measured every two days, and the animal survival rate was recorded every day. Tumor size was calculated as (length × $width^2$)/2. The weight of tumor-bearing mice was recorded on day 3, 6, 9, 12, 15, 18 and 20, respectively. Mice with tumor size larger than 20 mm at the longest axis were euthanized for ethical consideration.

Heart, liver, spleen, lung, and kidney of the mice were collected and weighed to calculate the organ index.

On day 6, B16F10-OVA bearing mice with 50 mm^3 volumes tumors size were randomly divided into seven groups (n = 7). Mice were respectively received saline, free Ava (2 mg/kg), OT-I $CD8^+$ T cell (1.0×10^7), OT-I $CD8^+$ T cell plus free Ava (1.0×10^7, 2 mg/kg for Ava), OT-I $CD8^+$ T-Tre/BCN-Lipo cell (1.0×10^7), OT-I $CD8^+$ T cell (1.0×10^7) plus unconjugated BCN-Lipo-Ava (2 mg/kg for Ava) or OT-I $CD8^+$ T-Tre/BCN-Lipo-Ava cell (1.0×10^7, 2 mg/kg for Ava) by intravenous injection at day 6 and 12 after tumor inoculation. The tumor size was measured every two days, and the animal survival rate was recorded every day. Tumor size was calculated as (length × $width^2$)/2. The weight of tumor-bearing mice was recorded on day 3, 6, 8, 10, 12, 14, and 16, respectively. Mice with tumor size larger than 20 mm at the longest axis were euthanized for ethical consideration. Heart, liver, spleen, lung, and kidney of the mice were collected and weighed to calculate the organ index.

For pharmacodynamic evaluation of adoptive surface anchor-engineered T cell in pulmonary metastatic melanoma model, B16F10-OVA-Luci cells (2.0×10^5) were injected intravenously into C57BL/6J mice, and then mice were randomly divided into six groups (n = 5). Mice were respectively received saline, free Ava (2 mg/kg), OT-I $CD8^+$ T cell (1.0×10^7), OT-I $CD8^+$ T cell plus free Ava (1.0×10^7, 2 mg/kg for Ava), OT-I $CD8^+$ T cell (1.0×10^7) plus unconjugated BCN-Lipo-Ava (2 mg/kg for Ava) or OT-I $CD8^+$ T-Tre/BCN-Lipo-Ava cell (1.0×10^7, 2 mg/kg for Ava) by intravenous injection at day 6 and 12 after tumor inoculation. From day 6, mice were imaged for bioluminescence every five days to monitor the tumor growth and the animal survival rate was recorded every day. Mice were euthanized when the body weight loss

was >20% of the pre-dosing weight. Heart, liver, spleen, lung, and kidney of the mice were collected and weighed to calculate the organ index.

Furthermore, orthotopic melanoma and metastatic lung were dissected, embedded in paraffin, sectioned, and stained with haematoxylin and eosin (H&E) using routine methods. Briefly, samples were harvested and fixed overnight in 4% paraformaldehyde (dissolved in phosphate buffer solution, pH 7.4) (Sigma-Aldrich) at 4°C. Subsequently, the paraformaldehyde-fixed tissues were transferred to 70% ethanol, dehydrated, embedded in paraffin (Sigma-Aldrich), divided into sections (5 μm thickness) and stained with H&E. Sections were photographed using dotSlide virtual microscopy (Olympus). Morphometric evaluation was performed, and the geometric characteristics of the tumor tissues were assessed using ImageJ (Fiji, 1.51n). Immunohistochemistry of Ki-67 was performed on paraffin sections by using rabbit anti-mouse-Ki-67 (1:200, Cell Signaling Technology) and staining with the HRP-DAB SPlink Detection Kit (ZSGB-Bio). The Ki-67 staining was imaged by a Microscope BX53 (Olympus) and analyzed by ImageJ (Fiji, 1.51n) with the ImmunoRatio 1.0 c plugin.

Measurement of serum cytokine levels and liver enzymes for toxicity study.

Serum samples from treated mice as described above were collected at day 18 or day 20 after tumor inoculation and these were then analyzed for cytokine levels of IL-6, IL-10 and TNFα using the ELISA Kit (Elabscience, China and Multisciences, China). The quantities of alkaline phosphatase (ALP), alanine transaminase (ALT), aspartate transaminase (AST), blood urea nitrogen (BUN), and lactate dehydrogenase (LDH) were determined using the corresponding assay kit, respectively.

***In vivo* bioluminescence imaging**

Luciferase substrate D-luciferin (Yeasen, Shanghai, China) suspended in ddH_2O (15 mg/mL) was injected (150 mg/kg) intraperitoneally 10 min before imaging. Bioluminescence images were collected on the IVIS Spectrum Imaging System (PerkinElmer, Waltham, MA, USA). Living Image software (PerkinElmer) was used to acquire and quantify the bioluminescence imaging data sets.

Anti-tumor responses, exhaustion and proliferation of adoptive transferred cells in tumor

After injection the pmel-1 $CD8^+$ T-Tre/BCN-Lipo-Ava cells for 4 days, the orthotopic melanoma were first digested by collagenase IV (Sangon Biotech), and leukocytes were isolated by 40-70% Percoll (GE) gradient centrifugation.

To measure the effector function of adoptive transferred cells (pmel-1 $CD8^+$ T-Tre/BCN-Lipo-Ava cell), the isolated cells were first stimulated with 1 μM ionomycin (MedChemExpress) and 50 ng/mL phorbol 12-myristate 13-acetate (PMA) for 4 h in the presence of 5 μg/mL Brefeldin A (BFA), followed by staining with PE-Cy7 anti-mouse Thy1.1 (Thermo). Then the cells were randomly divided into three groups, and were respectively stained with allophycocyanin (APC) anti-mouse PD-1 (Thermo), APC anti-mouse TIGIT (Vstm3) (Biolegend) or APC anti-mouse CD366 (TIM-3) (Biolegend). Next, cells were fixed with 4% PFA and punched through 0.2% Triton-X100. After that, the cells were stained with FITC anti-mouse granzyme B (Biolegend), PE-Cy5.5 anti-mouse IFNγ (Biolegend) or phycoerythrin (PE) anti-mouse TNFα (Biolegend), respectively. In general, to gate the cytokine or granule-producing cells, T cells without stimulation or stained with isotype control antibody were used as negative controls by flow cytometry analysis.

Additional, the isolated cells were stained with PE-Cy7 anti-mouse Thy1.1 (CD90.1), then the cells were randomly divided into two groups, and were respectively stained with APC anti-

mouse PD-1 (CD279) and PE anti-mouse TIGIT (Vstm3) (Biolegend), or APC anti-mouse CD366 (TIM-3), PE anti-mouse-CD152 (CTLA-4) (Thermo) and FITC anti-mouse CD223 (LAG-3) (Thermo). The exhausted markers of cells were analyzed by flow cytometry.

Moreover, to measure the proliferation and the level of membrane cholesterol in tumor-infiltrating pmel-1 T-Tre/BCN-Lipo-Ava cell, the isolated cells were stained with PE-Cy7 anti-mouse Thy1.1 (CD90.1), PE anti-mouse Ki-67 (Biolegend) and Filipin III (Santa cruz), followed by analysis using flow cytometry.

Anti-tumor responses, exhaustion and proliferation of tumor-infiltrating CD8$^+$ T cells

After the injection of pmel-1 CD8$^+$ T-Tre/BCN-Lipo-Ava cell or OT-I CD8$^+$ T-Tre/BCN-Lipo-Ava cell for 4 days, the orthotopic melanoma and metastatic lungs were first digested by collagenase IV (Sangon Biotech), and leukocytes were isolated by 40-70% Percoll (GE) gradient centrifugation.

To measure the effector function of tumor-infiltrating CD8$^+$ T cells, the isolated cells were first stimulated with 1 μM ionomycin (MedChemExpress) and 50 ng/mL phorbol 12-myristate 13-acetate (PMA) for 4 h in the presence of 5 μg/mL Brefeldin A (BFA), and then stained with APC-Cy7 anti-mouse CD8α (BD PharmingenTM). Next, cells were fixed with 4% PFA and punched through 0.2% Triton-X100. Then the cells were stained with FITC anti-mouse granzyme B (Biolegend), APC anti-mouse IFNγ (Biolegend) or PE anti-mouse TNFα (Biolegend), respectively. In general, to gate the cytokine or granule-producing cells, T cells without stimulation or stained with isotype control antibody were used as negative controls.

Moreover, the isolated cells were stained with APC-Cy7 anti-mouse CD8α (CD90.1), then the cells were randomly divided into two groups, and were respectively stained with APC anti-mouse PD-1 (CD279) and PE anti-mouse TIGIT (Vstm3) antibody, or APC anti-mouse CD366

(TIM-3), PE anti-mouse-CD152 (CTLA-4) and FITC anti-mouse CD223 (LAG-3). Next, the exhausted markers of cell were analyzed by flow cytometry.

Additional, to measure the proliferation and the level of membrane cholesterol in tumor-infiltrating $CD8^+$ T cell, the isolated cells were stained with APC-Cy7 anti-mouse CD8α, PE anti-mouse Ki-67 (Biolegend) and Filipin III (Santa cruz), followed by analysis using flow cytometry.

Preparation of CAR-T cells for ACT

The huGD2.CD28.4-1BB.z chimeric antigen receptor was designed based on the heavy and light chains of GD2 14G.2a antibody to form a single-chain variable fragment, which was fused to a portion of the extracellular and transmembrane domains of human CD8α, followed by the intracellular domains of CD28, 4-1BB and CD3ζ. The plasmid coding huGD2.CD28.4-1BB.z-CAR-GFP was constructed, and lentivirus was packaged by Public Protein/Plasmid Library (PPL, Nanjing, China). Human $CD3^+$ pan T cells were stimulated with CD3/CD28 agonist antibodies (Life Technologies). T cells were cultured in ImmunoCultTM-XF T cell Expansion Medium (Stemcell), penicillin and streptomycin (1%) and IL-2 (20 IU/ml) at 37°C, 5% CO_2, for 1 day. T cells were transfected with CAR-expressing lentivirus by a spinoculation method. In brief, a non-Tissue-Culture treated plate was coated with 10 μg/mL fibronectin at 37°C for 4 h or at 4°C overnight. Extra fibronectin was removed, and 2×10^5 T cells were added and transfected with 10^7 IU lentivirus in 1mL immunoCult XF T-cell medium containing 8 μg/mL polybrene and 10 ng/mL recombinant mouse IL-2 at 37°C, 5% CO_2. The plate was spun at 1500 g for 60 minutes at 22°C~32°C for three times with 8-h interval. Transfection reagent was replaced with 3 mL of fresh T-cell medium, and the expression of the CAR was confirmed and quantified by flow

cytometry. CAR-T cells were cultured and expanded in the single-use cell bag in a 3D-shaking bioreactor (25-250 mL SS04-1, Sunscell Biotech LTD, China) for 10 days.

Preparation and characterization of CAR T-Tre/BCN-Lipo-Ava cell

CAR T-Tre/BCN-Lipo-Ava cell was obtained by incubating CAR-T cells with DSPE-PEG_{5K}-Tre and BCN-Lipo-Ava sequentially. The method was the same to the preparation of T-Tre/BCN-Lipo-Ava cell. For characterization of CAR-T cells anchored with liposomes, CAR-T cells (1×10^6 cells/mL) were incubated with or without DSPE-PEG_{5K}-Tre at 37°C for 10 min. After washing with PBS, BCN-Lipo-RhoB were incubated with cells at 37°C for 30 min. After washing with PBS, cells anchored with fluorescent liposomes were obtained for DNA staining using Hoechst 33342. Then the cells were fixed with 4% PFA for confocal imaging and flow cytometry analysis.

TCR clustering of CAR T-Tre/BCN-Lipo-Ava cell

The bottom of the confocal chamber was treated with 0.01% *w/v* poly-L-lysine solution for 2 h, which was then discarded and placed at room temperature for 15 min to dry the solution. Meanwhile, 1×10^6 CAR T-Tre/BCN-Lipo-Ava cells or 1×10^6 CAR-T cells were cultured for 12 h, and another group of 1×10^6 CAR-T cells were incubated with 1 μM free Ava for 12 h. After that, the three groups of cells were plated in poly-L-lysine pre-treated confocal chamber. Then, cells were stained with anti-TCRα antibody (ab18861, Abcam) and Alexa 647-conjugated goat anti-rabbit IgG (the secondary antibody). Finally, cells were stained with Hoechst 33342 and fixed with 4% PFA for confocal imaging.

***In vivo* antitumor effect of CAR T-Tre/BCN-Lipo-Ava cell**

For the generation of intracranial glioma model, human luciferase-expressing glioblastoma cells (LN-229-luci cells) were detached by trypsinization, washed, and resuspended in PBS at a

concentration of 5×10^5 cells in 5 μL. NSG mice were anesthetized by isoflurane and fixed in a stereotactic frame. 5×10^5 cells were injected into the right frontal lobe of NSG mice using a microsyringe as previously described (*54*). The injection coordinates for the orthotopic model was 2 mm lateral from the bregma and 1.5 mm deep from the outer border of the cranium, respectively. Mice were randomly divided into five groups (n = 5). Mice were respectively received saline, free Ava (1 mg/kg), CAR-T cell (5×10^6), CAR-T cell plus free Ava (5×10^6, 1 mg/kg for Ava), CAR T-Tre/BCN-Lipo cell (5×10^6), CAR-T cell (5×10^6) plus unconjugated BCN-Lipo-Ava (1 mg/kg for Ava) or CAR T-Tre/BCN-Lipo-Ava cell (5×10^6, 1 mg/kg for Ava) by intracranial injection at day 6 and 12. From day 6, mice were imaged for bioluminescence every five days to monitor the tumor growth, and survival of mice was recorded every day. The body weight of mice was recorded on day 5, 10, 15, 20, 25, 30, respectively. Mice were euthanized when the body weight loss was >20% of the pre-dosing weight. Serum samples from each group of mice were collected at day 18 after tumor inoculation and these were then analyzed for cytokine levels of IL-6, IL-10 and TNFα using the ELISA Kit (Elabscience, China).

Statistical analysis

Statistical analyses were performed using GraphPad Prism 8.0. All plots show mean ± SEM. One-way ANOVA test was used for comparisons of multiple groups, Student's unpaired t test was used for two-group comparisons in the appropriate conditions, and a log-rank (Mantel-Cox) test was used to analyze the statistical significance of difference for survival analysis. Statistical significance was set at $*P < 0.05$, $**P < 0.01$ and $***P < 0.001$, ns: no significant difference.

Supplementary Materials

Fig. S1. Synthesis and characterization of DSPE-PEG_{5k}-Tre and DSPE-BCN.

Fig. S28. Biosafety analysis of surface anchor-engineered OT-I T cell in B16F10-OVA pulmonary metastatic melanoma.

Fig. S29. IFNγ, TNFα and GzmB production of tumor-infiltrating $CD8^+$ T cell after a single adoptive OT-I T-Tre/BCN-Lipo-Ava cell transfer in B16F10-OVA pulmonary metastatic melanoma.

Fig. S30. Characteristics of LN-229 glioblastoma cells.

Fig. S31. Characteristics of anti-GD2 CAR-T cells.

Fig. S32. Surface-anchoring of CAR-T cells by liposomal Ava enhanced TCR clustering and immunological synapse formation.

Table S1. The number of liposomes anchored on the surface of T cell.

References and Notes

1. A. L. Garfall, M. V. Maus, W. T. Hwang, S. F. Lacey, Y. D. Mahnke, J. J. Melenhorst, Z. Zheng, D. T. Vogl, A. D. Cohen, B. M. Weiss, K. Dengel, N. D. Kerr, A. Bagg, B. L. Levine, C. H. June, E. A. Stadtmauer, Chimeric Antigen Receptor T Cells against CD19 for Multiple Myeloma. *N Engl J Med* **373**, 1040-1047 (2015).
2. S. A. Grupp, M. Kalos, D. Barrett, R. Aplenc, D. L. Porter, S. R. Rheingold, D. T. Teachey, A. Chew, B. Hauck, J. F. Wright, M. C. Milone, B. L. Levine, C. H. June, Chimeric antigen receptor-modified T cells for acute lymphoid leukemia. *N Engl J Med* **368**, 1509-1518 (2013).
3. E. K. Moon, L. C. Wang, D. V. Dolfi, C. B. Wilson, R. Ranganathan, J. Sun, V. Kapoor, J. Scholler, E. Pure, M. C. Milone, C. H. June, J. L. Riley, E. J. Wherry, S. M. Albelda, Multifactorial T-cell Hypofunction That Is Reversible Can Limit the Efficacy of

Chimeric Antigen Receptor-Transduced Human T cells in Solid Tumors. *Clin Cancer Res* **20**, 4262-4273 (2014).

4. A. Ribas, J. D. Wolchok, Cancer immunotherapy using checkpoint blockade. *Science* **359**, 1350-1355 (2018).
5. J. Tang, L. Pearce, J. O'Donnell-Tormey, V. M. Hubbard-Lucey, Trends in the global immuno-oncology landscape. *Nat Rev Drug Discov* **17**, 783-784 (2018).
6. J. Tang, A. Shalabi, V. M. Hubbard-Lucey, Comprehensive analysis of the clinical immuno-oncology landscape. *Ann Oncol* **29**, 84-91 (2018).
7. J. Li, W. Li, K. Huang, Y. Zhang, G. Kupfer, Q. Zhao, Chimeric antigen receptor T cell (CAR-T) immunotherapy for solid tumors: lessons learned and strategies for moving forward. *J Hematol Oncol* **11**, 22 (2018).
8. T. Gargett, W. B. Yu, G. Dotti, E. S. Yvon, S. N. Christo, J. D. Hayball, I. D. Lewis, M. K. Brenner, M. P. Brown, GD2-specific CAR T Cells Undergo Potent Activation and Deletion Following Antigen Encounter but can be Protected From Activation-induced Cell Death by PD-1 Blockade. *Mol Ther* **24**, 1135-1149 (2016).
9. G. Varricchi, M. R. Galdiero, V. Mercurio, D. Bonaduce, G. Marone, C. G. Tocchetti, Pharmacovigilating cardiotoxicity of immune checkpoint inhibitors. *Lancet Oncol* **19**, 1545-1546 (2018).
10. P. F. Wang, Y. Chen, S. Y. Song, T. J. Wang, W. J. Ji, S. W. Li, N. Liu, C. X. Yan, Immune-Related Adverse Events Associated with Anti-PD-1/PD-L1 Treatment for Malignancies: A Meta-Analysis. *Front Pharmacol* **8**, 730 (2017).

11. K. Renner, K. Singer, G. E. Koehl, E. K. Geissler, K. Peter, P. J. Siska, M. Kreutz, Metabolic Hallmarks of Tumor and Immune Cells in the Tumor Microenvironment. *Front Immunol* **8**, 248 (2017).

12. C. H. Chang, E. L. Pearce, Emerging concepts of T cell metabolism as a target of immunotherapy. *Nat Immunol* **17**, 364-368 (2016).

13. E. Molnar, M. Swamy, M. Holzer, K. Beck-Garcia, R. Worch, C. Thiele, G. Guigas, K. Boye, I. F. Luescher, P. Schwille, R. Schubert, W. W. Schamel, Cholesterol and sphingomyelin drive ligand-independent T-cell antigen receptor nanoclustering. *J Biol Chem* **287**, 42664-42674 (2012).

14. W. W. Schamel, I. Arechaga, R. M. Risueno, H. M. van Santen, P. Cabezas, C. Risco, J. M. Valpuesta, B. Alarcon, Coexistence of multivalent and monovalent TCRs explains high sensitivity and wide range of response. *J Exp Med* **202**, 493-503 (2005).

15. T. Zech, C. S. Ejsing, K. Gaus, B. de Wet, A. Shevchenko, K. Simons, T. Harder, Accumulation of raft lipids in T-cell plasma membrane domains engaged in TCR signalling. *EMBO J* **28**, 466-476 (2009).

16. W. Yang, Y. Bai, Y. Xiong, J. Zhang, S. Chen, X. Zheng, X. Meng, L. Li, J. Wang, C. Xu, C. Yan, L. Wang, C. C. Chang, T. Y. Chang, T. Zhang, P. Zhou, B. L. Song, W. Liu, S. C. Sun, X. Liu, B. L. Li, C. Xu, Potentiating the antitumour response of CD8(+) T cells by modulating cholesterol metabolism. *Nature* **531**, 651-655 (2016).

17. I. A. Khawar, J. H. Kim, H. J. Kuh, Improving drug delivery to solid tumors: priming the tumor microenvironment. *J Control Release* **201**, 78-89 (2015).

18. M. C. Milone, V. G. Bhoj, The Pharmacology of T Cell Therapies. *Mol Ther-Meth Clin D* **8**, 210-221 (2018).

19. M. Norelli, M. Casucci, C. Bonini, A. Bondanza, Clinical pharmacology of CAR-T cells: Linking cellular pharmacodynamics to pharmacokinetics and antitumor effects. *Biochim Biophys Acta* **1865**, 90-100 (2016).

20. G. Llaverias, J. C. Laguna, M. Alegret, Pharmacology of the ACAT inhibitor avasimibe (CI-1011). *Cardiovasc Drug Rev* **21**, 33-50 (2003).

21. B. Heemskerk, K. Liu, M. E. Dudley, L. A. Johnson, A. Kaiser, S. Downey, Z. Zheng, T. E. Shelton, K. Matsuda, P. F. Robbins, R. A. Morgan, S. A. Rosenberg, Adoptive cell therapy for patients with melanoma, using tumor-infiltrating lymphocytes genetically engineered to secrete interleukin-2. *Hum Gene Ther* **19**, 496-510 (2008).

22. K. Adachi, Y. Kano, T. Nagai, N. Okuyama, Y. Sakoda, K. Tamada, IL-7 and CCL19 expression in CAR-T cells improves immune cell infiltration and CAR-T cell survival in the tumor. *Nat Biotechnol* **36**, 346-351 (2018).

23. S. Rafiq, O. O. Yeku, H. J. Jackson, T. J. Purdon, D. G. van Leeuwen, D. J. Drakes, M. Song, M. M. Miele, Z. Li, P. Wang, S. Yan, J. Xiang, X. Ma, V. E. Seshan, R. C. Hendrickson, C. Liu, R. J. Brentjens, Targeted delivery of a PD-1-blocking scFv by CAR-T cells enhances anti-tumor efficacy in vivo. *Nat Biotechnol* **36**, 847-856 (2018).

24. C. Zhang, J. Liu, J. F. Zhong, X. Zhang, Engineering CAR-T cells. *Biomark Res* **5**, 22 (2017).

25. M. C. Milone, U. O'Doherty, Clinical use of lentiviral vectors. *Leukemia* **32**, 1529-1541 (2018).

26. H. Pan, P. Li, G. F. Li, W. J. Li, B. Hu, H. M. He, Z. Chen, F. F. Wang, L. L. Liu, Y. F. Gong, Y. T. Han, Y. M. Luo, M. B. Zheng, Y. F. Ma, L. T. Cai, Y. Jin, Glycometabolic

Bioorthogonal Chemistry-Guided Viral Transduction for Robust Human T Cell Engineering. *Adv Funct Mater* **29**, 22 (2019).

27. M. T. Stephan, J. J. Moon, S. H. Um, A. Bershteyn, D. J. Irvine, Therapeutic cell engineering with surface-conjugated synthetic nanoparticles. *Nat Med* **16**, 1035-1041 (2010).

28. L. Tang, Y. R. Zheng, M. B. Melo, L. Mabardi, A. P. Castano, Y. Q. Xie, N. Li, S. B. Kudchodkar, H. C. Wong, E. K. Jeng, M. V. Maus, D. J. Irvine, Enhancing T cell therapy through TCR-signaling-responsive nanoparticle drug delivery. *Nat Biotechnol* **36**, 707-716 (2018).

29. M. T. Stephan, S. B. Stephan, P. Bak, J. Z. Chen, D. J. Irvine, Synapse-directed delivery of immunomodulators using T-cell-conjugated nanoparticles. *Biomaterials* **33**, 5776-5787 (2012).

30. B. N. Huang, W. D. Abraham, Y. R. Zheng, S. C. B. Lopez, S. S. Luo, D. J. Irvine, Active targeting of chemotherapy to disseminated tumors using nanoparticle-carrying T cells. *Sci Transl Med* **7**, 291ra94 (2015).

31. W. Li, H. Pan, H. He, X. Meng, Q. Ren, P. Gong, X. Jiang, Z. Liang, L. Liu, M. Zheng, X. Shao, Y. Ma, L. Cai, Bio-Orthogonal T Cell Targeting Strategy for Robustly Enhancing Cytotoxicity against Tumor Cells. *Small* **15**, e1804383 (2019).

32. J. Xue, Z. Zhao, L. Zhang, L. Xue, S. Shen, Y. Wen, Z. Wei, L. Wang, L. Kong, H. Sun, Q. Ping, R. Mo, C. Zhang, Neutrophil-mediated anticancer drug delivery for suppression of postoperative malignant glioma recurrence. *Nat Nanotechnol* **12**, 692-700 (2017).

33. L. Dupre, R. Houmadi, C. Tang, J. Rey-Barroso, T Lymphocyte Migration: An Action Movie Starring the Actin and Associated Actors. *Front Immunol* **6**, 586 (2015).

34. M. Santamaria, M. Marubayashi, J. M. Arizon, A. Montero, M. Concha, F. Valles, A. Lopez, F. Lopez, J. Pena, The activation antigen CD69 is selectively expressed on CD8+ endomyocardium infiltrating T lymphocytes in human rejecting heart allografts. *Hum Immunol* **33**, 1-4 (1992).

35. S. F. Ziegler, F. Ramsdell, M. R. Alderson, The Activation Antigen Cd69. *Stem Cells* **12**, 456-465 (1994).

36. C. Castellanos Mdel, S. Lopez-Giral, M. Lopez-Cabrera, M. O. de Landazuri, Multiple cis-acting elements regulate the expression of the early T cell activation antigen CD69. *Eur J Immunol* **32**, 3108-3117 (2002).

37. J. Fan, R. T. Lin, S. Y. Xia, D. Chen, S. E. Elf, S. P. Liu, Y. Z. Pan, H. D. Xu, Z. Y. Qian, M. Wang, C. L. Shan, L. Zhou, Q. Y. Lei, Y. C. Li, H. Mao, B. H. Lee, J. Sudderth, R. J. DeBerardinis, G. J. Zhang, T. Owonikoko, M. Gaddh, M. L. Arellano, H. J. Khoury, F. R. Khuri, S. M. Kang, P. W. Doetsch, S. Lonial, T. J. Boggon, W. J. Curran, J. Chen, Tetrameric Acetyl-CoA Acetyltransferase 1 Is Important for Tumor Growth. *Mol Cell* **64**, 859-874 (2016).

38. N. E. Scharping, A. V. Menk, R. S. Moreci, R. D. Whetstone, R. E. Dadey, S. C. Watkins, R. L. Ferris, G. M. Delgoffe, The Tumor Microenvironment Represses T Cell Mitochondrial Biogenesis to Drive Intratumoral T Cell Metabolic Insufficiency and Dysfunction. *Immunity* **45**, 374-388 (2016).

39. W. W. Overwijk, A. Tsung, K. R. Irvine, M. R. Parkhurst, T. J. Goletz, K. Tsung, M. W. Carroll, C. L. Liu, B. Moss, S. A. Rosenberg, N. P. Restifo, gp100/pmel 17 is a murine tumor rejection antigen: Induction of "self"-reactive, tumoricidal T cells using high-affinity, altered peptide ligand. *J Exp Med* **188**, 277-286 (1998).

40. A. Heczey, D. Liu, G. Tian, A. N. Courtney, J. Wei, E. Marinova, X. Gao, L. Guo, E. Yvon, J. Hicks, H. Liu, G. Dotti, L. S. Metelitsa, Invariant NKT cells with chimeric antigen receptor provide a novel platform for safe and effective cancer immunotherapy. *Blood* **124**, 2824-2833 (2014).

41. L. Zhang, P. Romero, Metabolic Control of CD8(+) T Cell Fate Decisions and Antitumor Immunity. *Trends Mol Med* **24**, 30-48 (2018).

42. J. G. Crompton, M. Sukumar, R. Roychoudhuri, D. Clever, A. Gros, R. L. Eil, E. Tran, K. Hanada, Z. Yu, D. C. Palmer, S. P. Kerkar, R. D. Michalek, T. Upham, A. Leonardi, N. Acquavella, E. Wang, F. M. Marincola, L. Gattinoni, P. Muranski, M. S. Sundrud, C. A. Klebanoff, S. A. Rosenberg, D. T. Fearon, N. P. Restifo, Akt inhibition enhances expansion of potent tumor-specific lymphocytes with memory cell characteristics. *Cancer Res* **75**, 296-305 (2015).

43. L. Gattinoni, C. A. Klebanoff, D. C. Palmer, C. Wrzesinski, K. Kerstann, Z. Yu, S. E. Finkelstein, M. R. Theoret, S. A. Rosenberg, N. P. Restifo, Acquisition of full effector function in vitro paradoxically impairs the in vivo antitumor efficacy of adoptively transferred CD8+ T cells. *J Clin Invest* **115**, 1616-1626 (2005).

44. D. O'Sullivan, E. L. Pearce, Targeting T cell metabolism for therapy. *Trends Immunol* **36**, 71-80 (2015).

45. C. M. Alvey, K. R. Spinler, J. Irianto, C. R. Pfeifer, B. Hayes, Y. Xia, S. Cho, P. Dingal, J. Hsu, L. Smith, M. Tewari, D. E. Discher, SIRPA-Inhibited, Marrow-Derived Macrophages Engorge, Accumulate, and Differentiate in Antibody-Targeted Regression of Solid Tumors. *Curr Biol* **27**, 2065-2077 (2017).

46. J. A. Hubbell, A. Chilkoti, Chemistry. Nanomaterials for drug delivery. *Science* **337**, 303-305 (2012).

47. R. A. Petros, J. M. DeSimone, Strategies in the design of nanoparticles for therapeutic applications. *Nature Reviews Drug Discovery* **9**, 615-627 (2010).

48. E. Blanco, H. Shen, M. Ferrari, Principles of nanoparticle design for overcoming biological barriers to drug delivery. *Nat Biotechnol* **33**, 941-951 (2015).

49. G. A. Wiseman, J. L. Murray, P. Pieslor, A. Molina, L. I. Gordon, I. Gaston, C. Emmanouilides, P. Multani, T. E. Witzig, C. A. White, Impact of metabolic and pharmacokinetic variability on dosing methodology for radioimmunotherapy (RIT) in patients with CD20+B-cell non-Hodgkin's lymphoma (NHL). *J Nucl Med* **44**, 415p-415p (2003).

50. S. T. Hess, T. J. Gould, M. V. Gudheti, S. A. Maas, K. D. Mills, J. Zimmerberg, Dynamic clustered distribution of hemagglutinin resolved at 40 nm in living cell membranes discriminates between raft theories. *Proc Natl Acad Sci U S A* **104**, 17370-17375 (2007).

51. S. T. Hess, M. Kumar, A. Verma, J. Farrington, A. Kenworthy, J. Zimmerberg, Quantitative electron microscopy and fluorescence spectroscopy of the membrane distribution of influenza hemagglutinin. *J Cell Biol* **169**, 965-976 (2005).

52. Y. Han, H. Pan, W. Li, Z. Chen, A. Ma, T. Yin, R. Liang, F. Chen, Y. Ma, Y. Jin, M. Zheng, B. Li, L. Cai, T Cell Membrane Mimicking Nanoparticles with Bioorthogonal Targeting and Immune Recognition for Enhanced Photothermal Therapy. *Adv Sci (Weinh)* **6**, 1900251 (2019).

53. C. M. Hu, R. H. Fang, K. C. Wang, B. T. Luk, S. Thamphiwatana, D. Dehaini, P. Nguyen, P. Angsantikul, C. H. Wen, A. V. Kroll, C. Carpenter, M. Ramesh, V. Qu, S. H. Patel, J.

Zhu, W. Shi, F. M. Hofman, T. C. Chen, W. Gao, K. Zhang, S. Chien, L. Zhang, Nanoparticle biointerfacing by platelet membrane cloaking. *Nature* **526**, 118-121 (2015).

54. C. E. Brown, B. Aguilar, R. Starr, X. Yang, W. C. Chang, L. Weng, B. Chang, A. Sarkissian, A. Brito, J. F. Sanchez, J. R. Ostberg, M. D'Apuzzo, B. Badie, M. E. Barish, S. J. Forman, Optimization of IL13Ralpha2-Targeted Chimeric Antigen Receptor T Cells for Improved Anti-tumor Efficacy against Glioblastoma. *Mol Ther* **26**, 31-44 (2018).

Acknowledgments: We thank the Public Platform of the State Key Laboratory of Natural Medicines for assistance with the pathological-section imaging and flow cytometry, and we are grateful to Yumeng Shen and Ping Zhou for their help in performing fluorescence-activated cell sorting experiments. **Funding**: This work was supported by the National Natural Science Foundation of China (81930099, 81773664, 81473153, 81903651), "Double First-Class" University project (CPU2018GY47, CPU2018GF10), China Postdoctoral Science Foundation funded project (2017M611956), Natural Science Foundation of Jiangsu Province (BK20190558, BK20180565), 111 Project from the Ministry of Education of China and the State Administration of Foreign Expert Affairs of China (No. 111-2-07, B17047), and the Open Project of State Key Laboratory of Natural Medicines (No. SKLNMZZ202017). **Author contributions**: M.X.H. designed and conducted all experiments, analyzed the data and wrote the manuscript. S.Y.H. designed and conducted all cell and animal experiments, analyzed the data and wrote the manuscript. W.S.L. analyzed the data and wrote the manuscript. K.M.L. assisted *in vivo* pharmacodynamic experiments and western blot analysis. L.J.X. assisted in data analysis. Q.F.H. and L.L.Z. assisted in the genetic identification and breeding of C57BL/6J pmel-1 mice and C57BL/6J OT-I mice. Y.C. assisted in the synthesis of DSPE-BCN. H.B.S. supervised the metabolic experiments. C.Y.J. supervised all animal experiments and wrote the manuscript. C.Z.

conceived the project and supervised all experiments. **Competing interests**: The authors declare no competing interests. **Data and materials availability**: All data associated with this study are present in the paper or Supplementary Materials.

Supplementary Materials

Combination of Metabolic Intervention and T Cell Therapy via Cell-Surface Anchor-Engineering Augments Solid Tumor Immunotherapy

Authors: Meixi Hao†, Siyuan Hou†, Weishuo Li, Kaiming Li, Lingjing Xue, Qifan Hu, Lulu Zhu, Yue Chen, Hongbin Sun, Caoyun Ju*, Can Zhang*

Affiliations:

State Key Laboratory of Natural Medicines, Jiangsu Key Laboratory of Drug Discovery for Metabolic Diseases, Center of Advanced Pharmaceuticals and Biomaterials, China Pharmaceutical University, Nanjing 210009, P.R. China.

* Corresponding author. Email: zhangcan@cpu.edu.cn (C.Z.); jucaoyun@cpu.edu.cn (J.C.Y.)

† These authors contributed equally to this work.

Figure List

Table List

Supporting Methods

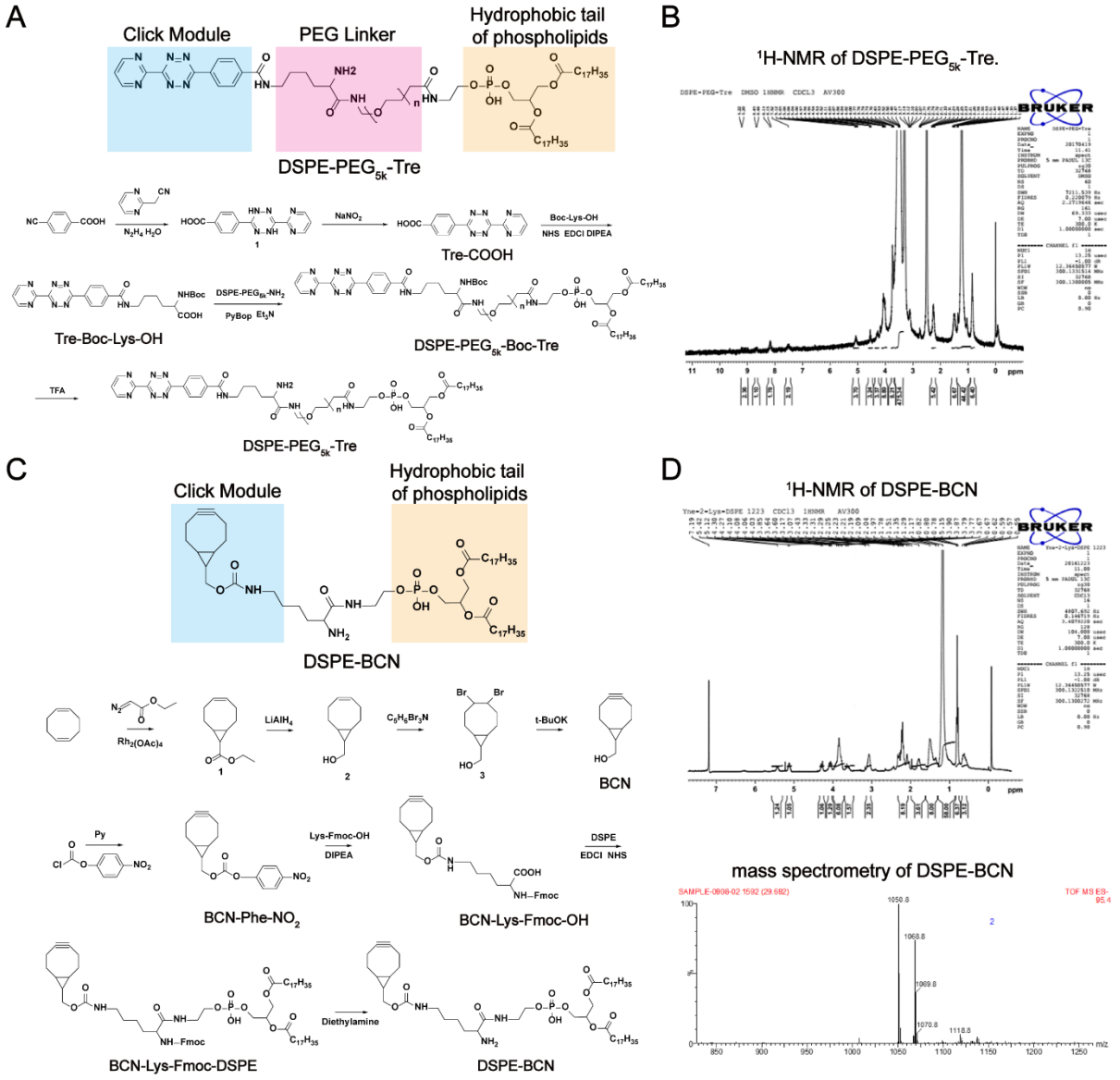

Fig. S1. Synthesis and characterization of DSPE-PEG$_{5k}$-Tre and DSPE-BCN. (A) The structure and synthesis of cell membrane anchoring module (DSPE-PEG$_{5k}$-Tre). **(B)** The characterization of DSPE-PEG$_{5k}$-Tre by ^{1}H-NMR. **(C)** The structure and synthesis of lipid click module (DSPE-BCN). **(D)** The characterization of DSPE-BCN by ^{1}H-NMR and mass spectrometry.

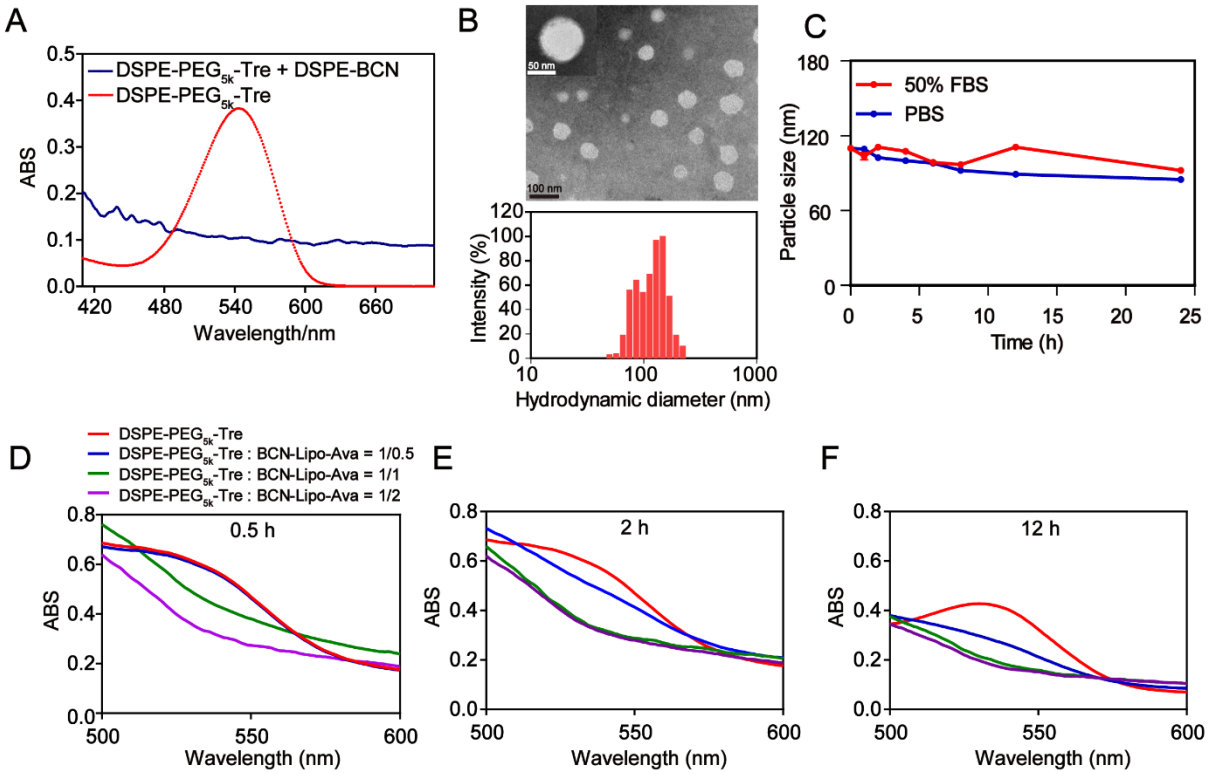

Fig. S2. Characteristics of the click reaction and the liposomal avasimibe (BCN-Lipo-Ava). **(A)** The UV spectral profile of DSPE-PEG$_{5k}$-Tre after incubation with or without DSPE-BCN for 10 min (n = 3 independent samples per group). **(B)** Representative transmission electron microscopy image and hydrodynamic sizes of BCN-Lipo-Ava. Scale bar, 100 nm. **(C)** The hydrodynamic size of BCN-Lipo-Ava measured by dynamic light scattering after incubation at PBS and 50% FBS in different time. n = 3 independent samples per group. **(D-F)** UV spectral profiles of the different mixtures of DSPE-PEG$_{5k}$-Tre and BCN-Lipo-Ava for 0.5 h, 2 h and 12 h (n = 3 independent samples per group). Error bars denote SEM.

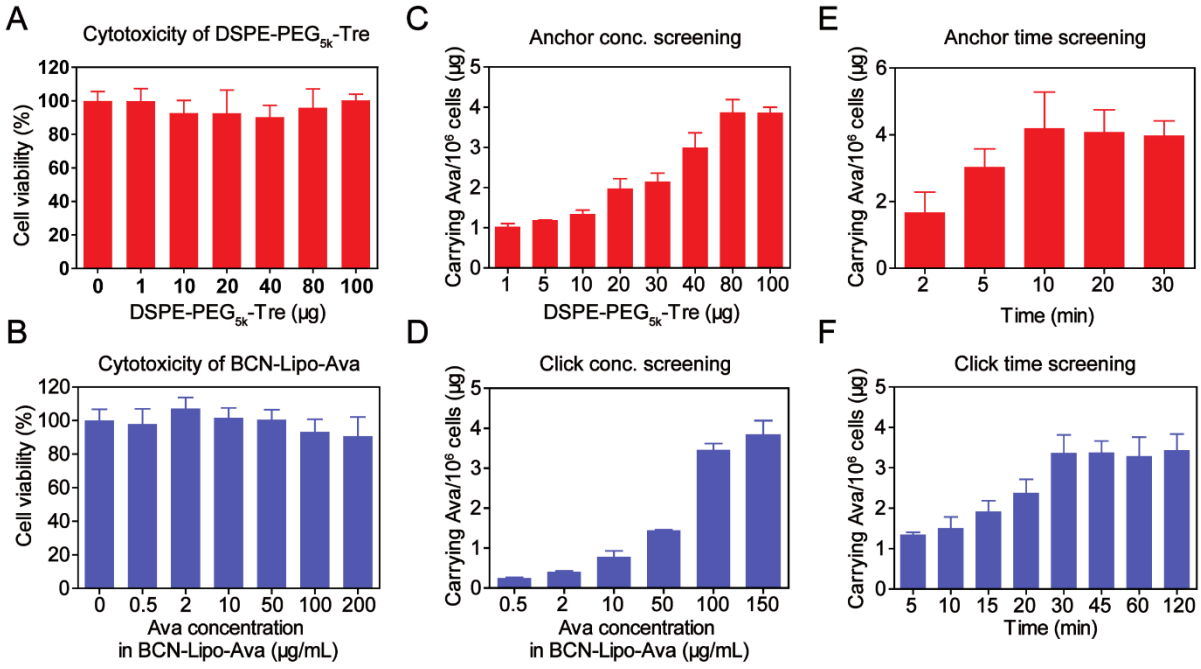

Fig. S3. *In vitro* cytotoxicity and the optimization of anchoring and clicking concentration and time. (A) *In vitro* cytotoxicity of different concentrations of DSPE-PEG$_{5k}$-Tre on T cells for 24 h (n = 5 independent samples per group). **(B)** *In vitro* cytotoxicity of different concentration of BCN-Lipo-Ava on T cells for 24 h (n = 5 independent samples per group). **(C)** The optimization of T cell surface-anchoring efficiency of Ava at different concentration of cell membrane anchoring module (DSPE-PEG$_{5k}$-Tre) when the concentration of BCN-Lipo-Ava set as 100 μg/mL (n = 5 independent samples per group). **(D)** The optimization of T cell surface-anchoring efficiency of Ava at different concentration of BCN-Lipo-Ava when the concentration of DSPE-PEG$_{5k}$-Tre set as 80 μg in 1 mL medium (n = 5 independent samples per group). **(E)** The optimization of T cell surface-anchoring efficiency of Ava at different incubation time with 80 μg DSPE-PEG$_{5k}$-Tre (n = 5 independent samples per group). **(F)** The optimization of T cell surface-anchoring efficiency of Ava at different incubation time with 100 μg/mL BCN-Lipo-Ava (n = 5 independent samples per group). All data were representative of two independent experiments, and were presented as the mean ± SEM.

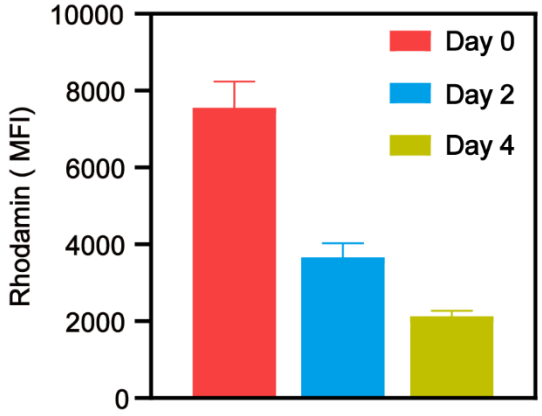

Percentage of initial anchoring liposomes over time		
Day 0	Day 2	Day 4
100% ± 15.6%	48.5% ± 8.3%	28.2% ± 3.3%

Fig. S4. Percentage of anchoring liposomes on T cells over time. Flow cytometry quantification the percentage of initial anchoring liposomes on T-Tre/BCN-Lipo-Ava cells expansion at 37°C for 0 days, 2 days and 4 days (n = 3 independent samples per group, data were presented as the mean ± SEM).

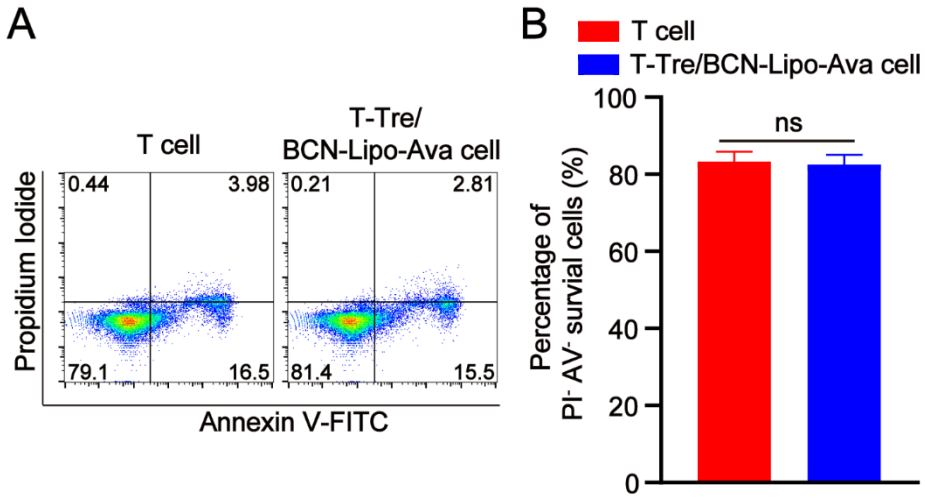

Fig. S5. Surface anchor-engineered T cell maintained normal T-cell vitality. Flow bound anti-CD3 and anti-CD28 antibody in the presence of IL-2, n = 6 independent samples per group. Data were analyzed by unpaired t-test. Error bars denote SEM, ns means no significant difference.

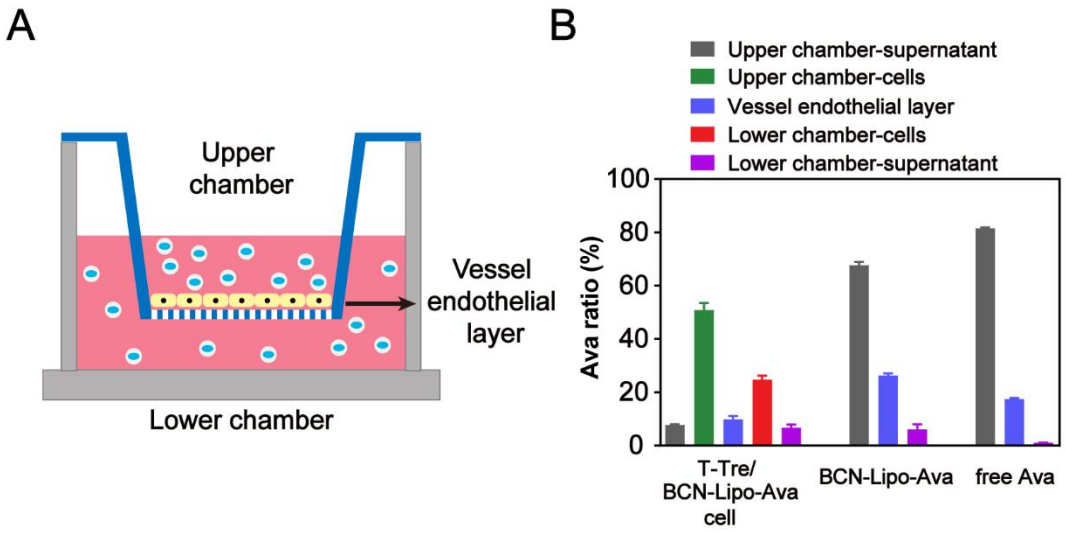

Fig. S6. The transvascular capacity of surface anchor-engineered T cell (T-Tre/BCN-Lipo-Ava cell). (A) The diagram of transwell insert for migration assay. **(B)** Quantification of the Ava distribution in the transwell chamber after incubation with different Ava formulations in the presence of MCP-1 (20 ng/mL) for 12 h, n = 3 independent samples per group. Data were presented as the mean ± SEM.

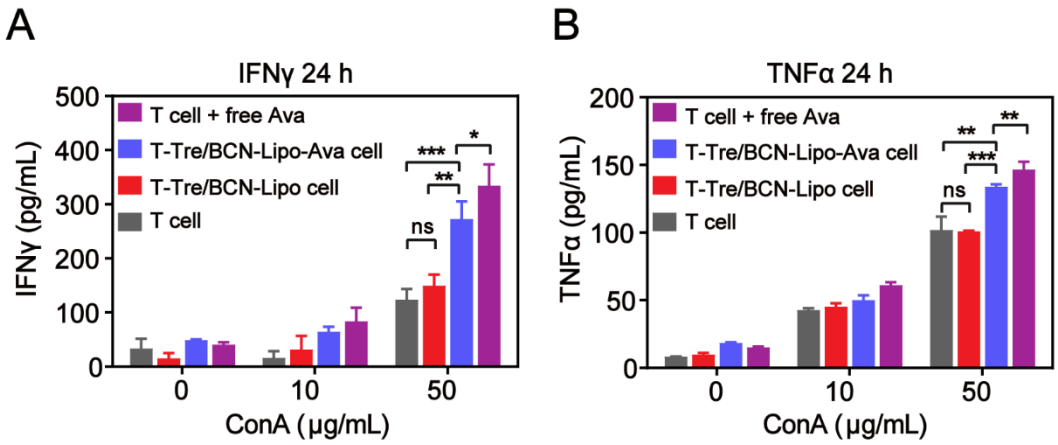

Fig. S7. *In vitro* activation of surface anchor-engineered T cell. ELISA analysis of cytokines (IFNγ and TNFα) secreted by T-Tre/BCN-Lipo-Ava cell after stimulation by concanavalin A (Con A) in different concentrations, n = 3 independent samples per group. Data were analyzed by unpaired t-test. Error bars denote SEM, *$P < 0.05$, **$P < 0.01$, ***$P < 0.001$ and ns means no significant difference.

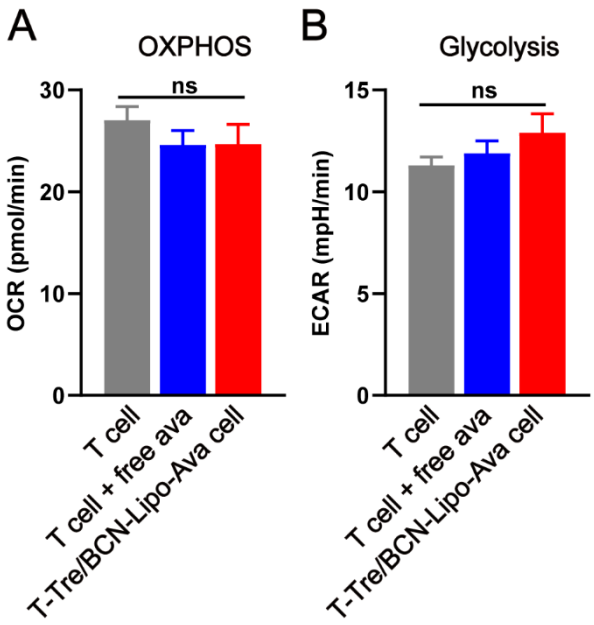

Fig. S8. The basal energy metabolism of surface anchor-engineered T cell (n = 3 independent samples per group). Data were representative of two independent experiments, and were analyzed by one-way ANOVA test. Error bars denote SEM, ns means no significant difference.

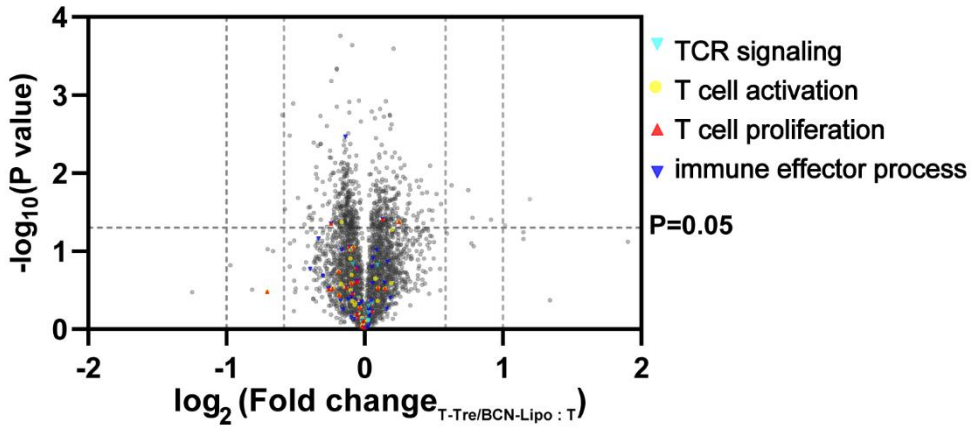

Fig. S9. Tandem Mass Tag (TMT)-based quantitative proteomics of surface anchor-engineered T cell (T-Tre/BCN-Lipo cell). T-Tre/BCN-Lipo cells were cultured *in vitro* at 37°C for 12 h, and the quantitative changes of the cellular proteome were investigated by Tandem Mass Tags (TMT) based mass spectrometry (n = 3 unique spectra). Volcano plot representing the distribution of all proteins (n = 7226) with relative protein abundance (log_2 fold change of T-Tre/BCN-Lipo : T) plotted against its significance level (negative log_{10} P value). The proteins enriched in the biological process of TCR signaling (light blue triangle), T cell activation (yellow dot), T cell proliferation (red triangle), and immune effector process (dark blue triangle) are shown.

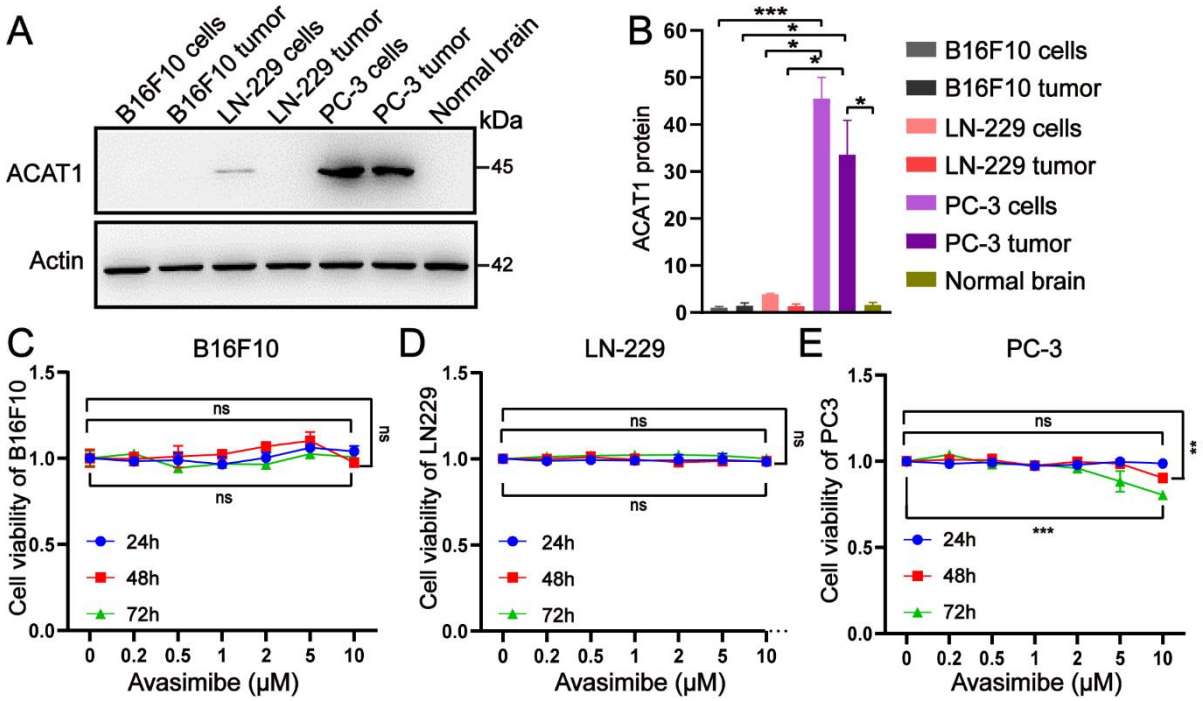

Fig. S10. The expression of ACAT1 proteins and the cytotoxicity of Ava in different types of cancer cells. (A) Expression of ACAT1 protein levels in different cancer cell lines and tumors. B16F10 melanoma was established by intradermal injection of B16F10 cells in C57BL/6J mice. PC-3 prostate cancer was established by subcutaneous injection of PC-3 cells in athymic nude mice. LN-229 glioblastoma was established by intracranial injection of LN-229 cells in NSG mice (n = 3 independent experiments). **(B)** The quantification of **(A). (C-E)** The cytotoxicity of avasimibe to different cancer cell lines, n = 3 independent samples per group. Data were analyzed by unpaired t-test. $*P < 0.05$, $**P < 0.01$, $***P < 0.001$, Error bars denote SEM.

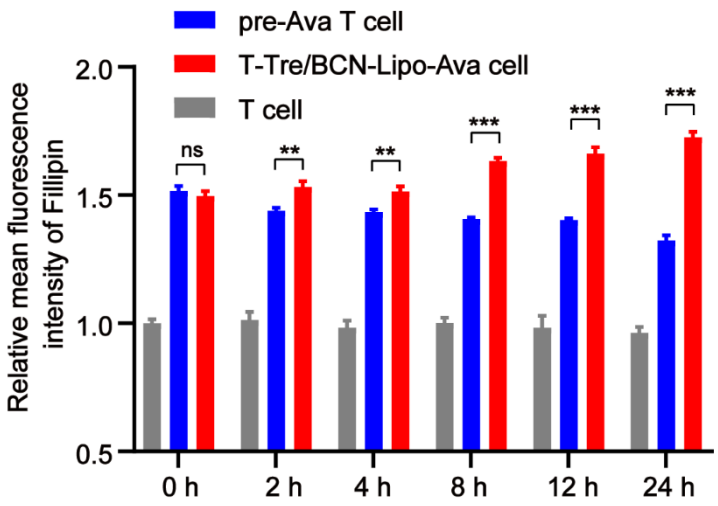

Fig. S11. Plasma membrane cholesterol level of T-Tre/BCN-Lipo-Ava cell over time. Flow cytometry quantification of Filipin III level in $CD8^+$ T cell membrane (n = 3 independent samples per group, data were analyzed by unpaired t-test. Error bars denote SEM, $^{**}P < 0.01$, $^{***}P < 0.001$, ns means no significant difference).

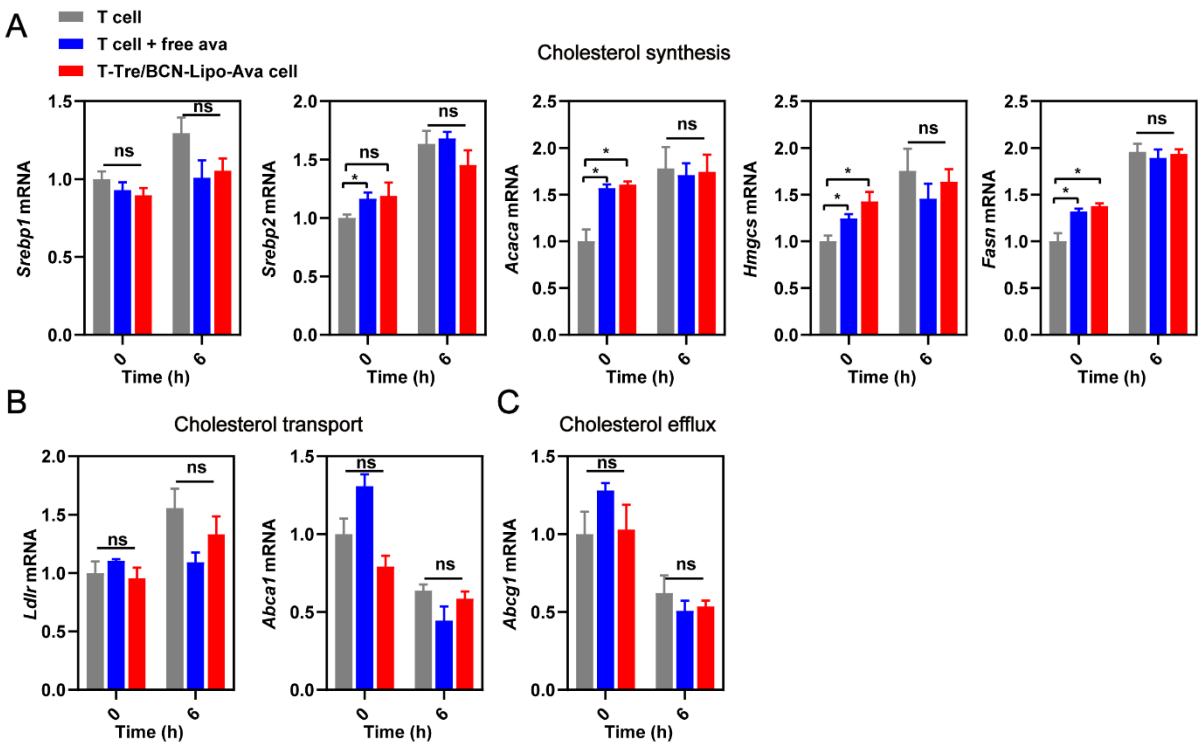

Fig. S12. Transcription levels of cholesterol metabolic genes in surface anchor-engineered T cell. (A) T-Tre/BCN-Lipo-Ava resulted in modest enhancement of the transcription levels of cholesterol synthesis genes, n = 3 independent samples per group. **(B-C)** Surface anchor-engineered T cell does not affect cholesterol transport and efflux genes in $CD8^+$ T cells, n = 3 independent samples per group. Data were analyzed by one-way ANOVA test. Error bars denote SEM, $*P < 0.05$ and ns means no significant difference.

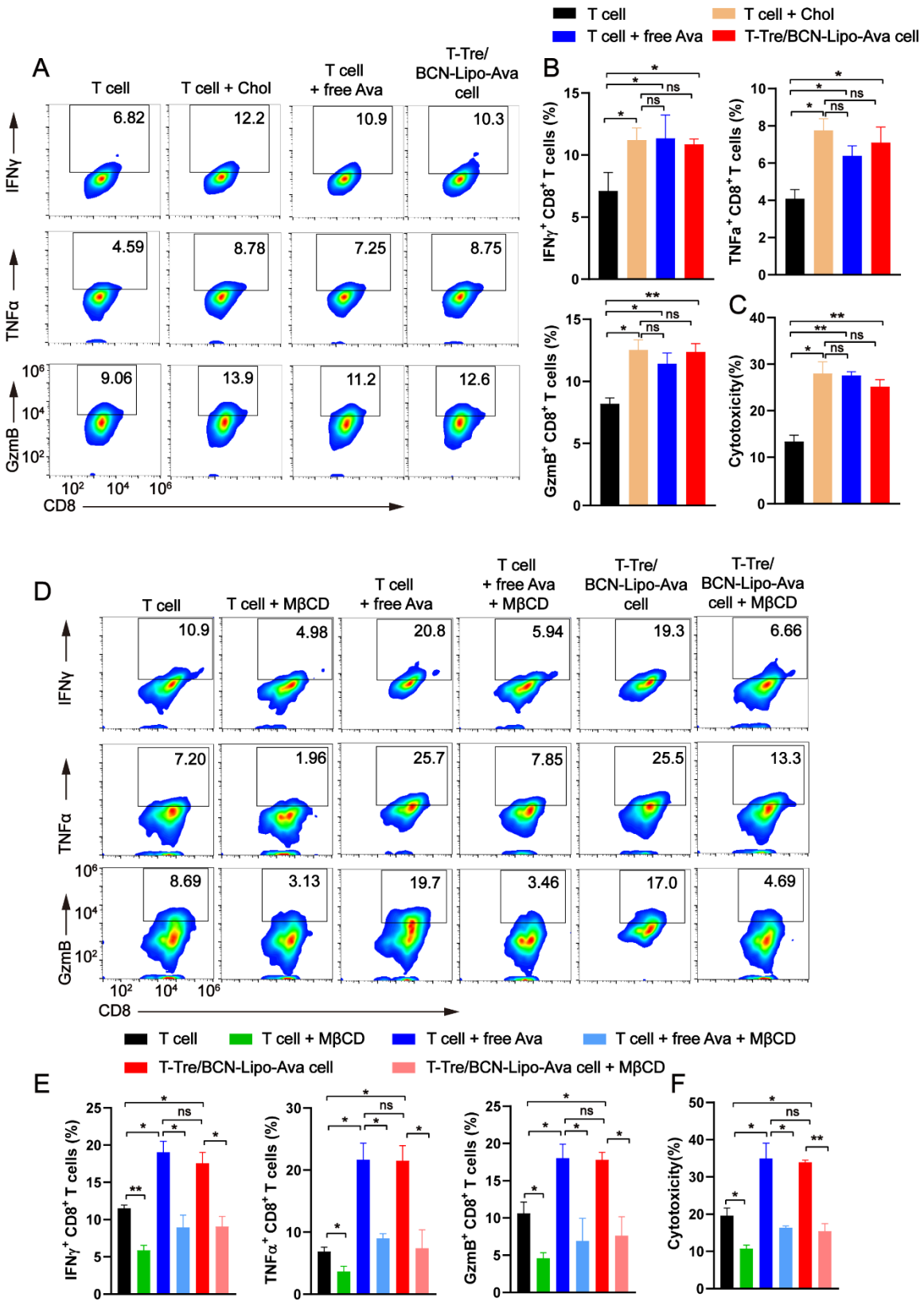

Fig. S13. IFNγ, TNFα and GzmB production and cytotoxicity of CD8⁺ T cell with adding

or depleting cholesterol. $CD8^+$ T cells were incubated at 37℃ for 12 h. To increase the cholesterol level, the cells were treated with MβCD-coated cholesterol (Chol). To reduce the cholesterol level of the plasma membrane, the cells were treated with MβCD. **(A)** Flow cytometry analysis and quantification of IFNγ, TNFα and GzmB secreted by $CD8^+$ T cell after treatment with MβCD-coated cholesterol (Chol) and stimulation with 5 μg/mL plate-bound anti-CD3 and anti-CD28 antibodies for 24 h at 37°C, n = 3 independent samples per group. **(B)** The quantification of **(A)**. **(C)** Cytotoxicity of $CD8^+$ T cells treated with MβCD-coated cholesterol (Chol), n = 3 independent samples per group. **(D)** Flow cytometry analysis and quantification of IFNγ, TNFα and GzmB secreted by $CD8^+$ T cell after treatment with MβCD and stimulation with 5 μg/mL plate-bound anti-CD3 and anti-CD28 antibodies for 24 h at 37°C, n = 3 independent samples per group. **(E)** The quantification of **(D)**. **(F)** Cytotoxicity of $CD8^+$ T cells treated with MβCD, n = 3 independent samples per group. Data were analyzed by unpaired t-test. Error bars denote SEM, $*P < 0.05$, $**P < 0.01$ and ns means no significant difference.

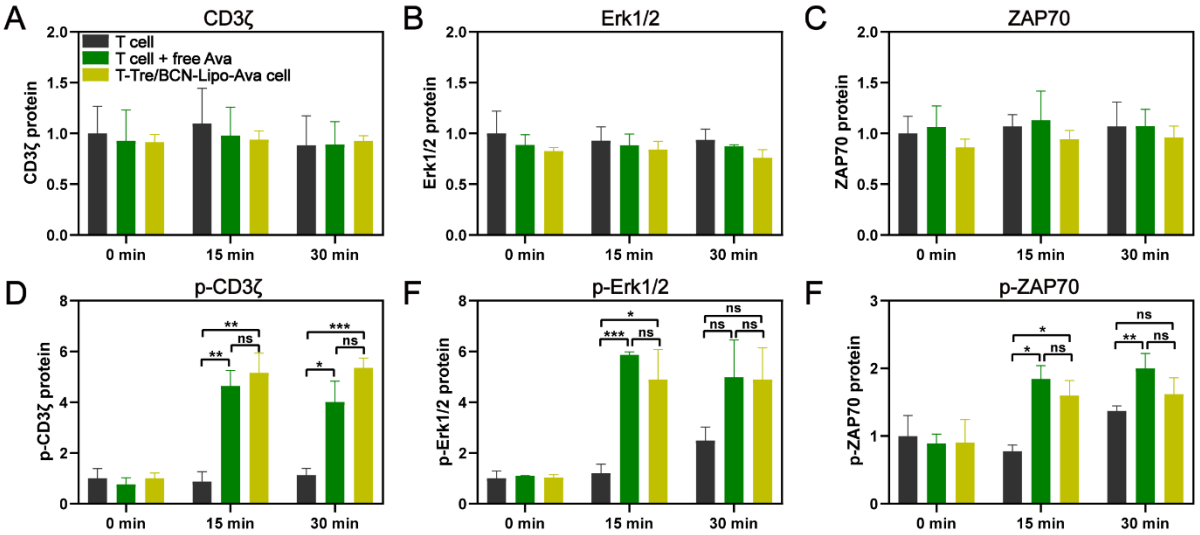

Fig. S14. Immunoblotting quantification of proximal and downstream TCR signaling molecules after stimulation with anti-CD3/CD28 Abs. Data were representative of three independent experiments, and were analyzed by unpaired t-test. Error bars denote SEM, *$P <$ 0.05, **$P < 0.01$, ***$P < 0.001$ and ns means no significant difference.

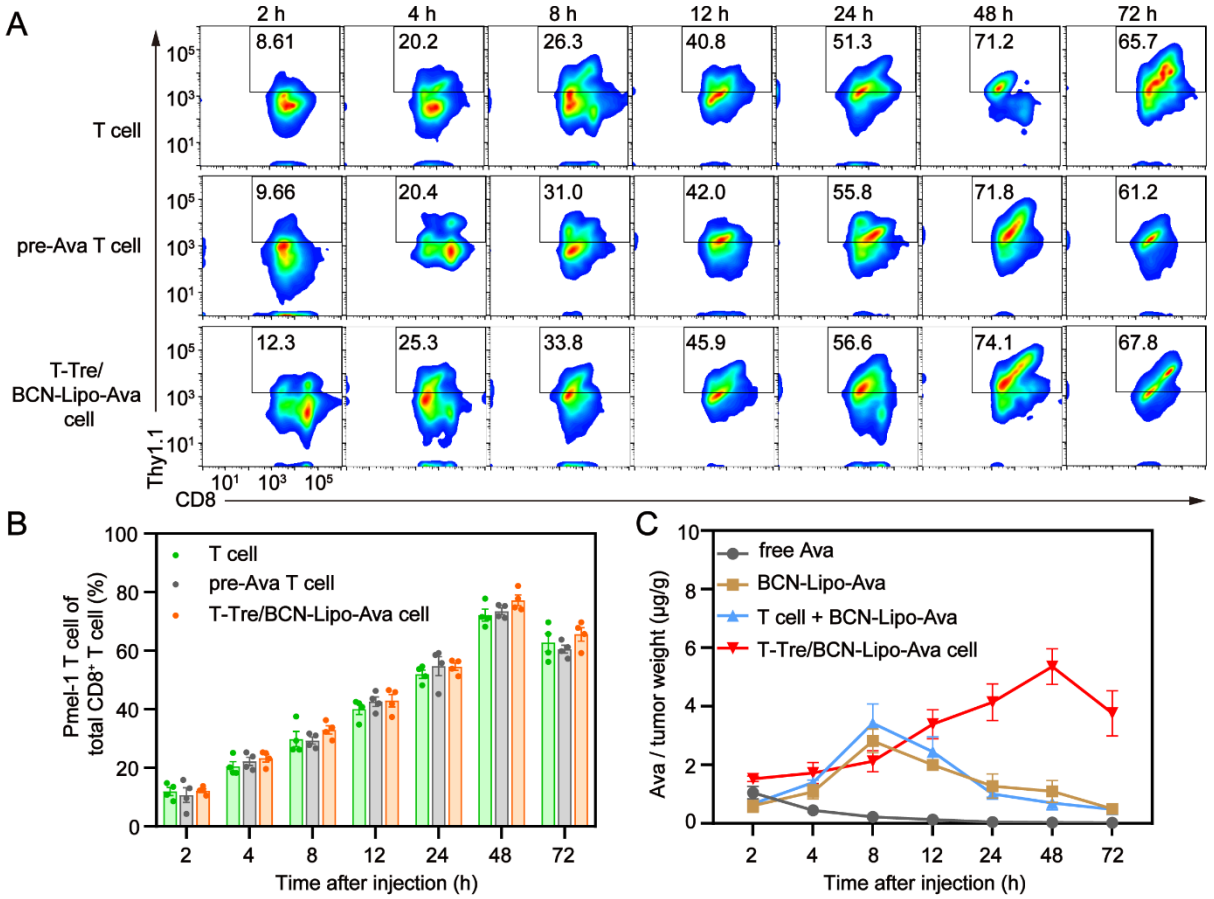

Fig. S15. The population of pmel-1 CD8$^+$ T cell and accumulation of Ava in tumor after injection of pmel-1 T-Tre/BCN-Lipo-Ava cell over time. (A-B) The population of pmel-1 T cell analyzed by flow cytometry analysis within tumor-infiltrating CD8$^+$ T cell, n = 4 mice/group. **(C)** HPLC quantification of the accumulation of Ava in tumor after intravenous injection of different Ava formulations with the dosage of Ava at 2 mg/kg, n = 3 mice/group. Error bars denote SEM.

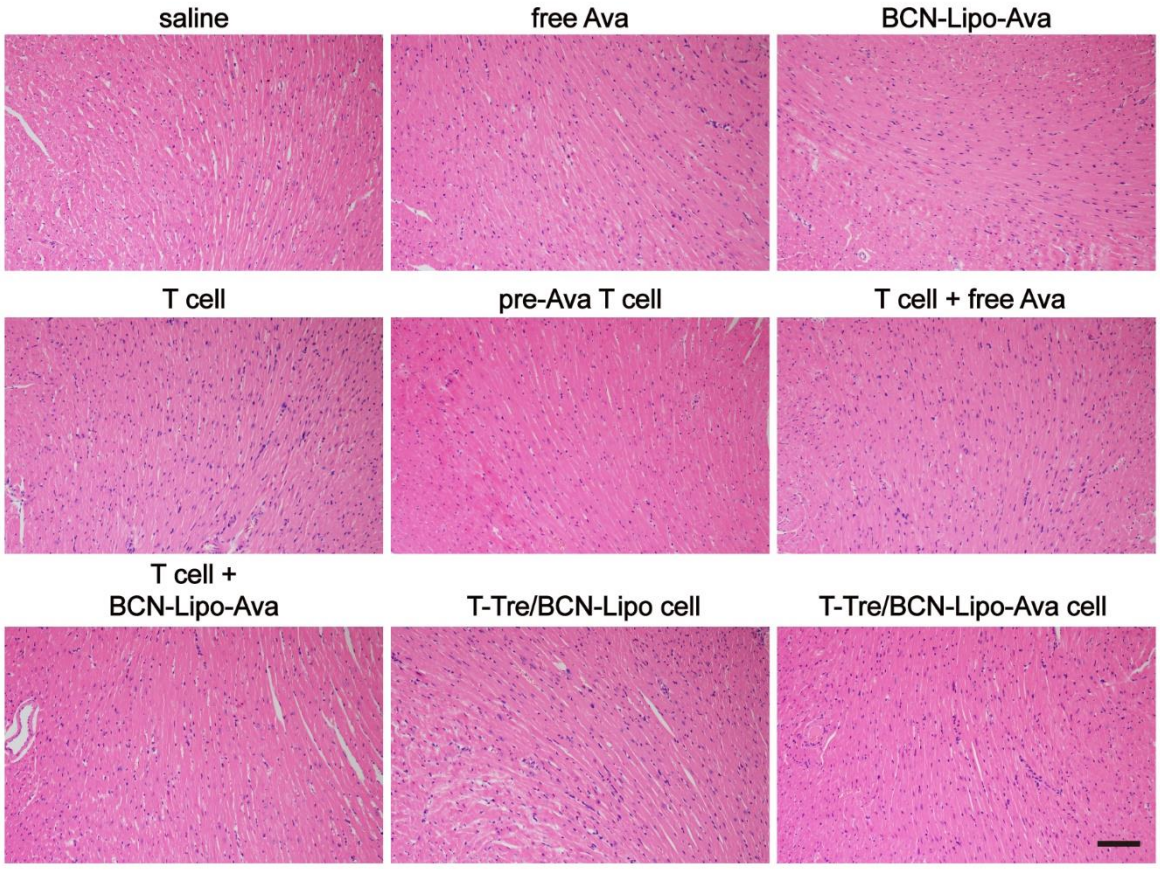

Fig. S16. Safety evaluation of heart tissue by microscopic pathological analysis in B16F10 orthotopic melanoma mouse model. Heart tissues were collected from the B16F10 bearing mice after administration of different treatments and HE sections were performed for pathological assessment. Scale bar, 50 μm.

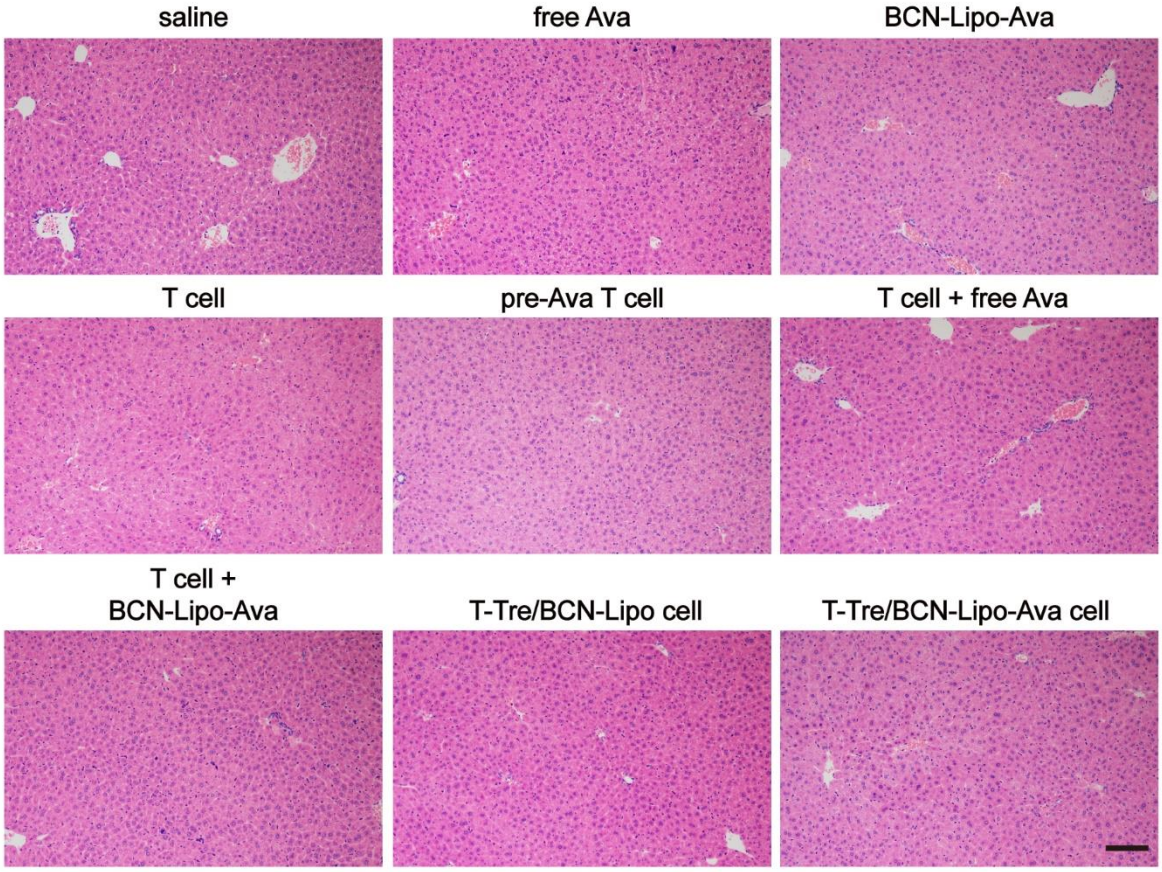

Fig. S17. Safety evaluation of liver tissue by microscopic pathological analysis in B16F10 orthotopic melanoma mouse model. Liver tissues were collected from the B16F10 bearing mice after administration of different treatments and HE sections were performed for pathological assessment. Scale bar, 50 μm.

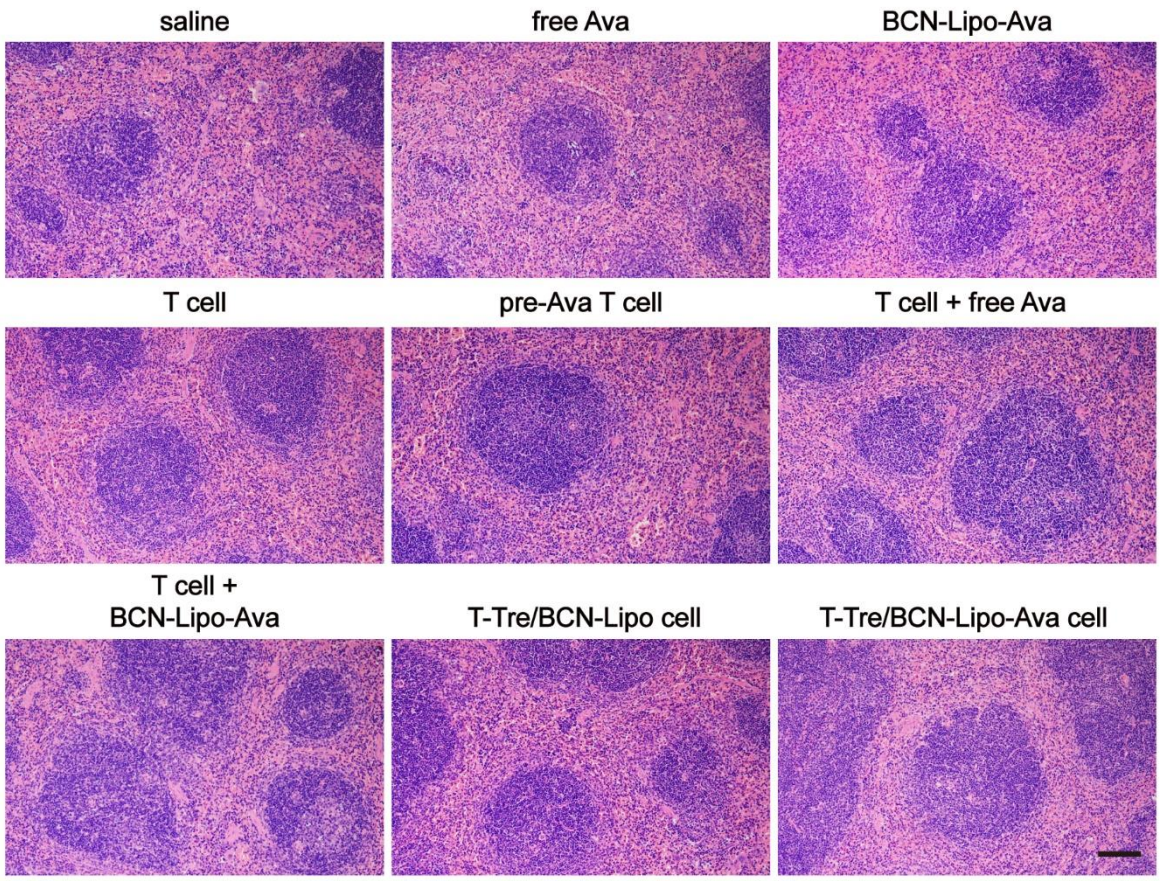

Fig. S18. Safety evaluation of spleen tissue by microscopic pathological analysis in B16F10 orthotopic melanoma mouse model. Spleen tissues were collected from the B16F10 bearing mice after administration of different treatments and HE sections were performed for pathological assessment. Scale bar, 50 μm.

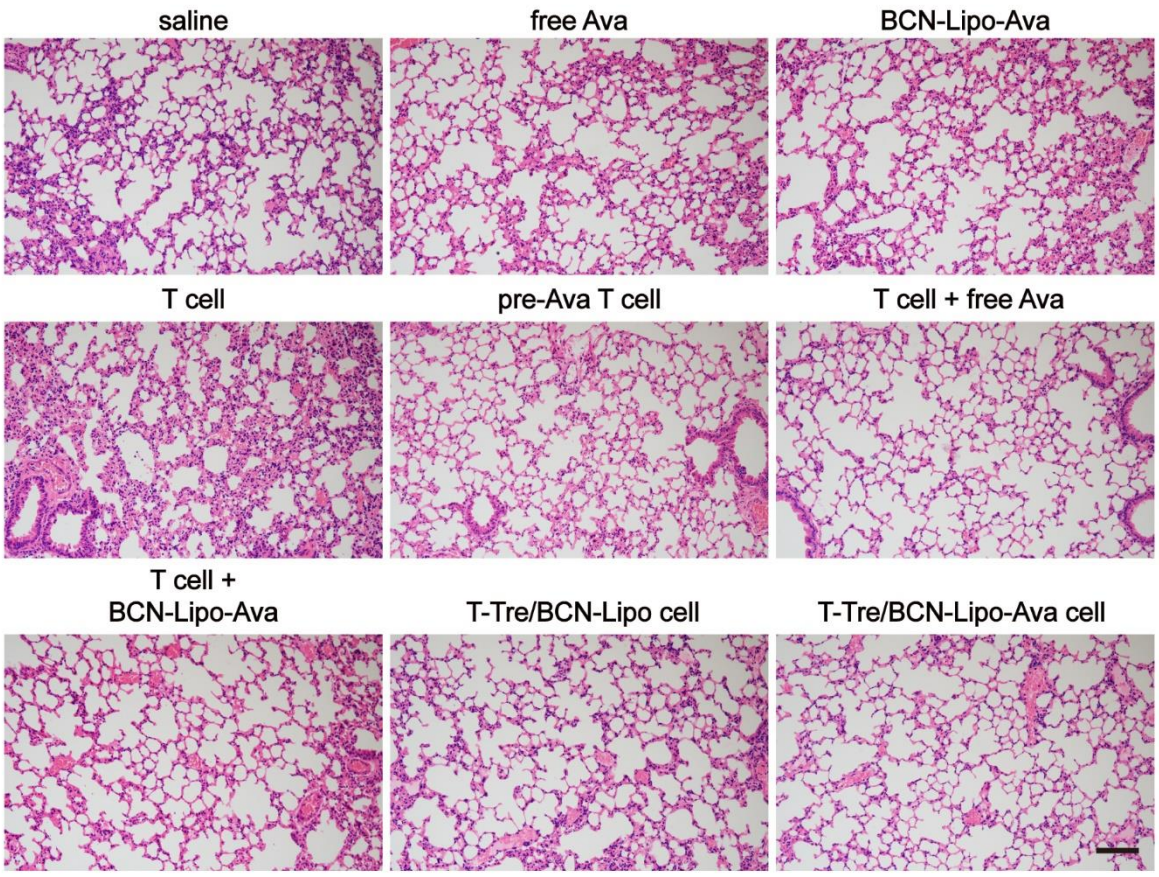

Fig. S19. Safety evaluation of lung tissue by microscopic pathological analysis in B16F10 orthotopic melanoma mouse model. Lung tissues were collected from the B16F10 bearing mice after administration of different treatments and HE sections were performed for pathological assessment. Scale bar, 50 μm.

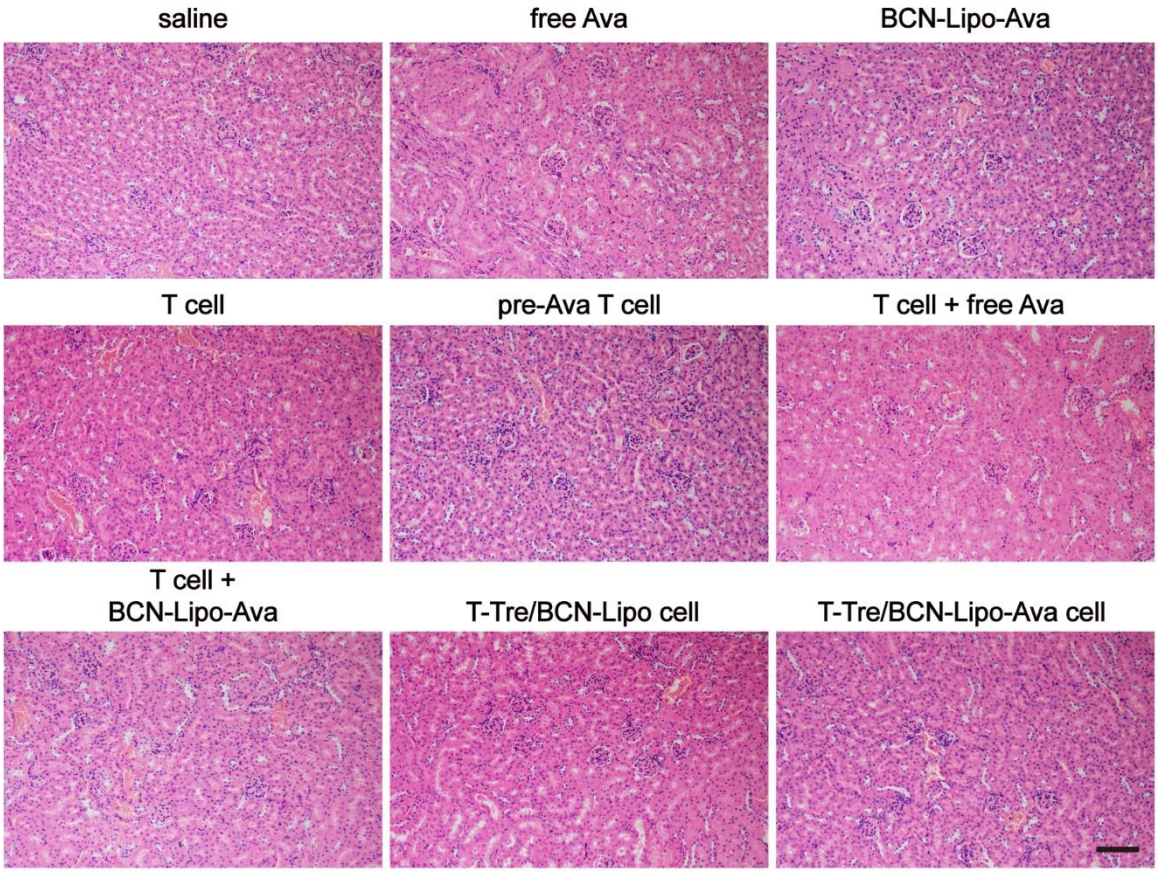

Fig. S20. Safety evaluation of kidney tissue by microscopic pathological analysis in B16F10 orthotopic melanoma mouse model. Kidney tissues were collected from the B16F10 bearing mice after administration of different treatments and HE sections were performed for pathological assessment. Scale bar, 50 μm.

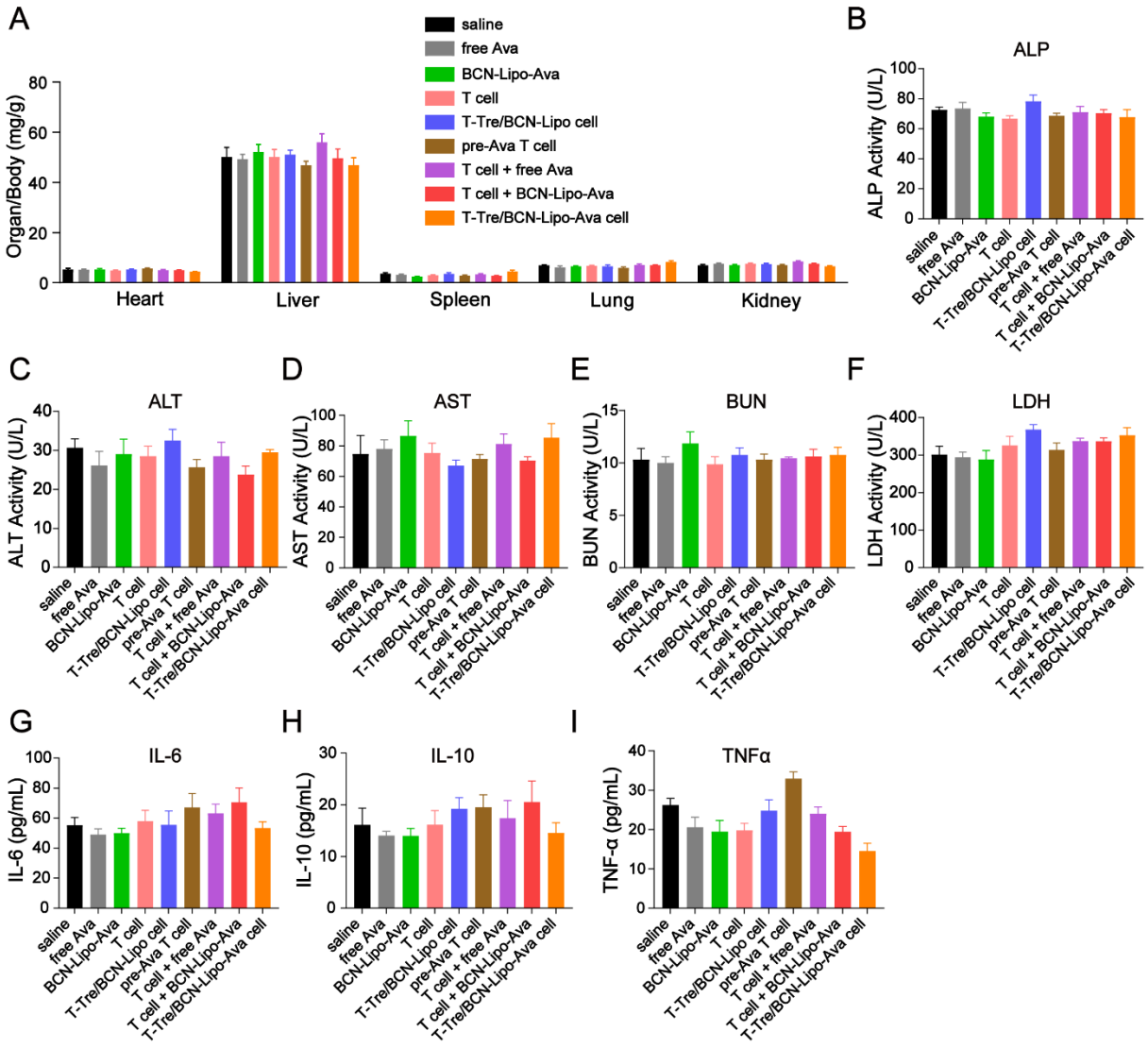

Fig. S21. Biosafety analysis of surface anchor-engineered pmel-1 T cell in B16F10 orthotopic melanoma. (A) Organ weight normalized to body weight (n = 6 mice/group). **(B-I)** Markers of liver/kidney injury and serum cytokine levels were measured (n = 6 mice/group). Error bars denote SEM.

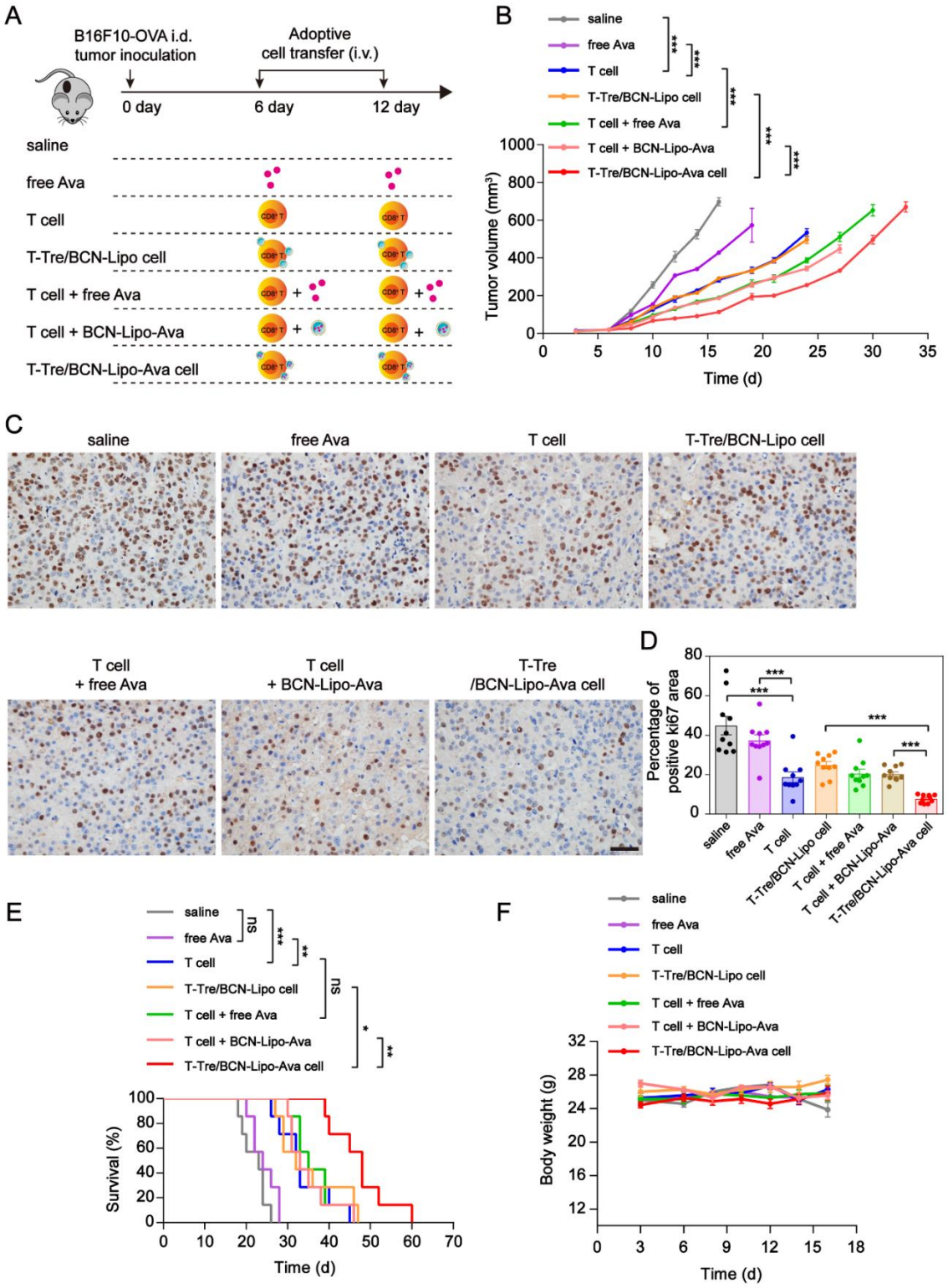

Fig. S22. Optimized synergistic antitumor efficacy of OT-I T-Tre/BCN-Lipo-Ava cell in B16F10-OVA orthotopic melanoma mouse model. (A) Schematic illustration of the experimental setting. **(B)** The tumor growth curves of mice receiving tested formulations, n =

7 mice/group. **(C-D)** Representative microscopic images **(C)** and quantification **(D)** of tumor sections immunostained by Ki-67. Ki-67 positive areas were quantified from each field (n = 10). Scale bar, 50 μm. **(E)** The survival profiles of mice receiving tested formulations, n = 7 mice/group. **(F)** Body weights of all mice, n = 7 mice/group. All data were analyzed by one-way ANOVA **(B)**, unpaired t-test **(D)** or a log-rank (Mantel-Cox) test **(E)**. Error bars denote SEM, $*P < 0.05$, $**P < 0.01$, $***P < 0.001$ and ns means no significant difference.

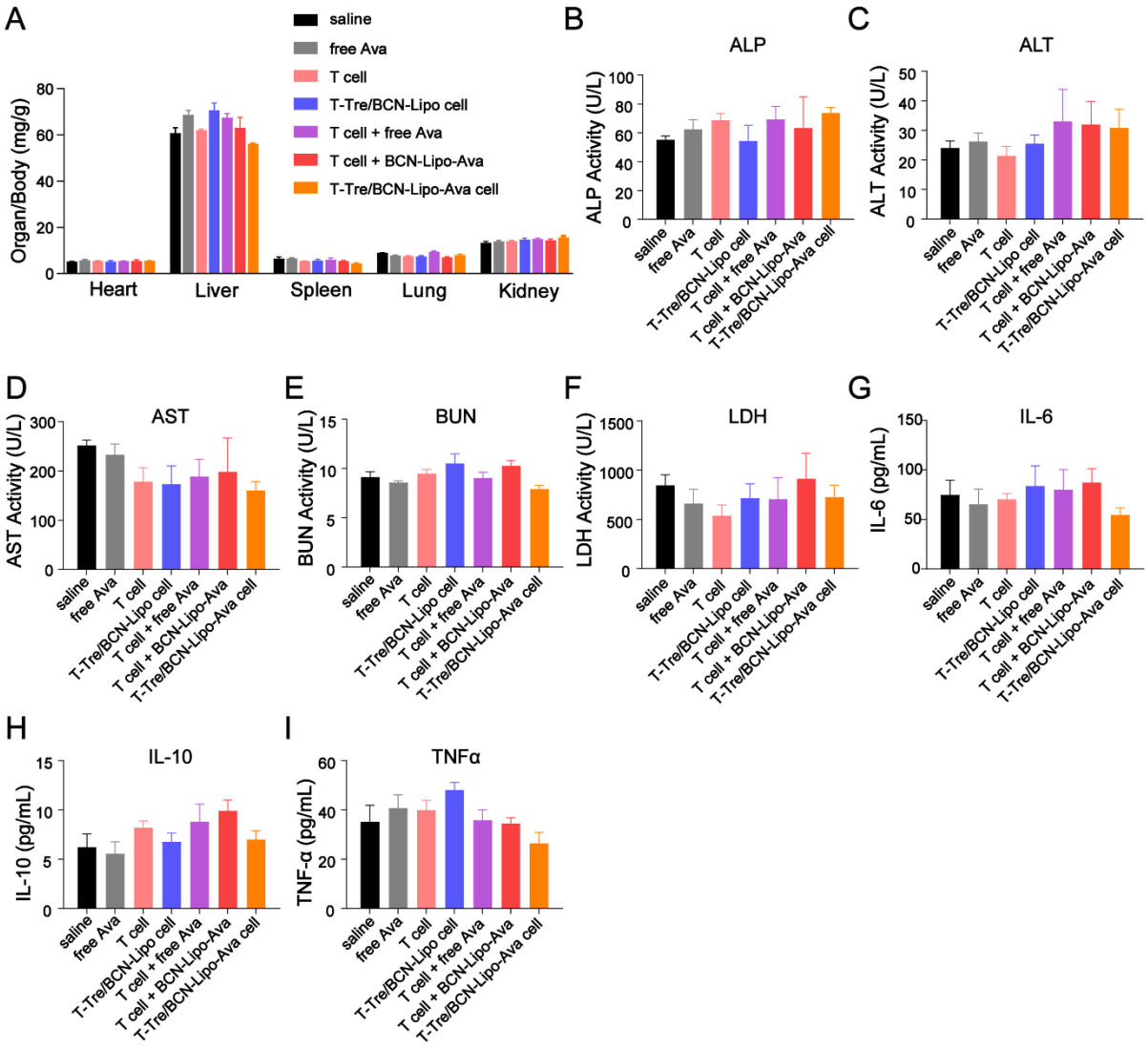

Fig. S23. Biosafety analysis of surface anchor-engineered OT-I T cell in B16F10-OVA orthotopic melanoma. (A) Organ weight normalized to body weight (n = 7 mice/group). **(B-I)** Markers of liver/kidney injury and serum cytokine levels were measured (n = 7 mice/group). Error bars denote SEM.

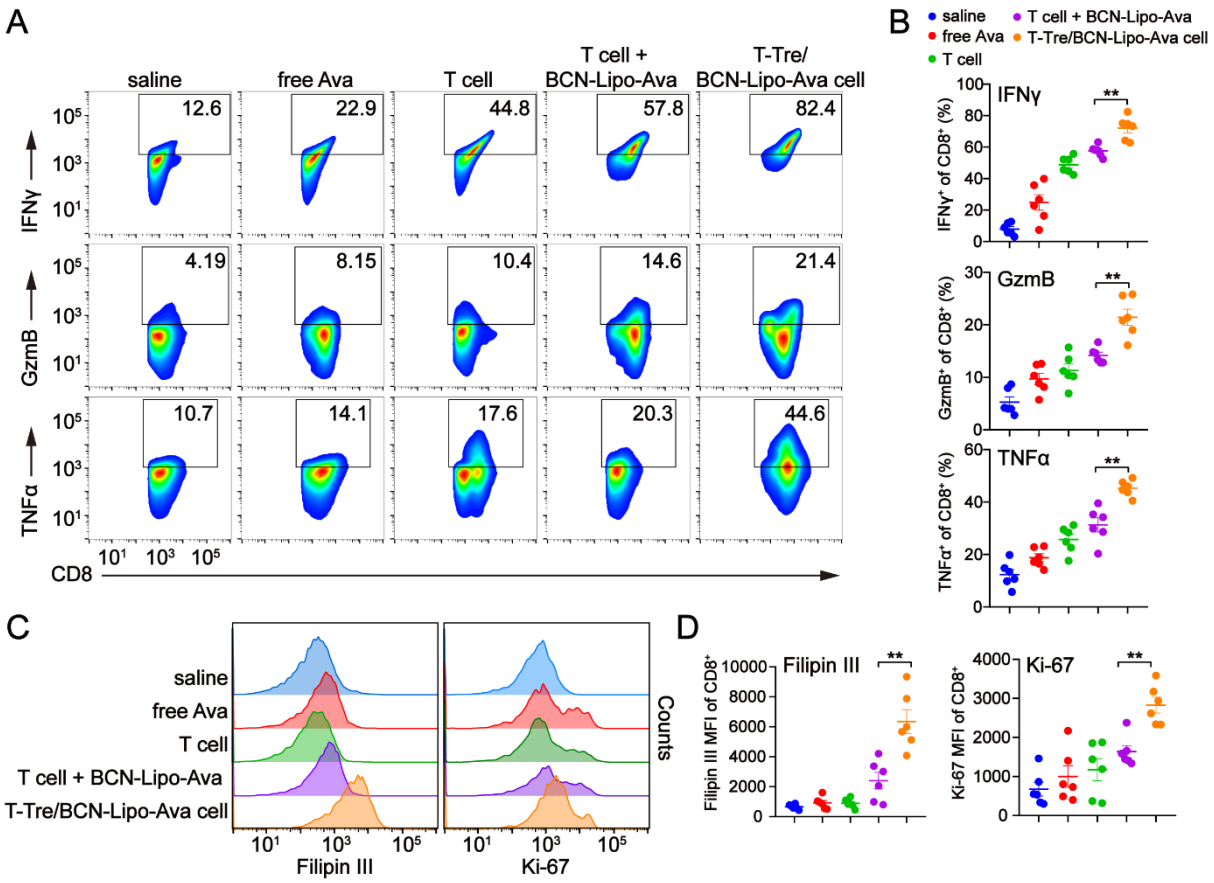

Fig. S24. Plasma membrane cholesterol level, Ki-67 expression, as well as IFNγ, TNFα and GzmB production of tumor-infiltrating CD8$^+$ T cell after a single adoptive pmel-1 T-Tre/BCN-Lipo-Ava cell transfer in B16F10 orthotopic melanoma tumors. (A-B) Flow cytometry analysis and quantification of TNFα$^+$, IFNγ$^+$, and GzmB$^+$ tumor-infiltrating CD8$^+$ T cells in B16F10 orthotopic melanoma tumors (n = 6 mice/group). **(C-D)** Filipin III and Ki-67 levels of tumour-infiltrating CD8$^+$ T cells were assessed using flow cytometry (n = 6 mice/group). Data were analyzed by unpaired t-test. Error bars denote SEM, $^{**}P < 0.01$ and ns means no significant difference.

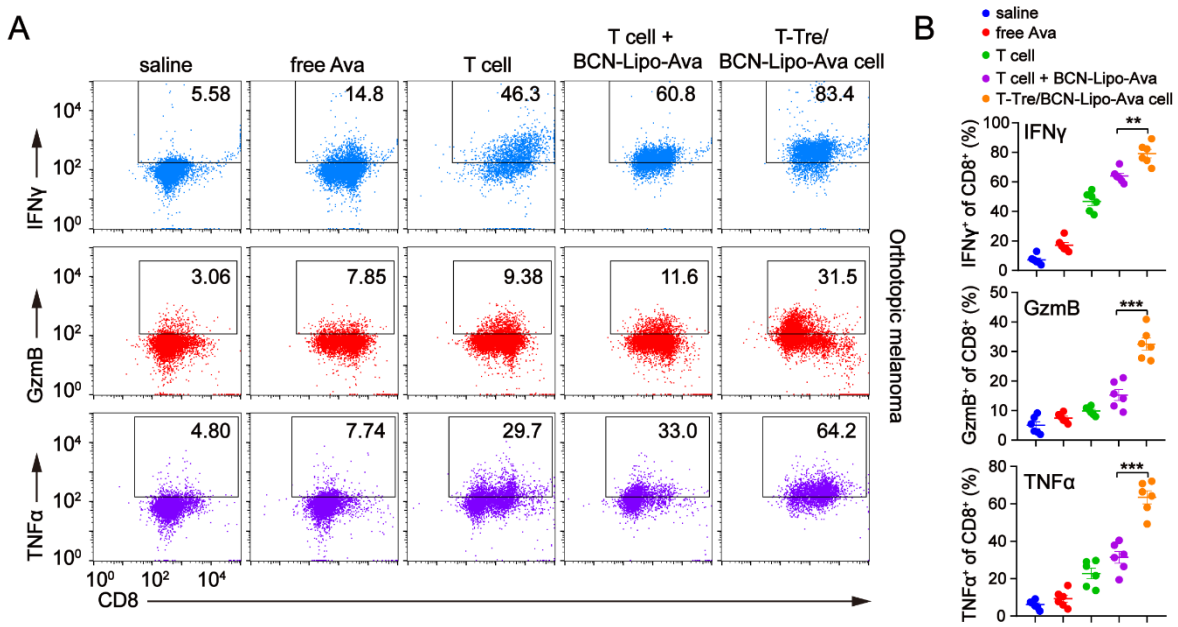

Fig. S25. IFNγ, TNFα and GzmB production of tumor-infiltrating CD8$^+$ T cell after a single adoptive OT-I T-Tre/BCN-Lipo-Ava cell transfer in B16F10-OVA orthotopic melanoma tumors. (A) Flow cytometry analysis and quantification of TNFα$^+$, IFNγ$^+$, and GzmB$^+$ tumor-infiltrating CD8$^+$ T cells in orthotopic melanoma tumors. **(B)** The quantification of **(A)**, n = 6 mice/group. All data were analyzed by unpaired t-test. Error bars denote SEM, $^{**}P < 0.01$, $^{***}P < 0.001$ and ns means no significant difference.

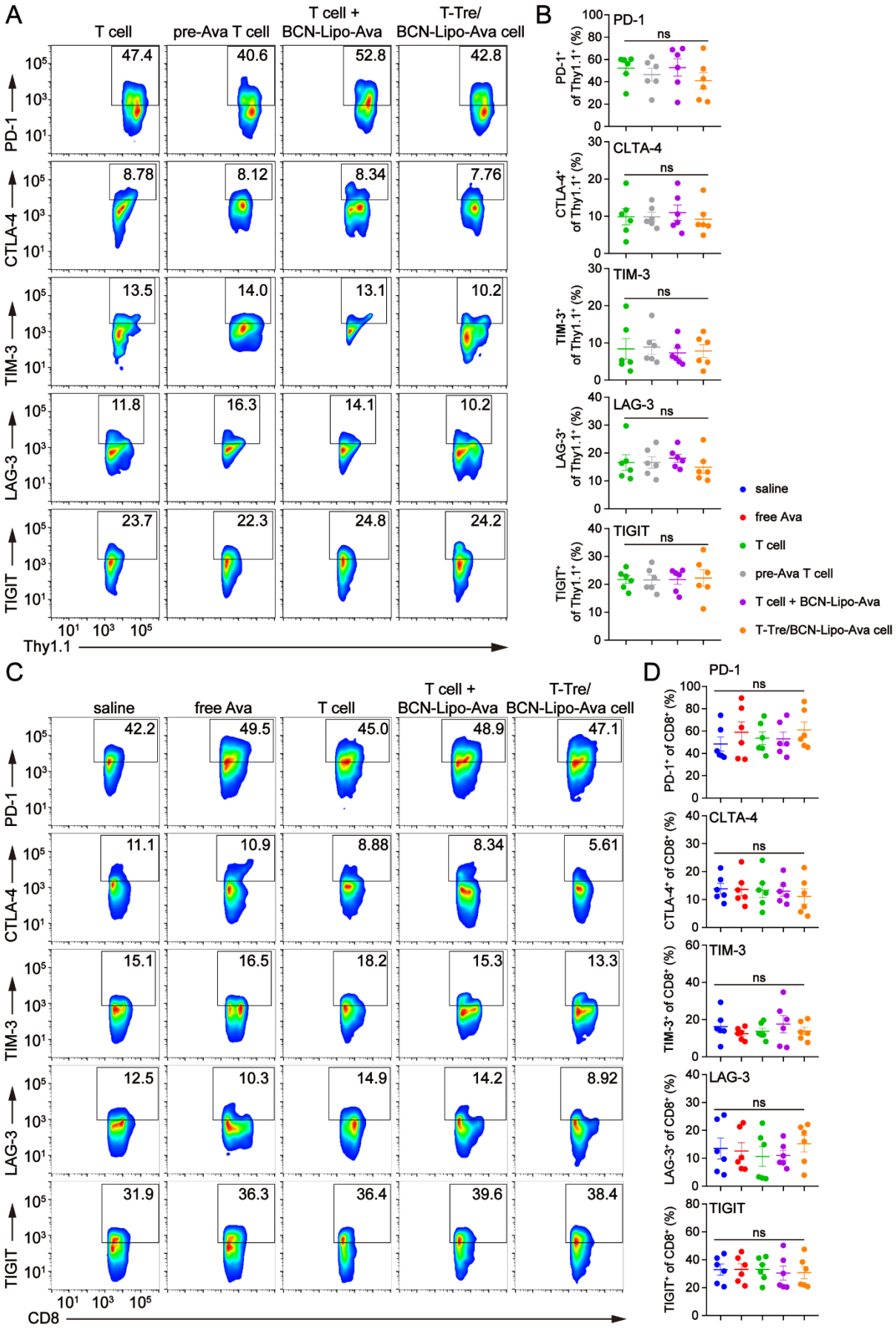

Fig. S26. The exhaustion and immunosuppressive status of adoptive transferred and

tumor-infiltrating CD8$^+$ T cell after a single adoptive pmel-1 T-Tre/BCN-Lipo-Ava cell transfer in B16F10 orthotopic melanoma tumors. (A-B) Flow cytometry analysis and quantification of PD-1$^+$, CTLA-4$^+$, TIM-3$^+$, LAG-3$^+$ and TIGIT$^+$ adoptive pmel-1 CD8$^+$ T cells in B16F10 orthotopic melanoma tumors (n = 6 mice/group). **(C-D)** Flow cytometry analysis and quantification of PD-1$^+$, CTLA-4$^+$, TIM-3$^+$, LAG-3$^+$ and TIGIT$^+$ tumor-infiltrating CD8$^+$ T cells in B16F10 orthotopic melanoma tumors (n = 6 mice/group). Data were analyzed by one-way ANOVA test. Error bars denote SEM, ns means no significant difference.

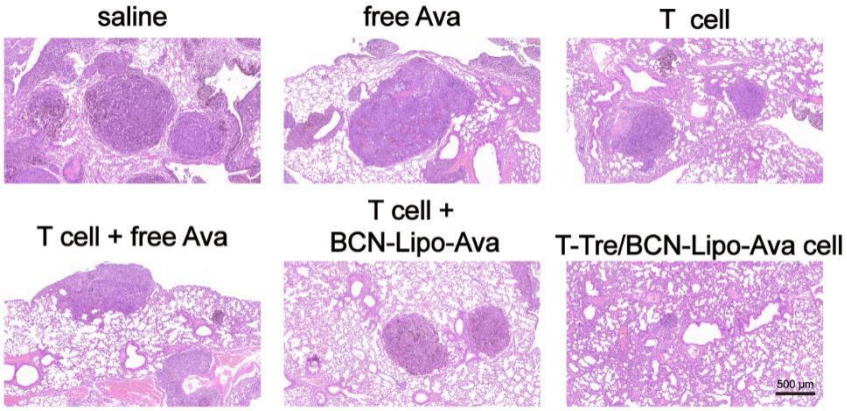

Fig. S27. Pathology analysis of pulmonary sections of B16F10-OVA metastatic melanoma. Local lung sections were photographed using imaged by a Microscope BX53 (Olympus) microscopy.

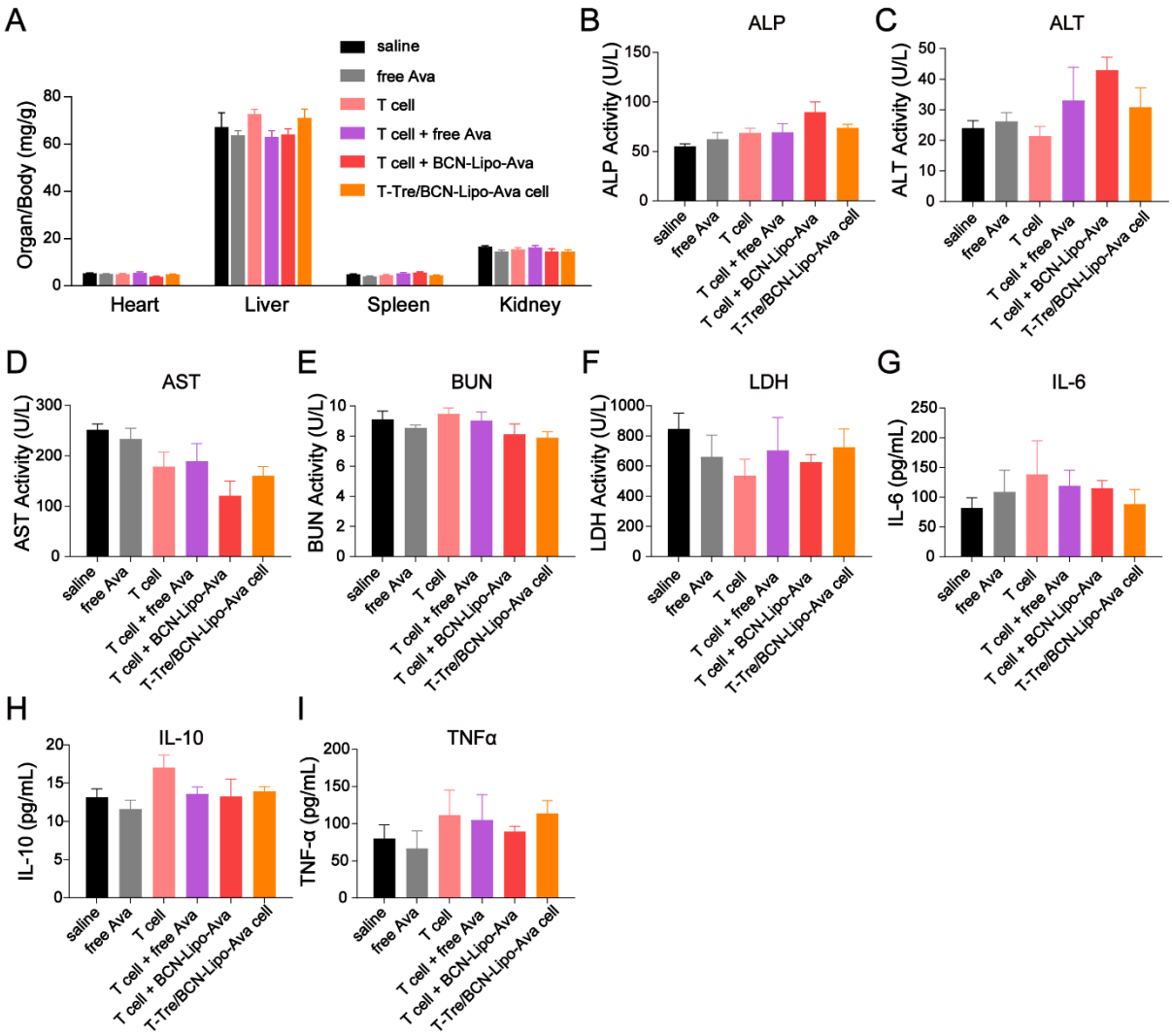

Fig. S28. Biosafety analysis of surface anchor-engineered OT-I T cell in B16F10-OVA pulmonary metastatic melanoma. (A) Organ weight normalized to body weight. **(B-I)** Markers of liver/kidney injury and serum cytokine levels were measured (n = 5 mice/group). Error bars denote SEM.

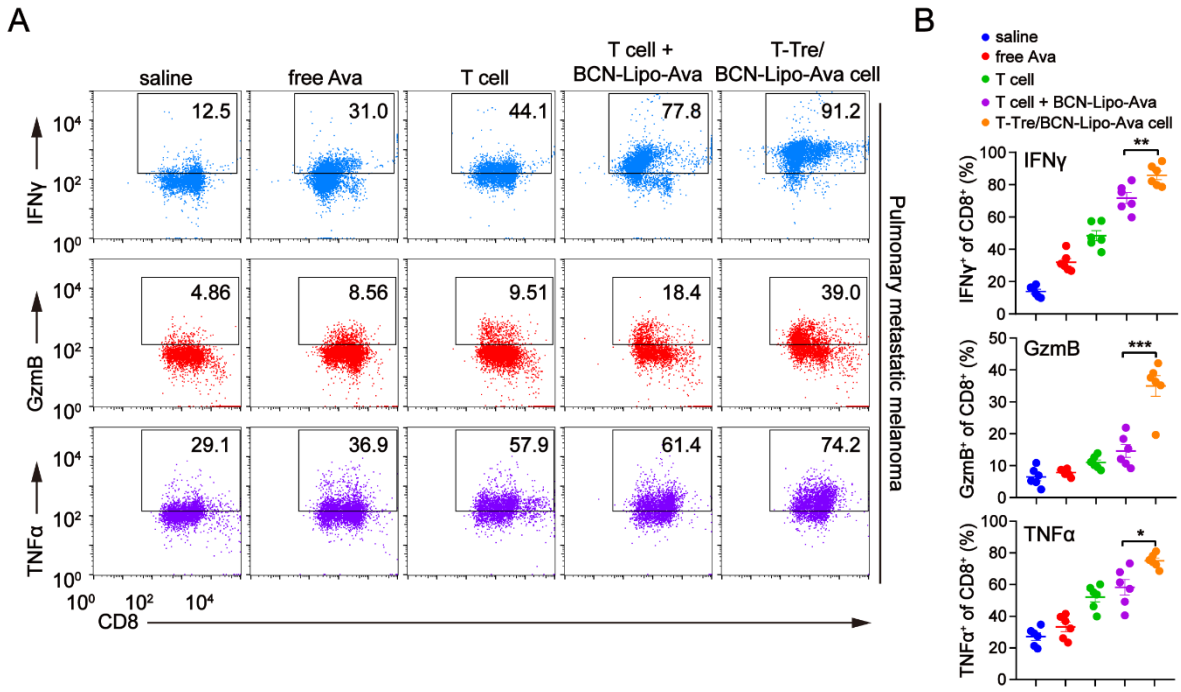

Fig. S29. IFNγ, TNFα and GzmB production of tumor-infiltrating CD8$^+$ T cell after a single adoptive OT-I T-Tre/BCN-Lipo-Ava cell transfer in B16F10-OVA pulmonary metastatic melanoma. (A) Flow cytometry analysis and quantification of TNFα$^+$, IFNγ$^+$, and GzmB$^+$ tumor-infiltrating CD8$^+$ T cells in pulmonary metastatic melanoma. **(B)** The quantification of **(A)**, n = 6 mice/group. All data were analyzed by unpaired t-test. Error bars denote SEM, *$P < 0.05$, **$P < 0.01$, ***$P < 0.001$ and ns means no significant difference.

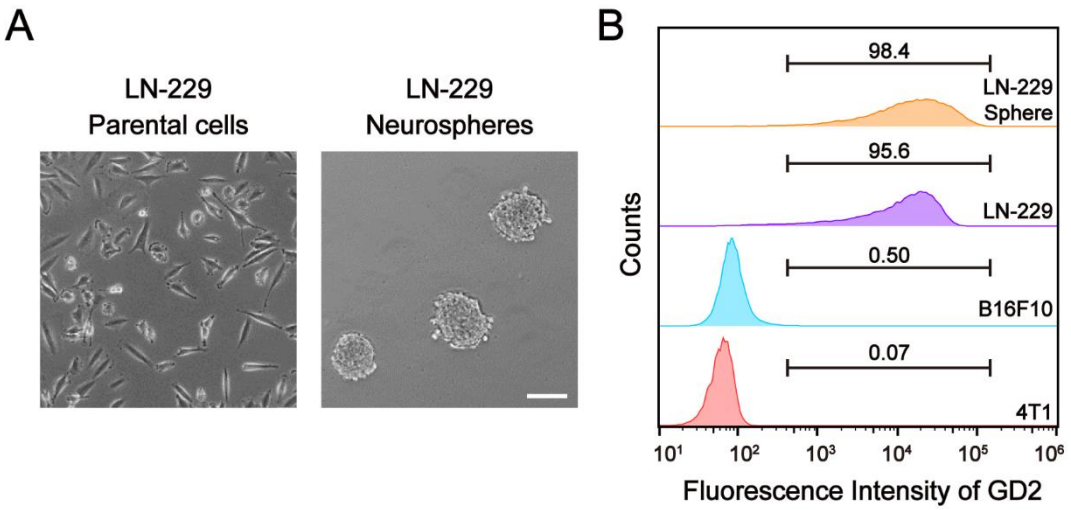

Fig. S30. Characteristics of LN-229 glioblastoma cells. (A) Morphology of LN-229 parental glioblastoma cells and LN-229 neurospheres. Scale bar, 100 μm. **(B)** The expressions of GD2 in LN-229 parental cells and LN-229 neurospheres were analyzed by flow cytometry. 4T1 breast cancer cells and B16F10 melanoma cells were set as controls.

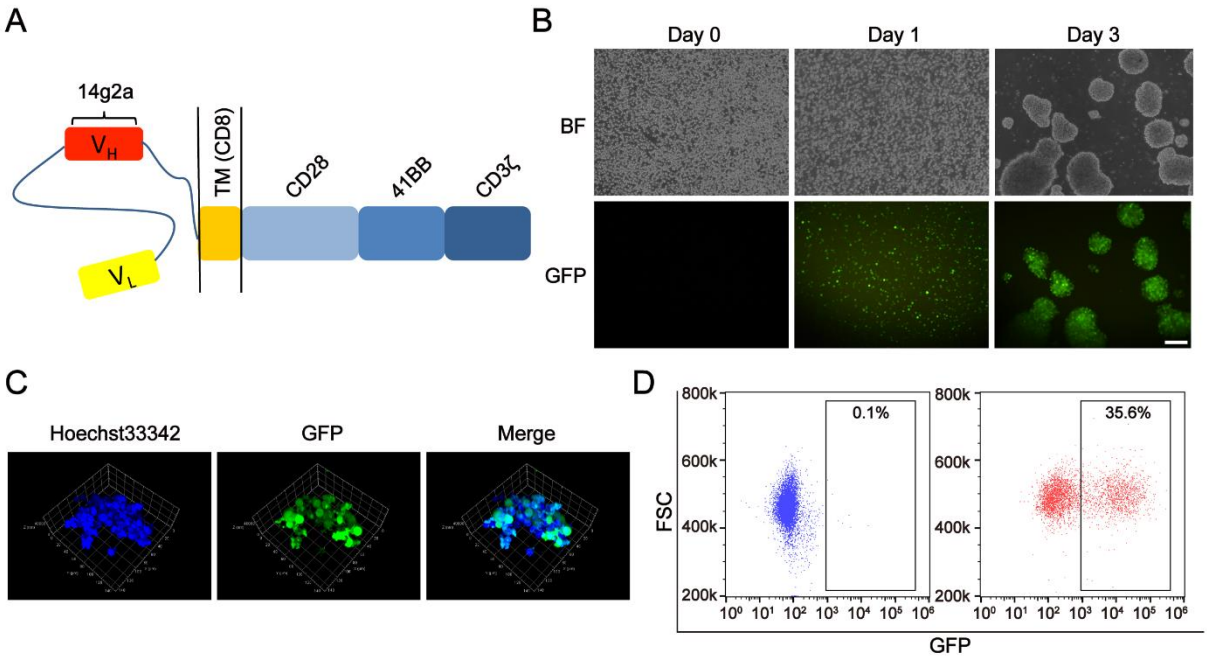

Fig. S31. Characteristics of anti-GD2 CAR-T cells. (A) Schematic of the GD2.CD28.4-1BB.z-CAR used in functional experiments. V_H, variable heavy chain; V_L, variable light chain. **(B)** Lentiviral transduction efficiency of GD2 CAR in human pan $CD3^+$ T cells determined by fluorescence imaging at different time points after transduction. The GFP green signals indicated positive GD2 CAR-T cells. Scale bar, 200 μm. **(C)** 3D z-stack of GD2 CAR-T cell cluster was imaged by ZEISS confocal and analyzed by Arivis 3D imaging system after the transduction of GD2 CAR for 2 days. The Hoechst 33342 blue signals indicated DNA staining, while the GFP green signals indicated positive GD2 CAR-T cells. **(D)** Lentiviral transduction efficiency of GD2 CAR in human pan $CD3^+$ T cells determined by flow cytometry.

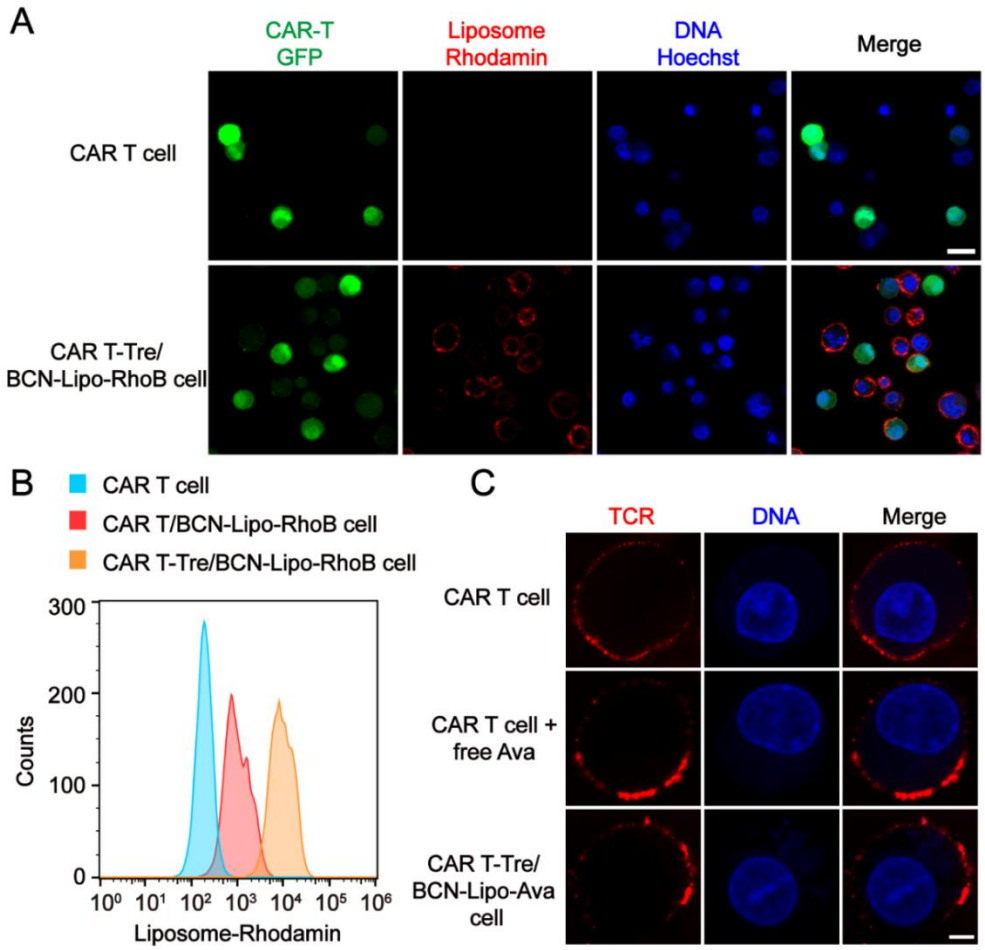

Fig. S32. Surface-anchoring of CAR-T cells by liposomal Ava enhanced TCR clustering and immunological synapse formation. (A) Confocal microscopy images of CAR-T cells after anchoring with Rhodamine B-labeled liposomes (BCN-Lipo-RhoB, red). CAR-T cell nuclei were stained by Hoechst 33342 (blue). Scale bar, 10 μm, n = 2 independent experiments. **(B)** Hydrophobic anchored CAR-T cells were incubated with fluorescent liposome (BCN-Lipo-RhoB) and then analyzed by flow cytometry, n = 3 independent samples per group. **(C)** Imaging of TCR clustering of CAR T-Tre/BCN-Lipo-Ava cell after stimulation with anti-CD3/CD28 antibodies. The TCRα was labeled with Alexa Fluor 647 (red) and cell nuclei were stained by Hoechst 33342 (blue). Scale bar, 5 μm, n = 2 independent experiments.

Table S1. The number of liposomes anchored on the surface of T cell.

$N_{\text{before DSPE-PEG-Tre}}$	$N_{\text{after DSPE-PEG-Tre}}$	$N_{\text{before DSPE-PEG}}$	$N_{\text{after DSPE-PEG}}$	$N_{\text{liposome per T cell}}$
$7.80\times10^8 \pm 0.18\times10^8$	$4.45\times10^8 \pm 0.28\times10^8$	$7.96\times10^8 \pm 1.39\times10^8$	$7.36\times10^8 \pm 1.39\times10^8$	274 ± 38

Data were presented mean ± SD, n = 3 independent samples per group. Detailed calculation was summarized in preparation and characterization of T-Tre/BCN-Lipo-Ava cell of Materials and Methods.

Supporting Methods

1. Synthesis of cell membrane anchoring module (DSPE-PEG$_{5k}$-Tre)

1.1 Synthesis of 4-(6-(pyrimidin-2-yl)-1,4-dihydro-1,2,4,5-tetrazin-3-yl) benzo-icacid (Tre-2H-COOH)

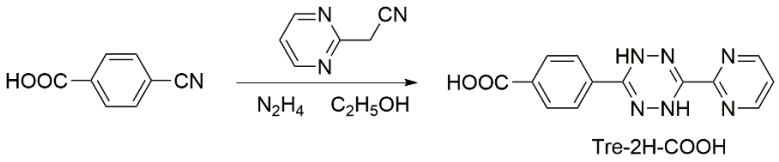

To a solution of 2-cyanopyrimidine (935 mg, 8.9 mmol) in ethanol (30 mL) was added 4-cyanobenzoic acid (1.96 g, 13.3 mmol). Upon all the 4-cyanobenzoic acid has dissolved, hydrazine hydrate (5.5 mL) was added slowly, and the brown mixture turned red immediately. The reaction mixture was allowed to reflux for 10 hours. After the reaction was cooled down to room temperature, the mixture was filtered to remove the filtrate. Then, drying the filter cake. 520 mg of henna powder of 4-(6-(pyrimidin-2-yl)-1,4-dihydro-1,2,4,5-tetrazin-3-yl) benzoic acid was obtained. Yield: 20.7%.

1.2 Synthesis of 4-(6-(pyrimidin-2-yl)-1,2,4,5-tetrazin-3-yl) benzoic acid (Tre-COOH)

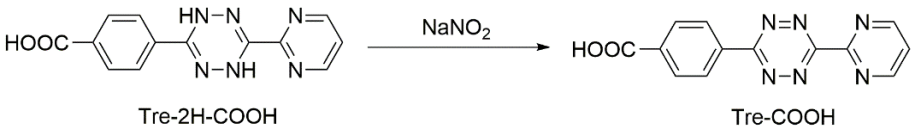

In a 50 mL round bottom flask, Tre-2H-COOH (520 mg, 1.8 mmol) in Acetic acid glacial (10 mL) and $NaNO_2$ (2.76 g, 40 mmol) was added slowly. The mixture was stirred for 0.5 h and filtered it under the negative pressure before we collected the filter cake. 10 mL DMF was added to dissolve the crude product in the filter cake. The suspension was filtered, concentrated under reduced pressure and purified via silica gel flash chromatography (CH_2Cl_2/MeOH = 10:1) to

give 200 mg Tre-COOH as prunosus solid. Yield: 38.7%. Structure confirmed by ^{1}H-NMR and HRMS. ^{1}H-NMR (300 MHz, DMSO-d_6), δ_H (TMS, ppm) : 9.20 (2H, d, J = 4.8 Hz)， 8.70 (2H, d, J = 8.3 Hz), 8.25 (2H, d, J = 9.9 Hz), 7.83 (1H, t, J = 4.8 Hz). HRMS: m/z calcd for $C_{13}H_8N_6O_2$ $(M-H)^-$: 279.0636 was found 279.0643.

1.3 Synthesis of N^2-(tert-butoxycarbonyl)-N^6-(4-(6-(pyrimidin-2-yl)-1,2,4,5-tetrazin-3-yl)benzoyl)lysine (Lys-Boc-Tre)

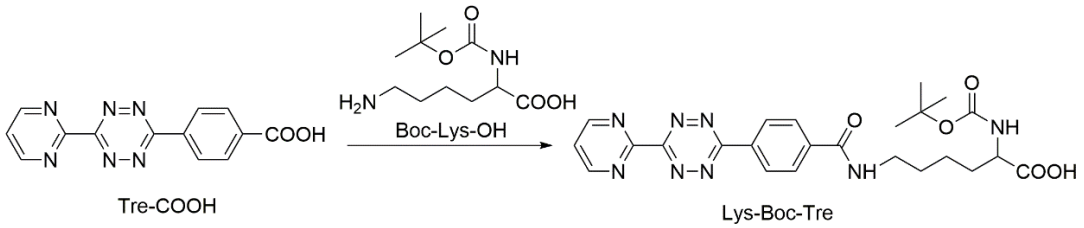

In a 100 mL round bottom flask, a solution of 80.00 mg (0.29 mmol) of Tre-COOH, 35.68 mg (0.31 mmol) of N-hydroxysuccinimide, 59.43 mg (0.31 mmol) of 1-(3-Dimethylaminopropyl)-3-ethylcarbodiimide hydrochloride in 30 mL of $CHCl_3$ stirred for 3 h. To a solution of Boc-Lys-OH·HCl (126.42 mg, 0.26 mmol) in $CHCl_3$ (30 mL) was added DIPEA (136.24 μL, 0.78 mmol) with stirring for 3 h. Then, the mixture of Boc-Lys-OH·HCl and DIPEA in $CHCl_3$ was added to the solution of Tre-COOH, N-hydroxysuccinimide and 1-(3-Dimethylaminopropyl)-3-ethylcarbodiimide hydrochloride in $CHCl_3$, then stirred overnight at room temperature. The reaction mixture washed with 1% citric acid (2×80 mL) and brine (2×80 mL). The organic layer was dried over Na_2SO_4 and the solvent evaporated. The product was purified by flash chromatography (chloroform / MeOH = 25:1) and isolated as a prunosus solid (90 mg, 61.9 %). Structure confirmed by ^{1}H-NMR. ^{1}H-NMR (300 MHz, $CDCl_3$), δ_H (TMS, ppm) : 9.12 (2H, d, J = 4.8 Hz), 8.78 (2H, d, J = 8.5 Hz), 8.06 (2H, d, J = 8.5 Hz), 7.63 (1H, t,

J = 4.8 Hz), 4.20 (1H, t, J = 4.6 Hz), 3.47-3.43 (2H, m), 1.76-1.65 (4H, m), 1.52-1.48 (2H, m), 1.40 (9H, s).

1.4 Synthesis of 1,2-distearoyl-sn-glycero-3-phosphoethanolamine-*N*-(polyeth-ylene glycol)-5000-N^2-(tert-butoxycarbonyl)-N^6-(4-(6-(pyrimidin-2-yl)-1,2,4,5-te-trazine-3-yl) benzoyl) lysine (DSPE-PEG$_{5k}$-Lys-Boc-Tre)

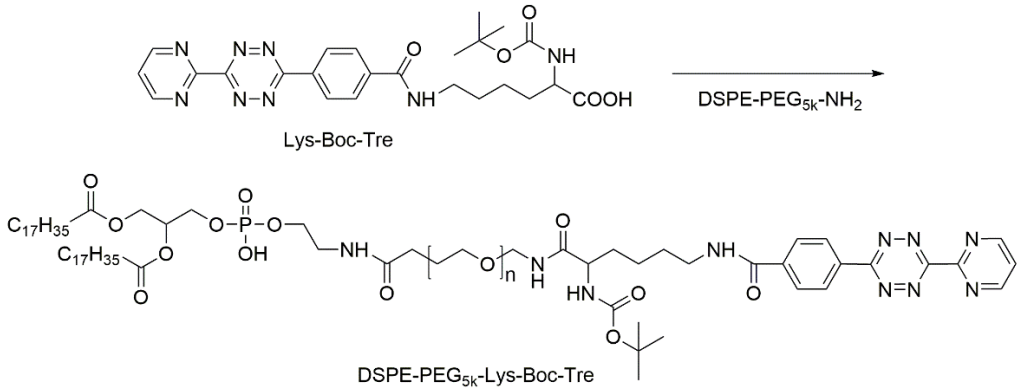

To a solution of DSPE-PEG$_{5k}$-NH$_2$ (50.00 mg, 0.01 mmol) in DMF (5 mL), were added benzotriazole-1-yl-oxytripyrrolidinophosphonium hexafluorophosphate (11.45 mg, 0.022 mmol), Triethylamine (4.09 μL, 3.03 mmol) and Lys-Boc-Tre (10.52 mg, 0.02 mmol) with stirring overnight at room temperature. The reaction mixture was transferred to a dialysis bag (MWCO = 3500 Da). After dialysis for 48 h with DMSO, deionized water for further dialysis for 48 h. A purple-red cotton-like product (DSPE-PEG$_{5k}$-Lys-Boc-Tre, 31.7 mg) was obtained by lyophilization. Yield: 60.8%. Structure confirmed by ^{1}H-NMR. ^{1}H-NMR (300 MHz, DMSO-d_6), δ_H (TMS, ppm) : 9.21 (2H, d, J = 4.4 Hz), 9.11 (2H, d, J = 5.2 Hz), 8.67 (2H, d, J = 8.7 Hz), 8.16 (2H, m), 7.84 (1H, t, J = 5.1 Hz), 6.87 (2H, s), 4.58-4.25 (5H, m), 4.19-4.14 (7H, m), 4.68-4.02 (6H, m), 3.75-3.69 (16H, m), 3.50-3.49 (452H, m), 2.72 (4H, m), 2.26-2.25(9H, m), 1.77-1.76 (1H, m), 1.55-1.49 (9H, m), 1.36 (9H, s), 1.22-1.01 (45H, m), 0.84 (6H, t, J = 6.2

Hz).

1.5 Synthesis of 1,2-distearoyl-sn-glycero-3-phosphoethanolamine-*N*-(polyethylene glycol)-5000-N^6-(4-(6-(pyrimidin-2-yl)-1,2,4,5-tetraazin-3-yl) benzoyl) lysine acid (DSPE-PEG_{5k}-Tre)

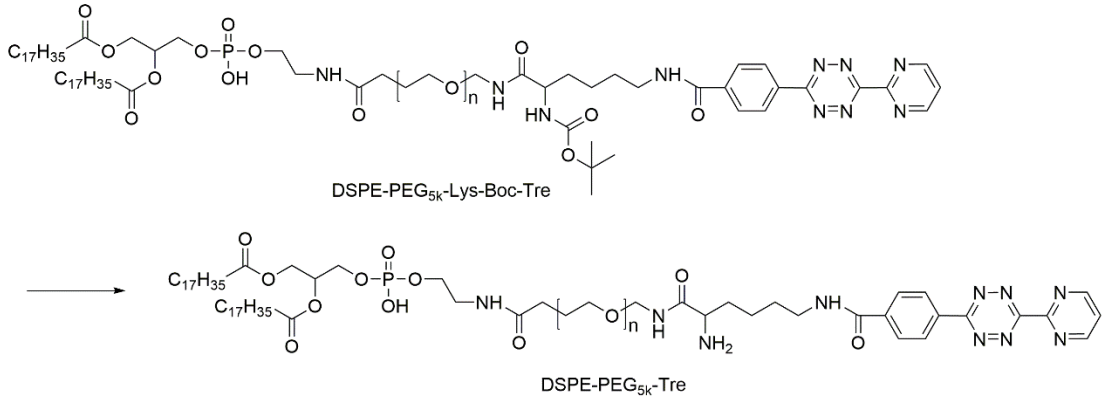

To a solution of 31.70 mg of DSPE-PEG_{5k}-Lys-Boc-Tre in deionized water (5 mL), were added 136.24 μL of TFA with stirring overnight. The reaction mixture was transferred to a dialysis bag (MWCO = 3500 Da). After dialysis for 48 h with deionized water, a purple-red cotton-like product (DSPE-PEG_{5k}-Lys-Tre, 20 mg) was obtained by lyophilization. Structure confirmed by ^{1}H-NMR.^{1}H-NMR (300 MHz, DMSO-d_6), δ_H (TMS, ppm) : 9.21 (2H, d), 8.68 (1H, d), 8.19 (2H, d), 7.51 (2H, d), 5.11-5.19 (4H, m), 4.57-4.52 (7H, m), 4.10-3.99 (9H, m), 3.77-3.68 (8H, m), 3.53-3.46 (475H, m), 2.32-2.19 (5H, m), 1.56-1.40 (7H, m), 1.25-1.20 (45H, m), 0.85 (6H, t).

1.6 Synthesis of 1,2-distearoyl-sn-glycero-3-phosphoethanolamine-*N*-(polye-thylene glycol)-5000-N^6-(4-(6-(pyrimidin-2-yl)-1,2,4,5-tetraazin-3-yl) benzoyl) ly-sine acid-FITC (DSPE-PEG_{5k}-Tre-FITC)

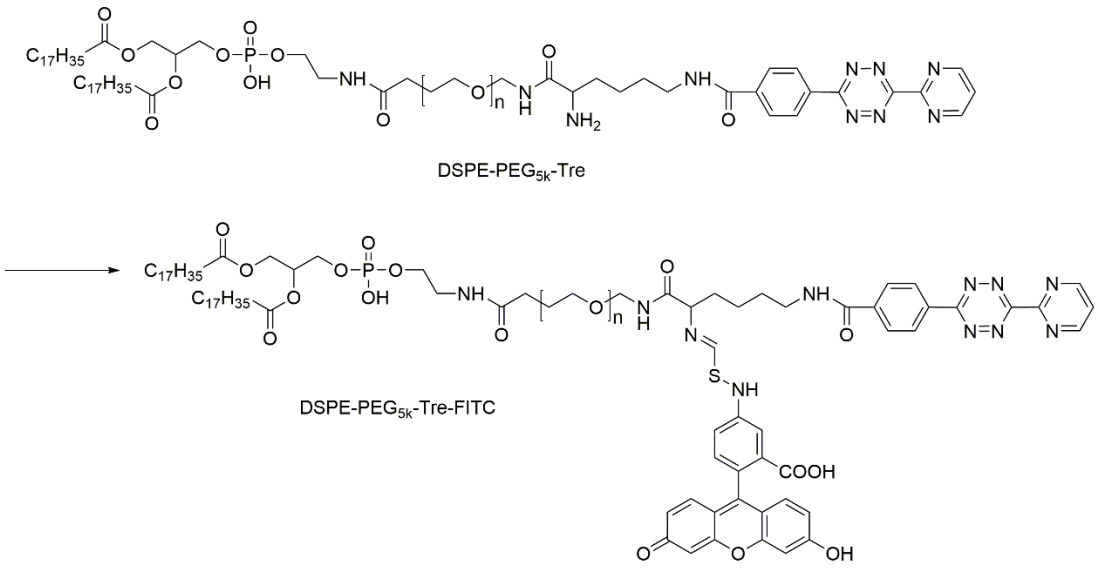

To a solution of 10 mg FITC in DMSO (1 mL), were added DSPE-PEG$_{5k}$-Tre (2 mg/mL) in PBS (5 mL, pH = 8.5) with stirring overnight. The reaction mixture was transferred to a dialysis bag (MWCO = 3500 Da). The reaction mixture was transferred to a dialysis bag (MWCO = 3500 Da). After dialysis for 48 h with DMSO, deionized water for further dialysis for 48 h. A yellow and green cotton-like product (DSPE-PEG$_{5k}$-Tre-FITC, 9.2 mg) was obtained by lyophilization. Structure confirmed by ^{1}H-NMR.

1.7 Synthesis of 1,2-distearoyl-sn-glycero-3-phosphoethanolamine-*N*-(polye-thylene glycol) -5000-FITC (DSPE-PEG$_{5k}$-FITC)

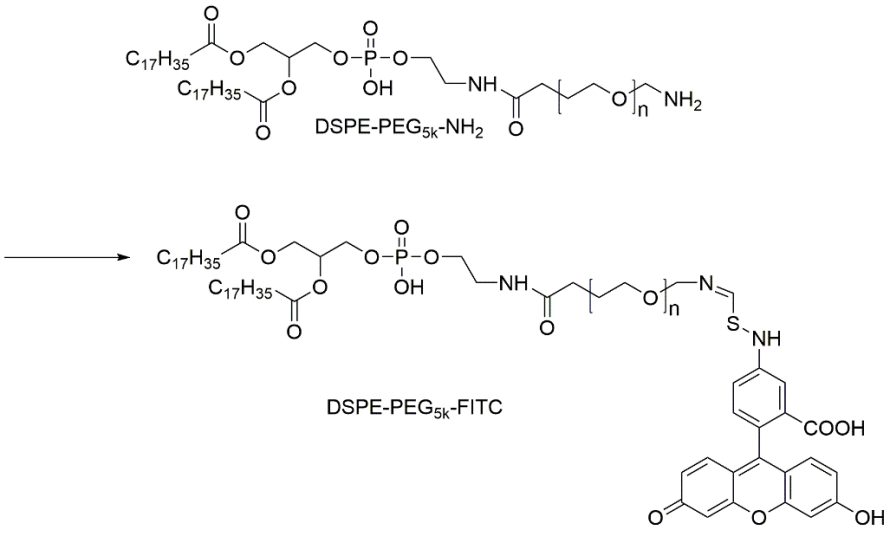

To a solution of 10 mg FITC in DMSO (1 mL), were added DSPE-PEG_{5k}-NH_2 (2 mg/mL) in PBS (5 mL, pH = 8.5) with stirring overnight. The reaction mixture was transferred to a dialysis bag (MWCO = 3500 Da). The reaction mixture was transferred to a dialysis bag (MWCO = 3500 Da). After dialysis for 48 h with DMSO, deionized water for further dialysis for 48 h. A yellow and green cotton-like product (DSPE-PEG_{5k}-Tre-FITC, 8.5 mg) was obtained by lyophilization. Structure confirmed by ^{1}H-NMR. ^{1}H-NMR (300 MHz, DMSO-d_6), δ_H (TMS, ppm) :7.46 (3H, m), 6.25 (6H, m), 5.45-5.39 (4H, m), 4.61-4.53 (4H, m), 4.05-4.01 (6H, m), 3.75-3.50 (426H, m), 2.28-2.24 (4H, m), 1.24-1.11 (55H, m), 1.02 (6H, t).

2. Synthesis of lipid click module（DSPE-BCN）

2.1 Synthesis of ethyl bicyclo [6.1.0] non-4-ene-9-carboxylate (1)

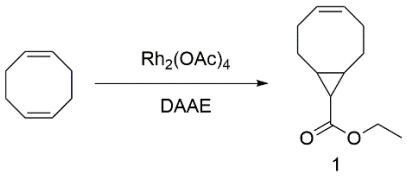

To a solution of 1,5-Cyclooctadiene (30 mL, 26.40 g, 0.24 mol) in CH_2Cl_2 (100 mL), were added rhodium (II) acetate dimer and ethyl diazoacetate (DAAE)/CH_2Cl_2 (4.3 mL/20 mL, 0.04

mol, 4.6 g) with stirring for 24 h at room temperature. Then, the reaction mixture was poured into 600 mL heptane/ethyl acetate (200:1) with stirring for 1 h. After the suspension was filtered, concentrated under reduced pressure and purified via silica gel flash chromatography (PE:EA = 50:1) 5.6 g of colorless oily liquid of **1** was obtained. Yield: 72.16%. Structure confirmed by ^{1}H-NMR. ^{1}H-NMR (300 MHz, $CDCl_3$), δ_H (TMS, ppm) : 5.65-5.54 (2H, m, -CH=CH-), 4.14-4.07 (2H, q, -O-CH_2-CH_3), 2.53-2.46 (2H, m, =CH-CH_2-CH_2-), 2.25-2.13 (2H, m, =CH-CH_2-CH_2-), 2.09-1.98 (2H, m, -CH-CH_2-CH_2-), 1.87-1.78 (2H, m, -CH_2-CH(CHCOO)-CH-, -CH_2-CH(CHCOO)-CH-), 1.72-1.66 (1H, t, -OC-CH(CH)-CH-), 1.44-1.32 (2H, m, -CH_2-CH_2-CH-), 1.27-1.22 (3H, t, -OCH_2CH_3).

2.2 Synthesis of bicyclo [6.1.0] non-4-en-9-ylmethanol (2)

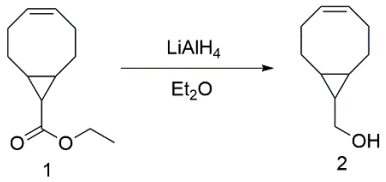

In a 125 mL round bottom flask, a solution of **1** (3.7 g, 19.05 mmol), $LiAlH_4$ (1.09 g, 28.59 mmol) in 50 mL of Et_2O stirred for 4 h at room temperature. The reaction mixture diluted with Et_2O and washed with brine (2×80 mL). The organic layer was dried over Na_2SO_4. Then, the solvent evaporated to obtain crude product (2.78 g, 96%). Structure confirmed by ^{1}H-NMR. ^{1}H-NMR (300 MHz, $CDCl_3$), δ_H (TMS, ppm) : 5.69-5.58 (2H, m, -CH=CH-), 3.48 (2H, d, HO-CH_2-CH-), 2.33-2.24 (2H, m, =CH-CH_2-CH_2-), 2.22-2.12 (2H, m, =CH-CH_2-CH_2-), 2.09-2.01 (2H, m, -CH-CH_2-CH_2-), 1.47-1.35 (2H, m, -CH-CH_2-CH_2-), 0.83-0.72 (2H, m, -CH_2-CH(CH_2)-CH-, -CH_2-CH(CH_2)-CH-), 0.70-0.62 (1H, t, -CH_2 -CH(CH)-CH-).

2.3 Synthesis of (4,5-dibromobicyclo [6.1.0] nonan-9-yl) methanol (3)

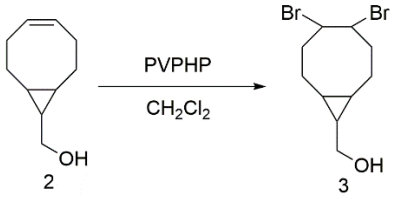

In a 100 mL round bottom flask, a solution of **2** (2.78 g, 18.27 mmol), pyridinium tribromide (PVPHP, 8.59 g, 21.93 mmol) in 50 mL of CH_2Cl_2 stirred for 10 h at room temperature. The reaction mixture washed with 1% citric acid (2×80 mL) and brine (2×80 mL). The organic layer was dried over Na_2SO_4 and the solvent evaporated. The product was purified by flash chromatography (PE: EA = 10:1) and isolated as a white solid (2.4 mg, 42.4%). Structure confirmed by ^{1}H-NMR. ^{1}H-NMR (300 MHz, $CDCl_3$), δ_H (TMS, ppm) : 4.79-4.75 (2H, m, -CHBrCHBr-), 3.46 (2H, d, HO-CH_2-CH-), 2.65-2.50 (2H, m, BrCH-CH_2-CH_2-), 2.05-1.99 (2H, m, BrCH-CH_2-CH_2-), 1.44-1.28 (4H, m, -CH-CH_2-CH_2-), 0.89-0.78 (2H, m, -CH2-CH(CH_2)-CH-, -CH_2-CH(CH_2)-CH-), 0.64-0.60 (1H, m, OHCH_2-CH(CH)-CH-).

2.4 Synthesis of bicyclo [6.1.0] non-4-yn-9-ylmethanol (BCN)

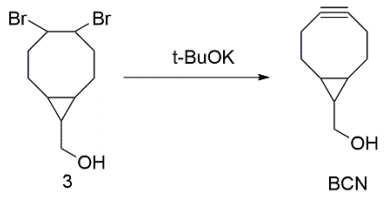

In a 100 mL three necked bottle, a solution of **3** (3 g, 9.60 mmol), potassium tert-butoxide (7.12 g, 63.45 mmol) in 50 mL of dry THF stirred for 4 h at room temperature After the suspension was filtered, concentrated under reduced pressure and purified via silica gel flash chromatography (PE/EA = 30:1) 550 mg of white powder was obtained. Yield: 38.2%. Structure confirmed by ^{1}H-NMR. ^{1}H-NMR (300 MHz, $CDCl_3$), δ_H (TMS, ppm): 3.58 (2H, d, HOCH_2-),

2.35-2.08 (4H, m, ≡C-CH_2-CH_2-), 1.52-1.27 (4H, m, -CH_2-CH_2-CH-), 0.77-0.69 (3H, m, OHCH_2-CH(CH)-CH-).

2.5 Synthesis of bicyclo [6.1.0] non-4-yn-9-ylmethyl (4-nitrophenyl) carbonate (BCN-Phe-NO_2)

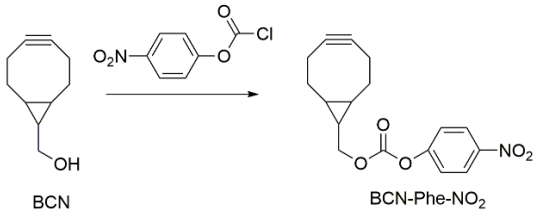

To a solution of BCN (350 g, 2.33 mmol) in CH_2Cl_2 (30 mL), were added 4-Nitrophenyl chloroformate (1.17 g, 5.82 mmol)) and Py (0.64 g, 8.15 mmol) with stirring for 6 h at room temperature. After the CH_2Cl_2 was removed, the product was purified by flash chromatography (PE: EA = 7:1) and isolated as a white powder (520 mg, 71.1%).

2.6 Synthesis of *N*$_2$-(((9H-fluoren-9-yl) methoxy) carbonyl)-*N*$_6$-((bicyclo[6.1.0]- -non-4-yn-9-ylmethoxy) carbonyl) lysine (BCN-Lys-Fmoc-OH)

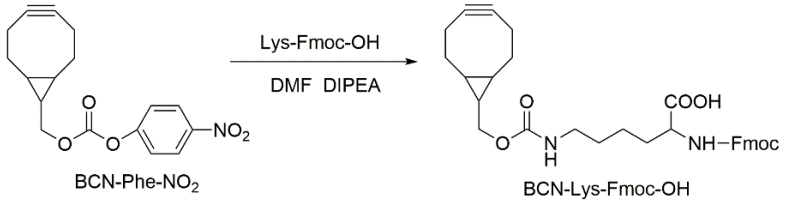

To a solution of BCN-Phe-NO_2 (360 mg, 1.14 mmol) in DMF (5 mL), were added Lys-Fmoc-OH·HCl (612 mg, 1.26 mmol) and DIPEA (0.65 mL, 3.77 mmol) with stirring for 4 h at room temperature. The reaction mixture washed with 1% citric acid (2×80 mL) and brine (2×80 mL). The organic layer was dried over Na_2SO_4 and the solvent evaporated. The product was purified by flash chromatography (CH_2Cl_2: MeOH = 40:1) and isolated as a white solid (320

mg, 51.6%). Structure confirmed by ^{1}H-NMR. ^{1}H-NMR (500 MHz, $CDCl_3$), δ_H (TMS, ppm) : 7.75 (2H, d, J = 7.4 Hz), 7.58 (2H, m), 7.38 (2H, t, J = 7.4 Hz), 7.28 (2H, t, J = 7.4 Hz), 4.39-4.15 (6H, m), 3.17 (2H, m), 2.32-2.12 (2H, m), 1.99-1.85 (2H, m), 1.76-1.68 (2H, m), 1.60-1.52 (4H, m), 1.42 (2H, m), 1.33-1.25 (3H, m), 1.06-0.86 (2H, m).

2.7 Synthesis of 1-(((2-(2-((((9H-fluoren-9-yl)methoxy)carbonyl)amino)-6-(((-bicyclo[6.1.0]non-4-yn-9-ylmethoxy) carbonyl) amino) hexanamido) ethoxy) (hydroxy) phosphoryl) oxy)ethane-1,2-diyl distearate (BCN-Lys-Fmoc-DSPE)

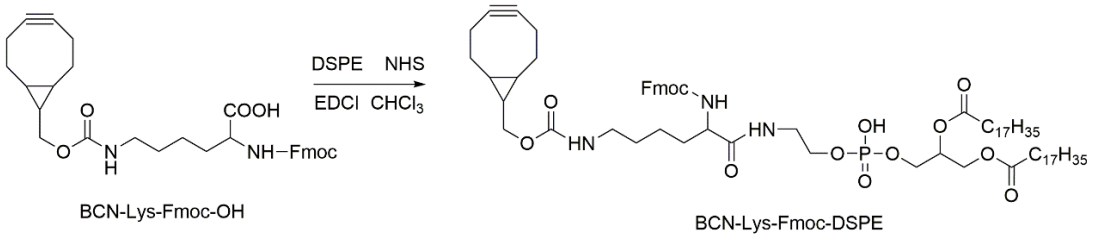

In a 50 mL round bottom flask, a solution of 100 mg (0.18 mmol) of BCN-Lys-Fmoc-OH, 26.00 mg (0.12 mmol) of *N*-hydroxysuccinimide (NHS), 45 mg (0.12 mmol) of 1-(3-Dimethylaminopropyl)-3-ethylcarbodiimide hydrochloride (EDCI) in 20 mL of $CHCl_3$ stirred for 1 h. To a solution of DSPE (137 mg, 0.202 mmol) in $CHCl_3$ (30 mL) was added DIPEA (106 µL, 0.30 mmol) with stiring for 1 h. Then, the mixture of DSPE and DIPEA in $CHCl_3$ was added to the solution of BCN-Lys-Fmoc-OH, NHS and EDCI in $CHCl_3$, then stirred overnight at room temperature. The reaction mixture washed with 1% citric acid (2×80 mL) and brine (2×80 mL). The organic layer was dried over Na_2SO_4 and the solvent evaporated. The product was purified by flash chromatography (CH_2Cl_2: MeOH = 10:1) and isolated as a light pink powder (200 mg, 88.5%). Structure confirmed by ^{1}H-NMR and MS. ^{1}H-NMR (300 MHz, $CDCl_3$), δ_H (TMS, ppm) : 7.72 (2H, d), 7.56 (2H, m), 7.35 (2H, t), 7.26 (2H, t), 5.18 (2H, m),

4.30 (3H, m), 4.15 (2H, m), 3.91 (4H, m), 3.64 (1H, m), 3.09 (2H, m), 2.33-1.99 (12H, m), 1.54-1.39 (10H, m), 1.25-1.23 (52H, m), 0.88 (6H, t), 0.70-0.56 (3H, m). MS: m/z calcd for [$C_{73}H_{11}6N_3O_{13}P$] $(M-H)^-$ 1272.8 found 1272.8, $(M+H_2O-H)^-$ 1290.9 found 1290.9.

2.8 Synthesis of 1-(((2-(2-amino-6-(((bicyclo[6.1.0]non-4-yn-9-ylmethoxy)carbonyl)amino)hexanamido)ethoxy)(hydroxy)phosphoryl)oxy)ethane-1,2-diyldistearate (DSPE-BCN)

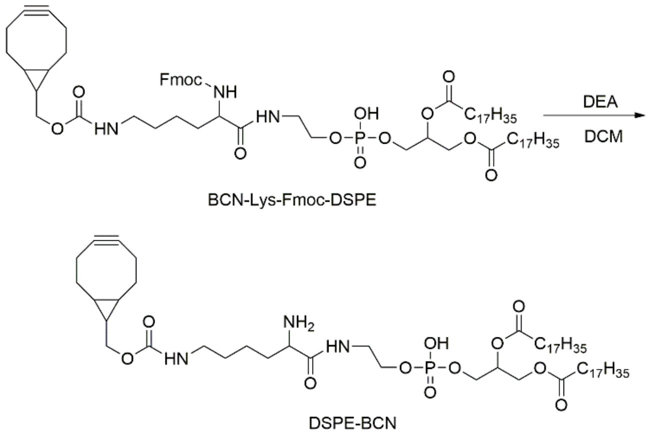

In a 50 mL round bottom flask, a solution of 100 mg of BCN-Lys-Fmoc-DSPE, DEA in 10 mL of CH_2Cl_2 stirred overnight. After the CH_2Cl_2 was removed, the product was purified by flash chromatography (CH_2Cl_2: MeOH = 10:1) and isolated as a white powder (50 mg, 61.3%). Structure confirmed by ^{1}H-NMR and MS. ^{1}H-NMR (300 MHz, $CDCl_3$), δ_H (TMS, ppm) : 5.42 (1H, m), 5.11 (1H, m), 4.40-4.26 (1H, m), 4.09-4.03 (1H, m), 3.90-3.77 (6H, m), 3.67-3.54 (2H, m), 3.07 (2H, m), 2.32-2.09 (8H, m), 1.78 (4H, m), 1.50-1.28 (8H, m), 1.28-1.17 (58H, m), 0.80 (6H, t), 0.61-0.55 (3H, m). MS: m/z calcd for [$C_{58}H_{106}N_3O_{11}P$] $(M-H)^-$ 1050.8 found 1050.8, $(M+H_2O-H)^-$ 1068.8 found 1068.8.

3. Preparation and characterization of liposomes. BCN-Lipo-Ava was prepared by using a

film dispersion method. Briefly, 120 mg natural soybean phosphatidylcholine (SPC), 20 mg DSPE-BCN, 15 mg cholesterol and 3 mg Ava (Selleck) were dissolved in 5 mL of the mixture of $CHCl_3$ and MeOH (3:2, *v:v*). After the organic solvents were removed by the rotary evaporation at 40℃, a thin lipid film was formed and was further dried under vacuum overnight to remove any traces of remaining organic solvents. The lipid film was then hydrated in 5 mL of the distilled water at 37℃ for 30 min. Then the liposomes (BCN-Lipo-Ava) were obtained dispersion using ultrasonic cell disruptor and extrusion through polycarbonate membrane filters with a pore size of 0.22 μm.

For the preparation of BCN-Lipo-RhoB, RhoB-Lipo, BCN-Lipo and RhoB-tagged BCN-Lipo-Ava, SPC (120 mg), DSPE-BCN (20 mg), cholesterol (15 mg) and DHPE-Rhodamine (25 μL, 5 mg/mL) or SPC (120 mg), cholesterol (15 mg) and DHPE-Rhodamine (25 μL, 5 mg/mL) or SPC (120 mg), DSPE-BCN (20 mg), cholesterol (15 mg) or SPC (120 mg), DSPE-BCN (20 mg), cholesterol (15 mg), DHPE-Rhodamine (25 μL, 5 mg/mL) and Ava (3 mg) were dissolved in 5 mL of the mixture of $CHCl_3$ and MeOH (3:2, *v:v*). Then different liposomes were obtained by using the similar method as BCN-Lipo-Ava.

The concentration of Ava in BCN-Lipo-Ava was determined using high performance liquid chromatography (HPLC-LC-2010A HT, SHIMADZU, Japan). The mobile phase was a mixture of acetonitrile and 0.05% aceticacid water (85:15, *v:v*). A Diamonsil ®C18 column (4.6×250 mm, 5 μm) was employed for the separation of analysis at a flow rate of 1 mL/min. The detection wavelength was set at 210 nm and the column temperature was 40°C.

The particle size was measured by a dynamic light scattering (DLS) analyzer (Brookhaven). The encapsulation efficiency (EE) was calculated by the following formula: EE%

= $W/W_0 \times 100\%$, where W and W_0 are the amounts of drugs in the liposomes after and before passing over polycarbonate membrane filters, respectively. The drug-loading capacity (DL) was calculated by the following formula: $DL\% = W_{drug}/W_{lipid} \times 100\%$, where W_{drug} and W_{lipid} are the amounts of drugs and lipids in the resulting liposomes, respectively.

The morphology of BCN-Lipo-Ava was characterized by transmission electron microscopy (TEM). After dripping the aqueous solution of the appropriate amount of the lipid body into the copper mesh, liposomes were stained with 0.5% phosphorus tungstate. After drying, the morphology of liposomes was imaged under transmission electron microscopy (TEM).

The stability of BCN-Lipo-Ava *in vitro* was investigated by detecting the change of particle size in 50% FBS or PBS. Briefly, the BCN-Lipo-Ava was diluted 10 times with 50% FBS or PBS, respectively. After incubation on shaker at 37℃ for different time (0 h, 1 h, 2 h, 4 h, 8 h, 12 h and 24 h), the particle size of BCN-Lipo-Ava was determined on each time point by a dynamic light scattering (DLS) analyzer (Brookhaven).

4. The efficiency analysis of click-reaction. The DSPE-PEG_{5k}-Tre (1 mM) was dissolved in $CHCl_3$ and the UV spectrophotometer is used for wavelength scanning. After adding the DSPE-BCN solution (10 mM in $CHCl_3$), which is fully mixed and reacts at room temperature for 10 minutes, wavelength scanning is performed using ultraviolet spectrophotometer to obtain the absorption curve. For the efficiency analysis of click reaction on surface of BCN-Lipo-Ava, the mole ratios and incubation time of DSPE-PEG_{5k}-Tre and BCN-Lipo-Ava were explored using ultraviolet spectrophotometry. Briefly, DSPE-BCN within BCN-Lipo-Ava and DSPE-PEG_{5k}-

Tre were incubated at different ratios of 0.5:1, 1:1 and 2:1 at room temperature for 0.5 h, 2 h or 12 h, respectively. The characteristic ultraviolet absorbing peak of Tre group at 540 nm was used to determine the efficiency of click reaction between the cell membrane anchoring module and the lipid click module.

5. Proteomics analysis. T-Tre/BCN-Lipo and unconjugated T cells were collected and disrupted using 300 μL 1% SDS lysis buffer supplemented with benzonase and protease inhibitor cocktail, and the cell debris was removed by centrifμgation at 16, 000 g for 30 min. Cellular proteins were quantified using BCA assay. The proteins were diluted to 0.75 μg/μL with total volume reaching 281 μL. The proteins were reduced by 2 mM DTT for 30 min at r.t and alkylated by 20 mM IDDA for 30 min at r.t in dark under rotator stirring. Each sample was divided equally into two tubes and precipitated with 600 μL methanol or 150 μL chloroform and 450 μL ddH_2O. The precipitate was washed twice with 1 mL methanol by centrifugation at 13, 000 g for 15 min. 100 μL 8M Urea was added to each tube to dissolve the proteins, and two tubes of identical samples were combined. For proteomics analysis, the proteins were digested with protease: protein ratio of 1:200 at r.t for 3-4 h. 10% TFA of 1/10 sample volume was added to adjust the pH to ≤ 3. The samples were then desalted by HLB-c18-1cc column, eluted by 1 mL (50% ACN, 0.1% FA) and lyophilized. The lyophilized sample was resuspended with 150 μL pH 8.03 200 mM HEPES solution under vortex and fractionated into twelve fractions by a BP-HRP-HPLC system. Each elution fraction was injected into Orbitrap Fusion™ Lumos™ (Thermo) for mass spectrometry. Gene Ontology (GO) enrichment analysis of expressed proteins was determined using the Cytoscape plugin BiNGO (3.0.4). Proteins related biological

process of TCR signaling (GO: 0050852), T cell activation (GO: 0042110), T cell proliferation (GO: 0042129), and immune effector process (GO: 0002252) were sorted out and shown on the volcano plot.

6. Quantitative real-time PCR. The naïve $CD8^+$ T cells were anchored with BCN-Lipo-Ava or incubated with 1 μM free Ava for 12 h. Then $CD8^+$ T cells, $CD8^+$ T cells plus free ava and T-Tre/BCN-Lipo-Ava cells were stimulated with anti-CD3 and anti-CD28 for different time. Total RNA was isolated from three groups of cells using the TransZol reagent (Transgene, Beijing, China) following the manufacturer's protocol. Total RNA (1 μg) was reverse transcribed to cDNA using a first-strand cDNA Synthesis Kit (TaKaRa). Real-time PCR was performed using the StepOnePlus TM real time PCR system (Applied Biosystems) and AceQ qPCR SYBR Green Master Mix (Vazyme). Quantification was performed according to the manufacturer's instructions, and the expression of target genes was normalized to the housekeeping gene Gapdh or 36B4. The real-time PCR was performed using gene specific primers as previously described.

7. T cell metabolism. The naive $CD8^+$ T cells were anchored with BCN-Lipo-Ava or incubated with 1 μM free Ava for 12 h. Then 1×10^5 cells of each group were seeded in XFe96 FluxPak plate (Seahorse Bioscience, North Billerica, MA) pre-coated with Cell-Tak (Corning). Oxygen consumption rates (OCR) and extracellular acidification rate (ECAR) were measured using XF Cell Mito Stress Test Kit and XF Glycolysis Stress Test Kit (Seahorse Bioscience, North Billerica, MA) on the XF96 Extracellular Flux Analyzer (Seahorse Bioscience, North Billerica,

MA) according to the manufacturer's instructions.

8. Measurement of cell viability with CCK8 assay. B16F10, LN-229 or PC-3 cells (5×10^3) in 100 μL media containing Ava or DMSO were cultured for 24, 48 or 72 h. CCK8 (Keygen Biotech, China) reagent (20 μL) was added into each well. After 2-3 h incubation, the absorbance at 490 nm was measured. The effect of avasimibe on cell viability was obtained by normalizing the absorbance of Ava-treated cells with that of the DMSO-treated cells. The viability value of DMSO-treated cells was set as a control.

9. Modulation of cholesterol levels of plasma membrane by adding or depleting cholesterol. T-Tre/BCN-Lipo-Ava cells, unconjugated T cells or free Ava plus unconjugated T cells were first incubated at 37℃ for 12 h. To reduce the cholesterol level of the plasma membrane, the cells were treated with MβCD (Sigma) for 5 min. To increase the cholesterol level, the cells were treated with MβCD-coated cholesterol (Chol) (Sigma) for 15 min. Then the cells were stimulated with 5 μg/mL plate-bound anti-CD3 and anti-CD28 antibodies for 24 h at 37°C. After that, the cells were collected and stained with APC-Cy7 anti-mouse CD8α (BD PharmingenTM). Next, cells were fixed with 4% PFA and punched through 0.2% Triton-X100. Then the cells were stained with FITC anti-mouse granzyme B (Biolegend), APC anti-mouse IFNγ (Biolegend) or PE anti-mouse TNFα (Biolegend), respectively. The percentage of granzyme B^+, $IFN\gamma^+$ and $TNF\alpha^+$ cells in $CD8^+$ T cells were analyzed and quantified by flow cytometry.

10. Plasma membrane cholesterol level of T-Tre/BCN-Lipo-Ava cell over time. T-Tre/BCN-Lipo-Ava cells, Ava pretreated T cells and unconjugated T cells were incubated at 37°C for 12 h. After incubation, the cells were collected at 0, 2, 4, 8, 12, 24 h and were stained with Filipin III to quantify the level of plasma membrane cholesterol of T cells by flow cytometry.

11. Biodistribution of pmel-1 T-Tre/BCN-Lipo-Ava cell in tumor over time. To prove the targeting and stability of adoptive surface anchor-engineered pmel-1 $CD8^+$ T cell in orthotopic melanoma model, B16F10 cells (1×10^6) were injected intradermally in the flank of C57BL/6J mice on day 0. Mice were lymphodepleted by 2 mg/kg cyclophosphamide and 2 mg/kg fludarabine 6 day after tumor cell inoculation. pmel-1 $CD8^+$ T cells (1×10^7), Ava pretreated pmel-1 T cell (1×10^7), pmel-1 T cell plus unconjugated BCN-Lipo-Ava (1×10^7) or pmel-1 T-Tre/BCN-Lipo-Ava cell (1×10^7) were administered by *i.v.* injection at day 8. After injected for 2, 4, 8, 12, 24, 48 and 72 h, the tumor-infiltrating $CD8^+$ T cells were isolated from tumor and were stained with APC-Cy7-anti-CD8α and PE anti-mouse Thy1.1 by flow cytometry analysis to obtain the percentage of pmel-1 T cells in tumor-infiltrating $CD8^+$ T cells over time. Additionally, Ava pretreated pmel-1 T cell (2 mg/kg for Ava), pmel-1 T cell plus unconjugated BCN-Lipo-Ava (2 mg/kg for Ava) or pmel-1 T-Tre/BCN-Lipo-Ava cell (2 mg/kg for Ava) were administered by *i.v.* injection at day 8. After injection for 2, 4, 8, 12, 24, 48 and 72 h, tumors were collected and homogenized in saline. For analysis of Ava quantity, the homogenate (0.2 mL) was mixed with acetonitrile (0.8 mL), followed by vortex for 5 min and centrifugate at 12000 rpm for 10 min. Then, 200 μL supernatant was transferred to a glass LC vital and quantified by HPLC to determine the concentration of Ava in tumor.

12. Flow cytometry analysis of GD2 expression. Cells were detached from the culture plates (adherent cells were trypsinized and washed two times with PBS) and were incubated with anti-GD2 antibody (14G2a, sc-53831, Santa Cruz Biotechnology) for 1 h and then washed in PBS. After that, the cells were incubated with Alexa Fluor 647-labeled anti-mouse IgG (1:1000) (Thermo) for 30 min, and then twice washed in PBS. All procedures were performed at 4°C. The samples were immediately analyzed using Attune NxT flow cytometer (Thermo). The data was analyzed using FlowJo software.